How to Constrain Your M Dwarf. II. The Mass–Luminosity–Metallicity Relation from 0.075 to 0.70 Solar Masses

Andrew W. Mann[1] , Trent Dupuy[2] , Adam L. Kraus[3] , Eric Gaidos[4] , Megan Ansdell[5,6] , Michael Ireland[7] ,
Aaron C. Rizzuto[3,13] , Chao-Ling Hung[8] , Jason Dittmann[9,13] , Samuel Factor[3] , Gregory Feiden[10] ,
Raquel A. Martinez[3] , Dary Ruíz-Rodríguez[11,12] , and Pa Chia Thao[1]

[1] Department of Physics and Astronomy, University of North Carolina at Chapel Hill, Chapel Hill, NC 27599-3255, USA; awmann@unc.edu
[2] Gemini Observatory, Northern Operations Center, 670 N. Aohoku Place, Hilo, HI 96720, USA
[3] Department of Astronomy, The University of Texas at Austin, Austin, TX 78712, USA
[4] Department of Geology & Geophysics, University of Hawaii at Mānoa, Honolulu, HI 96822, USA
[5] Center for Integrative Planetary Science, Berkeley, CA 94720, USA
[6] Department of Astronomy, University of California at Berkeley, Berkeley, CA 94720, USA
[7] Research School of Astronomy & Astrophysics, Australian National University, Canberra ACT 2611, Australia
[8] Department of Physics, Manhattan College, 4513 Manhattan College Parkway, Riverdale, NY 10471, USA
[9] Massachusetts Institute of Technology, 77 Massachusetts Avenue, Cambridge, MA 02138, USA
[10] Department of Physics, University of North Georgia, Dahlonega, GA 30597, USA
[11] Chester F. Carlson Center for Imaging Science, School of Physics & Astronomy, and Laboratory for Multiwavelength Astrophysics, Rochester Institute of
Technology, 54 Lomb Memorial Drive, Rochester, NY 14623, USA
[12] Research School of Astronomy and Astrophysics, Australian National University, Canberra, ACT 2611, Australia

Abstract

The mass–luminosity relation for late-type stars has long been a critical tool for estimating stellar masses. However, there is growing need for both a higher-precision relation and a better understanding of systematic effects (e.g., metallicity). Here we present an empirical relationship between M_{K_S} and M_* spanning $0.075\,M_\odot < M_* < 0.70\,M_\odot$. The relation is derived from 62 nearby binaries, whose orbits we determine using a combination of Keck/NIRC2 imaging, archival adaptive optics data, and literature astrometry. From their orbital parameters, we determine the total mass of each system, with a precision better than 1% in the best cases. We use these total masses, in combination with resolved K_S magnitudes and system parallaxes, to calibrate the M_{K_S}–M_* relation. The resulting posteriors can be used to determine masses of single stars with a precision of 2%–3%, which we confirm by testing the relation on stars with individual dynamical masses from the literature. The precision is limited by scatter around the best-fit relation beyond measured M_* uncertainties, perhaps driven by intrinsic variation in the M_{K_S}–M_* relation or underestimated uncertainties in the input parallaxes. We find that the effect of [Fe/H] on the M_{K_S}–M_* relation is likely negligible for metallicities in the solar neighborhood ($0.0\% \pm 2.2\%$ change in mass per dex change in [Fe/H]). This weak effect is consistent with predictions from the Dartmouth Stellar Evolution Database, but inconsistent with those from MESA Isochrones and Stellar Tracks (at 5σ). A sample of binaries with a wider range of abundances will be required to discern the importance of metallicity in extreme populations (e.g., in the Galactic halo or thick disk).

Key words: binaries: visual – stars: late-type – stars: low-mass – stars: luminosity function, mass function

Supporting material: machine-readable tables

1. Introduction

Over the past decade, M dwarfs have become critical for a wide range of astrophysics. On small scales, M dwarfs are attractive targets for the identification and characterization of exoplanets. The small size, low mass, and low luminosity of late-type stars facilitate the discovery of small planets (e.g., Muirhead et al. 2012b; Martinez et al. 2017; Mann et al. 2018) in their circumstellar habitable zone (e.g., Tarter et al. 2007; Shields et al. 2016; Dittmann et al. 2017). Close-in, rocky planets are also significantly more common around M dwarfs than their Sun-like counterparts (Dressing & Charbonneau 2013; Petigura et al. 2013; Mulders et al. 2015; Gaidos et al. 2016)

On larger scales, the properties of both the Milky Way and more distant galaxies are inexorably linked to parameters of their most numerous constituents (>70% of stars in the solar neighborhood are M dwarfs; Henry et al. 1994; Reid et al. 2004). Late-type dwarfs weigh heavily on the Galactic mass

function (e.g., Covey et al. 2008) and are useful probes of the Milky Way's structure (e.g., Jurić et al. 2008; Ferguson et al. 2017), kinematics (e.g., Bochanski et al. 2007; Yi et al. 2015), and chemical evolution (Woolf & West 2012; Hejazi et al. 2015). Although K and M dwarfs are much fainter than their higher-mass counterparts, they measurably contribute to the integrated spectra of massive galaxies; thus, M dwarf fundamental properties have become an essential component to studies of the initial mass function (e.g., Conroy & van Dokkum 2012; McConnell et al. 2016) and mass-to-light ratio (Spiniello et al. 2015) of nearby galaxies. Additionally, M dwarf–white dwarf pairs are a plausible progenitor for Type Ia supernovae (Wheeler 2012), and hence late-type stars may be important for cosmology.

For all these areas, it is essential that we have a method to estimate the fundamental parameters of late-type dwarfs. In exoplanet research, this means stellar radii for planet radii in transit surveys, stellar masses for planet masses in radial velocity surveys, and both (stellar densities) for determining

---

[13] 51 Peg b Fellow.

planet occurrence rates (e.g., Winn 2010; Gaidos & Mann 2013), internal structure (e.g., Rogers et al. 2011), and habitability (e.g., Gaidos 2013; Kane et al. 2017). Spectra, photometry, and distances of stars provide a relatively direct means to measure T_{eff} (e.g., Rojas-Ayala et al. 2012; Mann et al. 2013b), luminosity (e.g., Reid et al. 2002), metallicity (e.g., Bonfils et al. 2005; Rojas-Ayala et al. 2010), and radius (e.g., via Stefan–Boltzmann; Newton et al. 2015; Kesseli et al. 2018a). Masses are much more difficult to infer from observations alone, yet they are one of the most important and fundamental properties of a star.

In the case of a binary, it is possible to directly determine the mass of a star from its orbital parameters. For systems with reasonably short orbital periods, the motions of binary components can be monitored to determine their orbits. Radial velocity variation can yield individual stellar masses but only modulo the sine of the orbital inclination (e.g., Torres & Ribas 2002; Kraus et al. 2011; Stevens et al. 2018). In systems where binary components are spatially resolved, monitoring of their position angle and separation can yield a measurement of the total system mass, assuming that the parallax is known (e.g., Söderhjelm 1999; Woitas et al. 2003; Dupuy et al. 2009b). Absolute orbital astrometry (measured with respect to background stars) can yield both individual masses and a direct measurement of the system's parallax (e.g., Köhler et al. 2012; Benedict et al. 2016).

Microlensing can provide mass measurements for single stars (e.g., Zhu et al. 2016; Chung et al. 2017; Shin et al. 2017). Unfortunately, this method cannot be used to target specific M dwarfs of interest, and detected microlensing events are both rare and primarily limited to distant (∼kpc) targets in crowded fields, where follow-up is difficult.

Stellar evolution models can provide mass estimates of targeted single stars (e.g., Muirhead et al. 2012a). However, differences between empirical and model-predicted mass–radius and radius–luminosity relations for late-type stars (e.g., Boyajian et al. 2012; Feiden & Chaboyer 2012) raise concerns about the reliability of model-based masses. Further, the masses derived depend on both the model grid used (Spada et al. 2013; Choi et al. 2016) and the observed parameter over which the interpolation is done (e.g., color vs. luminosity; Mann et al. 2012, 2015). Ultimately, these models need to be tested empirically; differences between the models and empirical determinations can reveal important missing physics or erroneous assumptions in the model assumptions.

An empirical approach to estimating single-star masses is accomplished through a relation between mass and luminosity (e.g., Henry & McCarthy 1993; Delfosse et al. 2000), calibrated with dynamical mass measurements from binary stars. Absolute magnitude can be used as a proxy for luminosity and is generally easy to measure for visual binaries from the same data used to establish the orbit (resolved images/astrometry and a parallax). Deriving such relations for Sun-like stars is difficult, as the scatter is dominated by evolution (e.g., Andersen 1991; Torres et al. 2010), leading to the need for a mass–luminosity–age relation. Because main-sequence late-type stars evolve negligibly over the age of the universe, age becomes a negligible factor and the stellar locus in mass–luminosity space is tight for a fixed metallicity. Adopting near-infrared (NIR) instead of optical magnitudes as a proxy for luminosity mitigates the effect of metallicity, as abundance variations have a weaker effect on the absolute flux levels of M dwarfs past 1.2 μm when compared to optical regions

(Delfosse et al. 2000; Bonfils et al. 2005). Combined with the favorable Strehl ratios in adaptive optics (AO) imaging at K band, this has made the M_K–M_* relation the most precise and commonly used technique for estimated masses of late K and M dwarfs.

Empirical M_K–M_* relations from Henry & McCarthy (1993) and Delfosse et al. (2000) provided mass determinations to ≃10% precision, with more recent improvements by Benedict et al. (2016). However, as fields that rely on M dwarf parameters have pushed to higher precision, there has been an increasing need for proportionate improvements in stellar mass precision. Until recently, the lack of precise distances to M dwarfs was the dominant source of error when estimating masses using the M_{K_S}–M_* relation. With the arrival of *Gaia* parallaxes, many late-type dwarfs beyond the solar neighborhood have <1% parallaxes; the lower precision of existing M_{K_S}–M_* relations is now the dominant source of uncertainty when estimating masses this way. Existing relations also have gaps in their calibration sample, particularly below 0.1 $M_\odot$, where there is need for stellar masses to match new exoplanet surveys (e.g., Gillon et al. 2017). Methods to measure metallicities of M dwarfs have become increasingly precise (e.g., Rojas-Ayala et al. 2010; Neves et al. 2014), making it possible to explore the impact of metallicity on the M_{K_S}–M_* relation. Most importantly, both existing models and empirical measurements of inactive M dwarfs have found tight (<5% intrinsic scatter) mass–radius (e.g., Bayless & Orosz 2006; Spada et al. 2013; Han et al. 2017) and luminosity–radius relations (e.g., Boyajian et al. 2012; Mann et al. 2015; Terrien et al. 2015a), suggesting that similar improvements in the M_{K_S}–M_* relation are achievable.

Here we present a revised empirical relation between M_*, M_{K_S}, and [Fe/H], spanning almost an order of magnitude in mass, from 0.075 to 0.70 $M_\odot$, covering −0.6 < [Fe/H] < +0.4. The relation is built on orbital fits to visual binaries from a combination of AO imaging and astrometric measurements in the literature with metallicities estimated from the stars' NIR spectra. In Section 2 we detail our selection of nearby late-type binaries with orbits amenable to mass determinations. We overview our astrometric and spectroscopic observations in Section 3, including those from telescope archives. We explain our procedure for computing separations and position angles and incorporating similar measurements from the literature in Section 4. Our orbit-fitting procedure is explained in Section 5. We describe our method for determining other parameters of each system ([Fe/H], distance, and M_{K_S}) in Section 6. Our technique to fit the M_{K_S}–M_* relation from these binaries is described in Section 7, including an analysis of the errors as a function of M_{K_S}, tests of our relation on binaries with individual masses, a detailed look at the effects of [Fe/H], and a comparison to earlier similar mass–luminosity relations. We conclude in Section 8 with a brief summary and a discussion of the important caveats and complications to consider when using our relation, as well as future directions we are taking to expand on the current work.

If you want to use the relations in this manuscript, we advise at least reading Section 8.2 to understand the potential limitations of the provided program and posteriors.[14]

2. Sample Selection

Our selection of binaries was designed to sample the region of mass space over which the mass–luminosity relation should not

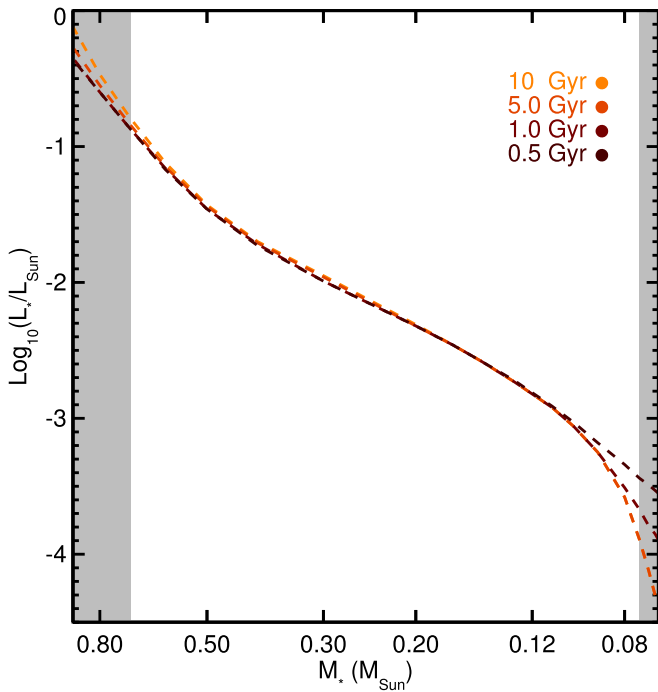---

[14] https://github.com/awmann/M_-M_K-

Figure 1. Stellar luminosity as a function of mass predicted by the Baraffe et al. (2015) models, color-coded by age (metallicity fixed at solar). The gray regions denote masses excluded by this study owing to a significant age dependence on the mass–luminosity relation. We have a lower cut on the low-mass end then implied by the tracks, as some spread at this low-mass end is due to a longer pre-main-sequence lifetime and empirical studies suggest a lower-mass boundary between stars and brown dwarfs.

evolve significantly between the zero-age main sequence and the age of the Galactic disk ($\sim$10 Gyr). We quantified this using the Baraffe et al. (2015) models (Figure 1). Above $0.70\,M_\odot$, a fixed luminosity (the observable) could correspond to a $\simeq$5% range in masses over 1–10 Gyr. Stars below $\simeq0.1\,M_\odot$ take a long time (100–1000 Myr) to arrive on the main sequence but obey a tight relation beyond this point. Those objects below $\simeq0.08\,M_\odot$ are predicted to never reach the main sequence and hence obey no mass–luminosity relation. However, this transition likely depends on metallicity, and empirical studies have found a limit closer to $0.075\,M_\odot$ (e.g., Dieterich et al. 2014; Dupuy & Liu 2017). Therefore, we attempted to select systems spanning $0.075\,M_\odot \lesssim M_* \lesssim 0.70\,M_\odot$.

We first selected systems by cross-matching catalogs of nearby M dwarfs (Lépine et al. 2013; Dittmann et al. 2014; Gaidos et al. 2014; Winters et al. 2015) with the fourth catalog of interferometric measurements of binary stars (INT4; Hartkopf et al. 2001) and AO images from the Keck Observatory Archive (KOA). As part of this cross-match, we also included targets matching the M dwarf selection criteria of Gaidos et al. (2014), but with a bluer color cut ($V - J > 1.8$) to incorporate additional late K dwarfs. We kept any binaries with separations less than 5″. We then added in other known late-type binaries from Law et al. (2008), Janson et al. (2012, 2014), and Ward-Duong et al. (2015). This provided a list of more than 300 multistar systems.

From here we selected binaries amenable to orbital characterization on a reasonable (few year) timescale. To this end, we assumed that the average of available (literature) separation measurements approximates the semimajor axis of the system. Next, we identified systems for which the time

between the first available observation and our final observation would span at least 30% of the orbit (based on our rough semimajor axis estimate), including the 2 yr of our orbital monitoring program with Keck. This cut accounted for existing data. As a result, long-period binaries with extensive previous observations were included, depending on the baseline available, while those with only recent epochs would generally need to have orbits of $\ll$10 yr to be targeted. These cuts left us with 129 systems. We then removed 36 systems at $\delta < -30^\circ$ that were difficult to observe from Maunakea, leaving us with 93 systems to be included in our observing program. Three systems south of this limit (Gl 54, Gl 667, and GJ 1038) were included in our final sample, as they had enough astrometry without our additional monitoring at Keck.

We removed 16 systems from our analysis because of an unresolved tertiary (or quaternary) component noted in the literature (e.g., Tokovinin & Smekhov 2002; Law et al. 2010; Tokovinin 2018). In their current form, such systems were not useful for our analysis, as we had no ΔK magnitudes or mass ratios for the unresolved components. Since many of these are double- or triple-lined systems, it is possible to recover their parameters with multiepoch radial velocities, and some systems have the necessary data in the literature (e.g., Ségransan et al. 2000). We continued to monitor these systems with high-resolution NIR spectrographs (Yuk et al. 2010; Rayner et al. 2012; Park et al. 2014), but they were excluded from the analysis done here. High-order systems where all components are resolved (e.g., GJ 2005ABC) were retained, although we only focus on the tighter pairs in this work.

A total of 17 systems were flagged as young, i.e., affiliated with nearby young moving groups or clusters (Shkolnik et al. 2012, 2017; Gagné et al. 2014, 2015; Kraus et al. 2014; Malo et al. 2014; Riedel et al. 2017; Rizzuto et al. 2017; Lee & Song 2018), or those that are known to be pre-main-sequence (e.g., LP 349-25; Reiners & Basri 2009). We monitored these targets even after flagging them as young, but they were not included in the analysis for the current work. Many of these either are pre-main-sequence stars, and hence will not follow the same mass–luminosity relation, or are atypically active compared to other stars in the solar neighborhood (e.g., Malo et al. 2014). Because these cuts generally only remove extremely young stars, the sample may include some young field stars.

After the completion of our observing program, we removed targets with fewer than six independent astrometric measurements and those lacking a precise parallax ($\sigma_\pi > 7\%$). We attempted to fit orbits of the remaining 57 systems (Section 5). Two of the resulting orbital parameters yielded system/total masses (M_{tot}) for the system too imprecise ($>$20%) to be useful for our analysis. This left us with 55 binaries (110 stars).

Our method uses M_{tot} (as opposed to individual masses) to derive the M_{K_S}–M_* relation (explained in Section 7.1). As a result, constraints on the mass ratio through radial velocities or absolute astrometry are not required to be included in the final sample (just separations and position angles). Since most systems do not have the data required for individual masses, this decision is important to keep the sample size large and the analysis homogeneous.

We added seven targets with orbits from Dupuy & Liu (2017) to fill in the sample around the end of the M dwarf sequence. These seven were selected because they are theoretically massive enough to sustain hydrogen fusion and satisfy all our other selection criteria. Systems from Dupuy & Liu (2017) also had

their orbits fit using a nearly identical method to our own, often using similar or identical sources of data and analysis methods (primarily Keck/NIRC2). Two additional systems in Dupuy & Liu (2017) matched our initial cut but were still omitted from this analysis. These were LP415-20, which Dupuy & Liu (2017) suggest is an anomalous system and possibly an unresolved triple, and 2M1847+55, which has a relatively imprecise orbit compared to the rest of the sample.

Parameters of the final 62 systems included in our analysis are given in Table 1.

3. Observations and Data Reduction

3.1. Near-infrared Spectra with IRTF/SpeX

To estimate the metallicities of our targets, we obtained NIR spectra for 58 of 62 targets using the SpeX spectrograph (Rayner et al. 2003) on the NASA Infrared Telescope Facility (IRTF) atop Maunakea. Observations were taken between 2011 May and 2017 November. Most data were taken as part of programs to characterize the fundamental properties of nearby M dwarfs (e.g., Mann et al. 2013b; Gaidos et al. 2014; Terrien et al. 2015b). All spectra were taken in SXD mode, providing simultaneous wavelength coverage from 0.9 to 2.5 μm. For 56 of the targets, observations were taken using the $0.3 \times 15''$ slit, which yielded a resolution of $R \simeq 2000$. Spectra for two targets (2M2206–20 and 2M2140+16) were taken from Dupuy et al. (2009a) and Dupuy & Liu (2012), which used the $0.5 \times 15''$ and $0.8 \times 15''$ slits (respectively), yielding spectral resolutions of $\simeq$750–1500.

For Gl 65 and HD 239960 the SpeX slit was aligned to get spectra of both targets simultaneously. For all other targets the binary was unresolved or too poorly resolved to separate in the reduction procedure, and instead the slit was aligned with the parallactic angle to compensate for differential refraction. Each target was nodded between two positions along the slit to remove sky background. Depending on the target brightness and conditions, between 6 and 30 individual exposures were taken following this nodding pattern, with exposure times varying from 8 to 180 s. An A0V-type star was observed immediately before or after each target to measure (and remove) telluric lines and flux-calibrate the spectrum. The final stacked spectra had a signal-to-noise ratio (S/N) of >100 per resolving element in the K band for all but the four faintest targets (which had S/N > 50).

Basic data reduction was performed with the `SpeXTool` package (Cushing et al. 2004). This included flat-fielding, sky subtraction, extraction of the 1D spectrum, wavelength calibration, stacking of individual exposures, and merging of individual orders. Telluric lines were removed, and the spectrum was flux-calibrated using the A0V star observations and the `xtellcor` software package (Vacca et al. 2003). When possible, the same A0V star was used for multiple targets taken near each other in time.

Three of the four targets lacking SpeX spectra are too warm (earlier than K5) to derive a metallicity from NIR spectra (Gl 792.1, Gl 765.2, and Gl 667), and the third (Gl 54) is too far south to be observed with IRTF.

3.2. Adaptive Optics Imaging and Masking

We analyzed a mix of AO data from our own program with Keck/NIRC2 and archival imaging from the Keck II Telescope, the Canada–France–Hawaii Telescope (CFHT), the Very Large Telescope (VLT), and the Gemini North Telescope. In general, we analyzed all usable images (e.g., nonsaturated, components resolved) regardless of observing mode and filter.

For our analysis, we considered a single data set a collection of observations with a unique combination of filter, target, and epoch. Each combined data set consisted of a Δm (for a given filter), separation, and position angle.

We separate the observations and reduction by instrument/telescope below. The full list of astrometry and contrast measurements is given in Table 2, sorted by target and date.

3.2.1. Keck II/NIRC2 Imaging and Masking

As part of a long-term monitoring program with Keck II atop Maunakea, between 2015 June and 2018 July we observed 51 of the 55 multistar systems analyzed here. All observations were taken using the facility AO imager NIRC2 in the vertical angle mode (fixed angle relative to elevation axis) and the narrow camera ($\approx$10 mas pixel^{-1}). Depending on the target brightness and observing conditions, images were usually obtained through either the K' ($\lambda_c = 2.124\ \mu$m) or narrow $K_{\rm cont}$ ($\lambda_c = 2.271\ \mu$m) filters, and nonredundant aperture masking (NRM) was always taken using the nine-hole mask and K' filter. After acquiring the target and allowing the AO loops to close, we took 4–10 images or 6–8 interferograms (for NRM), adjusting co-adds and integration time based on the brightness of the target. As most of our targets are bright, observations were usually taken using the Natural Guide Star system (Wizinowich et al. 2000; van Dam et al. 2004), only utilizing the Laser Guide Star mode for the faintest ($R \gtrsim 13$) targets or in poor conditions. In total, our observations provided 155 data sets.

In addition to our own data, we downloaded images from the KOA, spanning 2002 March to 2015 November, all of which were taken with the NIRC2 imager. Archival data comprised a wide range of observing modes, filters, and cameras, although the majority were taken with the narrow camera using either the H- or K-band filters. We included nearly all data with clear detections of both binary components independent of the observing setup. We discarded saturated images, those taken with the coronagraph for either of the component stars, and images where the target is completely unresolved. A total of 36 data sets were used from the archive.

The same data reduction was applied to observations both from our own program and from the archive, following our custom procedure described in Kraus et al. (2016). To briefly summarize, we corrected for pixel value nonlinearity in each frame and then dark- and flat-corrected it using calibrations taken the same night. In cases where no appropriate darks or flats were taken in the same night, we used a set from the nearest available night. We interpolated over "dead" and "hot" pixels, which were identified from superflats and superdarks built from data spanning 2006 to 2016. Because flats are rarely taken in narrowband filters, we used superflats built from the nearest (in wavelength) broadband filter where appropriate (e.g., for $K_{\rm cont}$ we used K' flats). Pixels with flux levels >10σ above the median of the eight adjacent pixels (primarily cosmic rays) were replaced with the median (average of the fourth and fifth ranked). Images were visually inspected as part of identifying the binary location, and a handful (<1%) of images were negatively impacted by our cosmic-ray removal (e.g.,

Table 1
Binary Sample

Name	Comp	R.A. J2000	Decl. J2000	System K_S (mag)	ΔK_S (mag)	M_{tot} ($M_\odot$)	[Fe/H][a] (dex)	Plx (mas)	Plx Ref
Systems analyzed in this paper									
GJ 1005	AB	00:15:28.0	−16:08:01	6.390 ± 0.016	1.145 ± 0.016	0.3188 ± 0.0023	−0.41	166.60 ± 0.30	3
GJ 2005	BC	00:24:44.1	−27:08:24	9.371 ± 0.050[b]	0.320 ± 0.016	0.1567 ± 0.0055	−0.08	128.5 ± 1.5	3
Gl 22	AC	00:32:29.2	+67:14:08	6.037 ± 0.023	2.060 ± 0.035	0.572 ± 0.011	−0.24	99.20 ± 0.60	3
Gl 54	AB	01:10:22.8	−67:26:42	5.132 ± 0.024	0.697 ± 0.036	0.7507 ± 0.0100	+0.17	126.90 ± 0.40	3
GJ 1038	AB	01:25:01.8	−32:51:04	6.207 ± 0.021	0.058 ± 0.016	1.23 ± 0.16	+0.03	39.8 ± 1.6	2
Gl 65	AB	01:39:01.2	−17:57:02	5.343 ± 0.021	0.161 ± 0.019	0.2374 ± 0.0053	+0.04	373.7 ± 2.7	5
Gl 84	AB	02:05:04.8	−17:36:52	5.662 ± 0.020	3.262 ± 0.016	0.523 ± 0.028	−0.14	109.4 ± 1.9	2
2M0213+36	AB	02:13:20.6	+36:48:50	8.518 ± 0.018	1.493 ± 0.018	0.246 ± 0.035	−0.07	74.6 ± 3.5	6
Gl 98	AB	02:27:45.9	+04:25:55	5.113 ± 0.018	0.068 ± 0.015	1.388 ± 0.079	+0.41	58.3 ± 1.1	2
Gl 99	AB	02:28:46.5	+32:15:34	6.062 ± 0.018	0.254 ± 0.016	1.46 ± 0.18	+0.21	38.2 ± 1.6	2
Gl 125	AB	03:09:30.8	+45:43:58	5.840 ± 0.016	1.140 ± 0.016	0.905 ± 0.081	+0.49	63.5 ± 1.9	2
Gl 150.2	AB	03:44:48.5	+46:02:09	5.513 ± 0.017	1.100 ± 0.040	1.553 ± 0.099	−0.14	38.63 ± 0.79	2
Gl 190	AB	05:08:35.0	−18:10:18	5.314 ± 0.018	0.103 ± 0.017	0.835 ± 0.053	+0.25	107.9 ± 2.1	2
GJ 1081	AB	05:33:19.1	+44:48:58	7.335 ± 0.027	0.949 ± 0.018	0.548 ± 0.038	−0.03	65.20 ± 0.40	3
Gl 234	AB	06:29:23.3	−02:48:49	5.421 ± 0.018[c]	1.526 ± 0.016	0.3329 ± 0.0017	+0.11	241.00 ± 0.40	3
LHS 221	AB	06:54:04.2	+60:52:18	6.391 ± 0.025[c]	1.120 ± 0.016	0.5306 ± 0.0079	−0.21	95.60 ± 0.30	3
LHS 224	AB	07:03:55.7	+52:42:06	7.776 ± 0.021	0.155 ± 0.017	0.2480 ± 0.0094	−0.60	112.6 ± 1.4	3
Gl 263	AB	07:04:17.7	−10:30:31	6.427 ± 0.017	0.441 ± 0.020	0.93 ± 0.17	+0.43	62.4 ± 3.6	2
Gl 277	AC	07:31:57.7	+36:13:09	5.927 ± 0.017	1.931 ± 0.016	0.738 ± 0.020	+0.18	83.327 ± 0.069	12
2M0736+07	AB	07:36:25.1	+07:04:43	7.282 ± 0.020	0.272 ± 0.016	0.280 ± 0.015	+0.03	117.1 ± 2.1	1
Gl 301	AB	08:13:08.5	−13:55:01	5.815 ± 0.026	0.506 ± 0.018	1.17 ± 0.15	−0.18	53.0 ± 2.2	8
Gl 310	AB	08:36:25.5	+67:17:42	5.580 ± 0.015	2.134 ± 0.017	0.801 ± 0.054	−0.06	72.6 ± 1.3	2
Gl 330	AB	08:57:04.6	+11:38:49	6.486 ± 0.023	1.086 ± 0.016	0.92 ± 0.14	−0.17	58.8 ± 2.7	2
LHS 6167	AB	09:15:36.4	−10:35:47	7.733 ± 0.017	0.143 ± 0.016	0.2801 ± 0.0087	−0.13	103.3 ± 1.0	9
Gl 340	AB	09:17:53.4	+28:33:38	4.767 ± 0.017	0.024 ± 0.020	1.365 ± 0.054	−0.39	57.92 ± 0.76	2
Gl 352	AB	09:31:19.4	−13:29:19	5.511 ± 0.020	0.119 ± 0.018	0.766 ± 0.083	−0.03	99.9 ± 3.6	2
Gl 381	AB	10:12:04.6	−02:41:04	6.193 ± 0.026	0.811 ± 0.016	0.824 ± 0.092	−0.12	81.1 ± 2.9	2
Gl 416	AB	11:11:33.1	−14:59:28	5.874 ± 0.017	0.980 ± 0.017	1.19 ± 0.10	−0.20	46.4 ± 1.3	2
Gl 469	AB	12:28:57.6	+08:25:31	6.956 ± 0.026	1.100 ± 0.016	0.514 ± 0.011	+0.19	76.40 ± 0.50	3
Gl 473	AB	12:33:17.4	+09:01:15	6.042 ± 0.020	0.001 ± 0.018	0.262 ± 0.016	+0.09	227.9 ± 4.6	5
Gl 494	AB	13:00:46.6	+12:22:32	5.578 ± 0.016	4.269 ± 0.017	0.666 ± 0.035	+0.30	85.5 ± 1.5	2
Gl 570	BC	14:57:26.5	−21:24:40	3.980 ± 0.038[c]	1.067 ± 0.036	0.854 ± 0.039	+0.18	170.011 ± 0.085	12
Gl 600	AB	15:52:08.1	+10:52:28	5.819 ± 0.023	0.029 ± 0.018	1.228 ± 0.032	+0.01	47.65 ± 0.30	11
Gl 623	AB	16:24:09.2	+48:21:10	5.915 ± 0.023	2.501 ± 0.040	0.4944 ± 0.0044	−0.44	125.00 ± 0.30	3
GJ 1210	AB	17:07:40.8	+07:22:06	8.419 ± 0.025	0.075 ± 0.017	0.259 ± 0.022	−0.19	82.0 ± 2.3	1
Gl 660	AB	17:11:52.2	−01:51:06	6.656 ± 0.021	0.033 ± 0.017	0.623 ± 0.062	−0.20	84.6 ± 2.8	5
Gl 661	AB	17:12:07.8	+45:39:58	4.834 ± 0.023	0.251 ± 0.020	0.595 ± 0.053	−0.41	167.3 ± 5.0	2
Gl 667	AB	17:18:57.1	−34:59:23	3.191 ± 0.040[c]	0.310 ± 0.035	1.304 ± 0.012	−0.49	138.017 ± 0.092	12
HIP 86707	AB	17:43:00.7	+05:47:21	6.631 ± 0.018	0.926 ± 0.017	0.93 ± 0.14	−0.09	50.1 ± 2.5	2
Gl 695	BC	17:46:25.1	+27:43:00	4.953 ± 0.016	0.287 ± 0.016	0.8374 ± 0.0089	+0.22	120.33 ± 0.16	2
Gl 747	AB	19:07:42.9	+32:32:41	6.416 ± 0.020	0.098 ± 0.016	0.415 ± 0.026	−0.20	122.3 ± 2.5	5
Gl 748	AB	19:12:14.5	+02:53:11	6.342 ± 0.018[c]	1.035 ± 0.024	0.5369 ± 0.0071	−0.23	98.40 ± 0.30	3
Gl 762.1	AB	19:31:08.5	+58:35:13	4.463 ± 0.015	0.155 ± 0.020	1.446 ± 0.053	−0.17	58.37 ± 0.54	11
Gl 765.2	AB	19:39:05.9	+76:25:18	5.898 ± 0.016	0.371 ± 0.037	1.346 ± 0.068	−0.35	33.67 ± 0.53	2
GJ 1245	AC	19:53:54.4	+44:24:53	6.854 ± 0.016	1.124 ± 0.016	0.20304 ± 0.00039	+0.01	214.528 ± 0.082	12
Gl 791.2	AB	20:29:48.3	+09:41:20	7.307 ± 0.024	1.565 ± 0.018	0.289 ± 0.012	+0.05	113.40 ± 0.20	3
Gl 804	AB	20:44:21.9	+19:44:59	6.553 ± 0.016	1.083 ± 0.016	0.97 ± 0.13	−0.09	47.4 ± 2.1	2
Gl 831	AB	21:31:18.5	−09:47:26	6.379 ± 0.020	1.221 ± 0.016	0.4189 ± 0.0033	+0.20	125.30 ± 0.30	3
Gl 844	AB	22:01:49.0	+16:28:02	6.180 ± 0.021	0.108 ± 0.016	0.879 ± 0.096	+0.21	61.8 ± 2.2	2
HD 239960	AB	22:27:59.5	+57:41:45	4.777 ± 0.029	0.994 ± 0.017	0.461 ± 0.011	−0.11	249.9 ± 1.9	2
HIP 111685	AB	22:37:29.9	+39:22:51	5.872 ± 0.027	0.913 ± 0.016	1.196 ± 0.020	+0.03	47.61 ± 0.20	12
Gl 893.4	AB	23:16:39.7	+19:37:17	7.303 ± 0.017	0.052 ± 0.016	0.85 ± 0.12	−0.17	32.5 ± 1.5	1
Gl 900	BC	23:35:00.2	+01:36:19	7.571 ± 0.050[b]	0.758 ± 0.018	0.606 ± 0.018	+0.03	48.17 ± 0.31	11
LHS 4009	AB	23:45:31.2	−16:10:19	8.312 ± 0.016	0.068 ± 0.017	0.283 ± 0.015	−0.16	80.0 ± 1.4	10
Gl 913	AB	23:58:43.4	+46:43:44	5.831 ± 0.020	1.327 ± 0.018	0.93 ± 0.12	−0.12	67.0 ± 3.0	7
Systems from Dupuy & Liu (2017)									
LHS 1901	AB	07:11:11.4	+43:29:58	9.126 ± 0.018	0.094 ± 0.010	0.2029 ± 0.0090	−0.41	76.4 ± 1.1	4
2M0746+20	AB	07:46:42.5	+20:00:32	10.468 ± 0.022	0.357 ± 0.025	0.1535 ± 0.0017	−0.18[d]	81.24 ± 0.25	4
2M1017+13	AB	10:17:07.5	+13:08:39	12.710 ± 0.023	0.113 ± 0.024	0.149 ± 0.016	−0.35[d]	32.2 ± 1.2	4
2M1047+40	AB	10:47:13.8	+40:26:49	11.254 ± 0.018	0.289 ± 0.049	0.171 ± 0.012	+0.17	39.02 ± 0.90	4

Table 1
(Continued)

Name	Comp	R.A. J2000	Decl. J2000	System K_S (mag)	ΔK_S (mag)	M_{tot} ($M_\odot$)	[Fe/H][a] (dex)	Plx (mas)	Plx Ref
LSJ1735+26	AB	17:35:12.9	+26:34:47	10.157 ± 0.020	0.490 ± 0.020	0.1779 ± 0.0078	$+0.03$	64.82 ± 0.95	4
2M2140+16	AB	21:40:29.3	+16:25:18	11.826 ± 0.031	0.743 ± 0.075	0.190 ± 0.017	-0.10[e]	29.52 ± 0.88	4
2M2206−20	AB	22:06:22.8	−20:47:05	11.315 ± 0.027	0.067 ± 0.016	0.168 ± 0.016	-0.05[e]	36.6 ± 1.2	4

Notes. Parallax references: (1) this work (MEarth); (2) van Leeuwen 2007; (3) Benedict et al. 2016; (4) Dupuy & Liu 2017; (5) van Altena et al. 1995; (6) Finch & Zacharias 2016; (7) Goldin & Makarov 2006; (8) Söderhjelm 1999; (9) Bartlett et al. 2017; (10) Riedel et al. 2010; (11) Gaia Collaboration et al. 2016; (12) companion to star in Lindegren et al. (2018).
[a] Errors on [Fe/H] are limited primarily by the calibration (Mann et al. 2013a, 2014) and are 0.08 dex for all targets unless otherwise noted.
[b] K_S magnitude from 2MASS contains a third star; listed K_S magnitude has third star's flux removed.
[c] Synthetic K_S magnitudes derived from spectra. All other K_S magnitudes are from 2MASS.
[d] L dwarfs are beyond the calibration range of Mann et al. (2014); [Fe/H] values should be used with caution.
[e] Abundance derived from lower-resolution IRTF spectrum; σ[Fe/H] estimated to be 0.12 dex.

(This table is available in its entirety in machine-readable form.)

removal of part of the source). For these, we used the data prior to cosmic-ray rejections.

3.2.2. CFHT/KIR Imaging

We obtained data for 34 of our targets from the Canadian Astronomy Data Centre archive, all taken with the 3.6 m CFHT using the Adaptive Optics Bonnette (AOB, often referred to as PUEO after the Hawaiian owl; Arsenault et al. 1994) and the KIR infrared camera (Doyon et al. 1998). After removing images where the target was saturated, unresolved, or had poor AO correction, a total of 239 data sets were included. Observations spanned 1997 December to 2007 January, covering most of the time PUEO was in use at CFHT (1996–2011). Images were taken using a range of filters across JHK bands, but the majority used either the narrowband Brγ or [Fe II] filters. All data were taken using a three- to five-point dither pattern and included at least two images at each dither location.

Data reduction for KIR observations followed the same basic steps as our NIRC2 data. We first applied flat-fielding and dark correction using a set of superflats and superdarks built by splitting the data sets into 6-month blocks and combining calibration data within the same time period. As with the NIRC2 data, we identified bad pixels by comparing each image to a set of superflats built from calibration data spanning all downloaded data. To identify cosmic rays, we first stacked consecutive images of each target (at a fixed location, so not including dithers), recording the robust mean and standard deviation at each pixel. Pixels $>10\sigma$ above this robust mean were replaced with the median of the eight surrounding points. Since KIR data were taken in sets of >5 images before the object was dithered, this median filtering was effective for removing nearly all cosmic rays.

3.2.3. VLT/NaCo Imaging

We downloaded AO-corrected images from the ESO archive taken with the Nasmyth Adaptive Optics System Near-Infrared Imager and Spectrograph (NAOS-CONICA, or NaCo) instrument on VLT. Data spanned 2002 November to 2016 October, with about half of the 72 data sets taken from 2001 to 2005. Based on the program abstracts, $\lesssim 1/2$ of the observations were meant to use these binaries as astrometric or photometric calibration (e.g., science case is unrelated to M dwarfs or

binaries). Data covered 21 of our targets, excluding saturated or otherwise unusable data. Observations were taken with a wide range of filters, cameras, and observing patterns, but the majority were taken using the S13 camera (≈ 13 mas pixel^{-1}), with either broadband K_s and L or narrowband [Fe II] and Brγ filters, and always followed a two- to four-point dither pattern.

Basic data reduction was applied to NaCo images following a similar procedure with the KIR and NIRC2 data. We applied flat-fielding and dark corrections to each observation using the standard set of calibrations taken each night as part of the VLT queue. In the case where calibration (dark or flat) images were missing or unusable, we used the nearest (in time) set of calibration images matching the filter (for flats) and exposure setup (for darks). Flats taken in broadband filters were used for flat-fielding narrowband images at similar wavelengths. We built bad pixel masks using median stacks of all images taken within a night after applying flat and dark corrections. To identify and remove cosmic rays, we used the L.A. Cosmic software (van Dokkum 2001).

3.2.4. Gemini/NIRI Imaging

We retrieved 36 data sets for eight of our targets from the Gemini archive, all taken with the AO imager NIRI (Hodapp et al. 2003) on the Frederick C. Gillett Gemini Telescope (Gemini North). All observations were taken between 2004 August and 2011 February with the assistance of the ALTtitude conjugate Adaptive optics for the InfraRed (ALTAIR). Most observations were taken with the f32 camera (≈ 21 mas pixel^{-1}) using broadband J-, H-, or K-band filters. All observations followed a two- to four-point dither pattern and took at least two images at each dither location.

Data from NIRI were reduced using the same basic methods as for all other AO data. First, we applied flat and dark corrections to each set of images using the standard calibration images taken as part of the Gemini queue, usually within 24 hr of the target observations. In most cases, flats taken in broadband filters were used for narrowband flat-fielding. We then identified bad pixels from median filtering of all images within a given night. Observations with a target near or on top of a heavily impacted pixel (identified with the mask) were discarded. We used the L.A. Cosmic software for the identification and removal of cosmic rays.

Table 2
Input Astrometry and Photometry

UT Date[a] (YYYY-MM-DD)	ρ (mas)	θ (deg)	Filter	Δm[b] (mag)	Source[c]	PI[d]
			GJ 1005			
		R.A., Decl. = 00:15:28.0, −16:08:01				
1993 Aug 9	397.7 ± 4.6	236.10 ± 0.85	⋯	⋯	Benedict et al. (2016)	
1994 May 22	286.6 ± 4.6	200.20 ± 0.85	⋯	⋯	Benedict et al. (2016)	
1994 Aug 15	242.1 ± 4.6	181.70 ± 0.85	⋯	⋯	Benedict et al. (2016)	
1994 Oct 15	213.8 ± 4.6	161.70 ± 0.85	⋯	⋯	Benedict et al. (2016)	
1994 Dec 1	194.1 ± 4.6	146.60 ± 0.85	⋯	⋯	Benedict et al. (2016)	
1995 Jun 25	193.6 ± 4.6	56.80 ± 0.85	⋯	⋯	Benedict et al. (2016)	
1995 Aug 1	198.3 ± 4.6	41.70 ± 0.85	⋯	⋯	Benedict et al. (2016)	
1995 Sep 11	205.3 ± 4.6	26.30 ± 0.85	⋯	⋯	Benedict et al. (2016)	
1995 Oct 30	209.2 ± 4.6	8.20 ± 0.85	⋯	⋯	Benedict et al. (2016)	
1995 Dec 11	218.2 ± 4.6	353.90 ± 0.85	⋯	⋯	Benedict et al. (2016)	
1996 Jun 2	281.0 ± 4.6	308.80 ± 0.85	⋯	⋯	Benedict et al. (2016)	
1996 Jun 24	290.5 ± 4.6	305.30 ± 0.85	⋯	⋯	Benedict et al. (2016)	
1996 Jul 28	305.7 ± 4.6	298.70 ± 0.85	⋯	⋯	Benedict et al. (2016)	
1996 Dec 25	364.0 ± 4.6	278.80 ± 0.85	⋯	⋯	Benedict et al. (2016)	
1997 Jun 29	406.2 ± 4.6	258.50 ± 0.85	⋯	⋯	Benedict et al. (2016)	
1997 Nov 10	410.6 ± 4.6	247.40 ± 0.85	⋯	⋯	Benedict et al. (2016)	
1997 Dec 18	410.1 ± 4.6	243.20 ± 0.85	⋯	⋯	Benedict et al. (2016)	
2000 Aug 20	227.0 ± 5.6	340.9 ± 2.5	BrG	1.067 ± 0.013	CFHT/KIR	Perrier-Bellet
2000 Dec 12	274.4 ± 2.0	312.0 ± 2.6	H	1.110 ± 0.067	CFHT/KIR	Roddier
2000 Dec 12	270.3 ± 4.0	312.4 ± 2.6	K	1.070 ± 0.025	CFHT/KIR	Roddier
2001 Aug 4	376.4 ± 1.9	276.8 ± 2.5	BrG	1.142 ± 0.039	CFHT/KIR	Perrier-Bellet
2001 Aug 31	383.7 ± 2.0	273.8 ± 2.5	Fe II	1.190 ± 0.017	CFHT/KIR	Forveille
2002 Jun 25	420.0 ± 3.0	240.7 ± 2.5	Fe II	1.175 ± 0.041	CFHT/KIR	Beuzit
2002 Sep 11	410.2 ± 1.6	238.8 ± 2.5	PaBe	1.220 ± 0.040	CFHT/KIR	Beuzit
2002 Nov 21	392.8 ± 1.6	227.0 ± 2.5	H2v = 2–1	1.114 ± 0.049	CFHT/KIR	Forveille
2003 Oct 16	227.3 ± 4.6	174.1 ± 2.7	H2v = 2–1	1.196 ± 0.095	CFHT/KIR	Forveille
2003 Dec 10	210.8 ± 2.1	157.82 ± 0.43	Fe II	1.255 ± 0.044	VLT/NaCo	Beuzit
2004 Jan 8	199.4 ± 2.9	146.2 ± 2.7	BrG	1.115 ± 0.057	CFHT/KIR	Coustenis
2004 Jul 2	200.5 ± 2.1	66.3 ± 2.6	H2v = 2–1	1.310 ± 0.042	CFHT/KIR	Forveille
2004 Sep 24	206.6 ± 2.1	36.66 ± 0.53	Fe II	1.239 ± 0.011	VLT/NaCo	Beuzit
2005 Oct 16	327.4 ± 5.1	289.1 ± 2.5	H2v = 2–1	1.108 ± 0.035	CFHT/KIR	CFHTTeam
2007 Aug 9	374.0 ± 9.9	221.4 ± 1.8	⋯	⋯	Mason et al. (2018)	
2007 Aug 29	369.5 ± 2.0	220.84 ± 0.43	Fe II	1.211 ± 0.023	VLT/NaCo	Montagnier
2014 Jul 30	270.6 ± 1.0	314.05 ± 0.10	K_{cont}	1.196 ± 0.012	Keck/NIRC2	Dupuy
2015 Jun 23	399.2 ± 1.0	266.75 ± 0.10	K_{cont}	1.203 ± 0.011	Keck/NIRC2	Ireland
2015 Nov 27	422.6 ± 1.0	252.06 ± 0.10	K_{cont}	1.209 ± 0.011	Keck/NIRC2	Ireland
2015 Nov 30	426.8 ± 3.8	251.70 ± 0.96	⋯	⋯	Tokovinin et al. (2016)	
2016 Sep 20	376.5 ± 1.2	223.60 ± 0.10	K_{cont}	1.211 ± 0.017	Keck/NIRC2	Mann

Notes.
[a] Dates from literature points may be off by 1 day owing to inconsistency in reporting UT versus local date.
[b] Errors on Δm values are based on the scatter in individual images and are likely underestimated.
[c] Astrometries with source as Keck/NIRC2, CFHT/KIR, VLT/NaCo, or Gemini/NIRI are from this paper. All other measurements list the paper reference.
[d] Principal investigator for AO data analyzed in this paper (from our program or the archive) as it was listed in the image header.

(This table is available in its entirety in machine-readable form.)

4. Astrometry and Photometry

Extracting separations and position angle measurements followed a similar multistep procedure across all instruments, excluding the NRM data (which is described below). Our method is based largely on that described in Dupuy et al. (2016) and Dupuy & Liu (2017), which is built on the techniques from Liu et al. (2008) and Dupuy et al. (2010).

We first cross-correlated each image with a model Gaussian point-spread function (PSF) to identify the most significant peaks. The cross-correlation peak occasionally centers on instrumental artifacts, often struggling to separate partially overlapping binaries, and can easily identify the wrong source for triple systems. This step was checked by eye and updated as needed. The eye-check phase also allowed us to manually remove data of poor quality, e.g., no or poor AO correction, saturated data, or unresolved systems. We used these centers as the initial guess for the pixel position utilized in the next phase.

We then fit the PSF centers by either (1) running StarFinder, a routine designed to measure astrometry and photometry from AO data by deriving a PSF template from the image and iteratively fitting this model to the components (for more details, see Diolaiti et al. 2000), or (2) fitting the binary

image with a PSF modeled by three-component elliptical 2D Gaussians using the least-squares minimization routine MPFIT (Markwardt 2009). Although the results of these two methods generally agreed, StarFinder was preferred, as it used a nonparametric and more realistic model of the PSF and worked with mediocre AO correction, provided that the component PSFs were well separated. StarFinder, however, failed on the tightest binaries, where it was unable to distinguish two stars and, as a result, incorrectly built an extended PSF that fit the blended image. The Gaussian fit was used for these cases where StarFinder failed.

As part of the PSF fit, both methods provided a flux ratio of the PSF normalization factors, which we used to determine the contrast Δm in the relevant band. Data from all filters are used for astrometry, although only measurements in the K band (K_s, K, K', Brγ, and K_{cont}) were used in the estimate of M_{K_s} (see Section 6.3).

PSF fitting provides pixel position measurements of each component, but converting these to separation (ρ) and position angle (PA) on the sky requires an astrometric calibration of the instrument. For the NIRC2 narrow camera, we used the Yelda et al. (2010) distortion solution for data taken before 2015 April 13 UT and the Service et al. (2016) solution for data taken after this. These calibrations include a pixel scale and orientation determination of 9.952 ± 0.002 mas pixel^{-1} and $0°252 \pm 0°009$ for the former and 9.971 ± 0.004 mas pixel^{-1} and $0°262 \pm 0°020$ for the latter. For the NIRC2 wide camera we used the solution from H. Fu et al. (2012, private communication),[15] with a pixel scale of 39.686 ± 0.008 mas pixel^{-1} and the same orientation as the narrow camera. For the $f/32$ camera on NIRI, we used the distortion solution from the Gemini webpage.[16]

For other instruments and cameras, data were always taken following a dither pattern to sample different regions of the CCD distortion pattern. Hence, the rms between dithered images should reflect errors due to uncorrected distortion (which is included in our errors; see below). For KIR (CFHT/ PUEO), we adopted a pixel scale of 34.8 ± 0.1 mas pixel^{-1} (Stapelfeldt et al. 2003) and an orientation of $0° \pm 2°$.[17] For NaCo, we assumed a pixel scale of 13.24 ± 0.05 mas pixel^{-1} for the S13 camera (Masciadri et al. 2003; Neuhäuser et al. 2005) and the values given in the ESO documentation for all others[18] (with the same error). The rotation taken from the NaCo headers was assumed to be correct to $0°4$ (Seifahrt et al. 2008). For NIRI observations, we used a pixel scale provided in the Gemini documentation[19] for each camera (117.1, 49.9, and 21.9 mas pixel^{-1} for $f/6$, $f/14$, and $f/32$, respectively), with a global uncertainty of 0.05 mas pixel^{-1} on the pixel scale and $0°1$ on the orientation (Beck et al. 2004).

Calculation of separations and position angles from NRM observations followed the procedures in the Appendix of Kraus et al. (2008) with the aid of the latest version of the "Sydney" aperture-masking interferometry code.[20] To remove systematics, each NRM observation of a science star was paired with that of a single calibrator star taken in the same night with a similar magnitude and air mass. Binary system profiles were

then fit to the closure phases to produce estimates of the separation, position angle, and contrast of the binary components. More details on the analysis of masking data can be found in Lloyd et al. (2006), Kraus et al. (2008), and Evans et al. (2012).

All data in a single set (same target, filter, and night) were combined into a single measurement (after applying all corrections above), with errors estimated using the rms in the individual images within a night. This scatter across images was combined with the uncertainty in the orientation and pixel scale in quadrature. We assumed that the pixel scale and orientation uncertainties were completely correlated within a night and filter, so they do not decrease with repeat observations.

We also corrected separation and position angle measurements for differential atmospheric refraction (DAR; Lu et al. 2010) using filter wavelength information and weather data from the header (for VLT) or from the CFHT weather archive[21] (for Keck, CFHT, and Gemini). We disregarded the chromatic component of this effect, as the correction is small compared to measurement errors.

4.1. Literature Astrometry

To help identify literature astrometry for our targets, we used the fourth catalog of interferometric observations of binary stars (INT4; Hartkopf et al. 2001). We only used measurements with both a separation and position angle. In cases where the literature data were also available in one of the archives above (i.e., the same data set used in the reference), we adopted our own measurements over the literature data. We did not utilize contrast measurements from the literature.

In total, we used 597 measurements (each including a separation and position angle) covering 51 of the 55 systems analyzed here. Although we pulled astrometry from 71 different publications, most of the measurements come from $\sim$10 different surveys (which may be spread across numerous publications). For example, 160 points came from *HST*, primarily the Fine Guidance Sensors measurements of 14 systems (e.g., Benedict et al. 2016), and 180 measurements came from speckle observations on the Special Astrophysical Observatory 6 m (e.g., Balega et al. 2002a), WIYN (e.g., Horch et al. 2017), or SOAR (e.g., Tokovinin 2017) telescopes. The rest of the measurements are from a mix of surveys focusing on taking many epochs of specific systems to determine orbits (e.g., Köhler et al. 2012), broader surveys (e.g., for multiplicity) that obtain one to two epochs on dozens of binaries (e.g., Janson et al. 2012), and programs targeting M dwarfs (e.g., Mason et al. 2018).

For a single system, GJ 1005, the position angle measurements from Benedict et al. (2016) differed significantly from our own astrometry and other literature determinations. The offset is consistent with a sign error in the individual positions assigned to each target before computing the final position angle. An earlier analysis of this same data set by Hershey & Taff (1998) gave position angles consistent with ours and discrepant from Benedict et al. (2016). We opt to use the Benedict et al. (2016) values over Hershey & Taff (1998) because the former is more precise, but we apply the relevant correction to the Benedict et al. (2016) position angles to correct the sign error. The separations were not affected, and no other system showed a similar discrepancy.

---

[15] http://homepage.physics.uiowa.edu/~haifu/idl/nirc2wide/
[16] http://www.gemini.edu/sciops/instruments/niri/undistort.pro
[17] http://www.cfht.hawaii.edu/Instruments/Detectors/IR/KIR/
[18] http://www.eso.org/sci/facilities/paranal/instruments/naco/doc.html
[19] http://www.gemini.edu/sciops/instruments/niri/imaging/pixel-scales-fov-and-field-orientation
[20] https://github.com/mikeireland/idlnrm
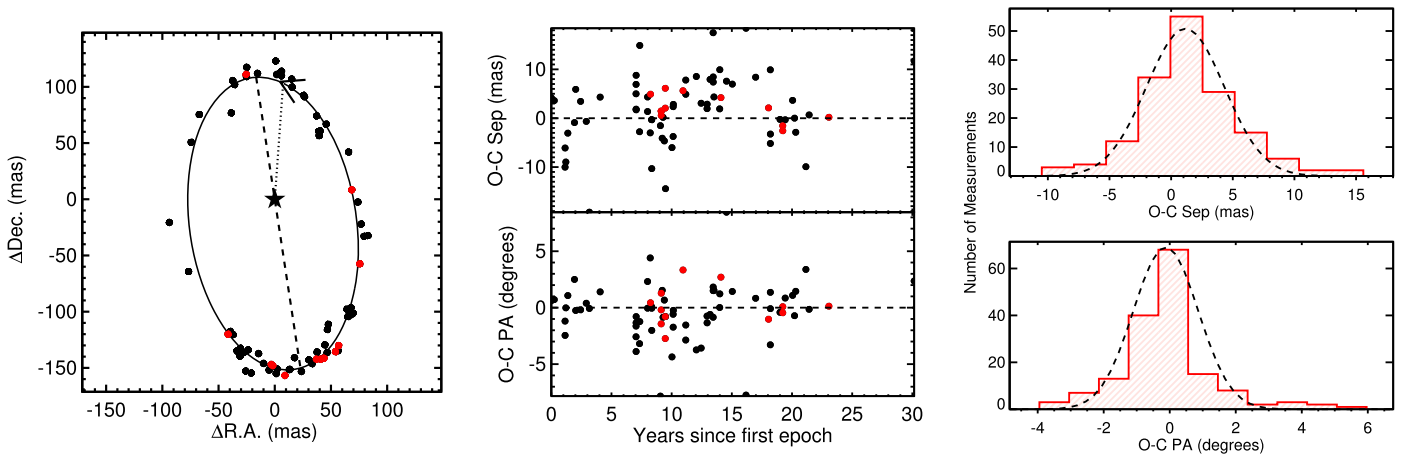[21] http://mkwc.ifa.hawaii.edu/archive/wx/cfht/

Figure 2. Example of our method for assessing any missing error terms in literature astrometry. The left and middle panels show the orbit (left) and residuals (middle) for an example binary, HR 1331AB. Literature points are shown as circles in the left and middle panels. In the left panel, the solid line is the best fit, the dotted line connects periastron passage, with an arrow pointing in the orbital direction, and the dashed line indicates the line of nodes. Measurements taken using the speckle imager on the BTA 6 m are labeled in red. The rightmost panels show a histogram of separation and position angle residuals from measurements taken with the BTA 6 m across 39 different binaries. The total residuals are modeled well by a Gaussian function, which we used to estimate the missing error term after subtracting out reported measurement uncertainties and errors in the orbital parameters.

One complication using older literature astrometry is inhomogeneous reporting of separation and position angle errors. Many references provided separations and position angles without uncertainties or have a discussion of general uncertainties but do not provide them for individual measurements. A separate problem is references that reported measurement errors only, usually derived from a set of observations of a given target within a night or observing run (e.g., errors due to scatter in the PSF fit or variations in separation and position angle between exposures). Because we combined measurements from multiple instruments and sources, it is critical that we also account for systematic effects, i.e., those that impact all the images in a given set of observations (and hence are likely not reflected in the reported measurement uncertainties). This includes field distortion, the adopted pixel scale and instrument orientation, and DAR. These effects cannot be removed or modeled from individual epochs and can be larger than measurement uncertainties alone, particularly for extremely high precision measurements (e.g., Lu et al. 2009).

The most robust corrections for systematic were accomplished by observing crowded fields at multiple pointings and orientations. The extracted position of each star can then be compared to an external catalog and/or to repeat measurements with the star on different regions of the detector. Similar methods were used to calibrate a wide range of high-precision AO systems, including those used in this work (Yelda et al. 2010; Plewa et al. 2015; Service et al. 2016). In the absence of such data, observations of binaries with relatively well-determined orbits were often used as a low-order correction to the orientation or pixel scale (e.g., Tokovinin et al. 2015). Corrections for these effects, whether derived from observations of binaries or dense fields, have been particularly effective for systems that are stabilized and rarely removed from the telescope. For many other instruments and telescopes, however, the corrections can vary with time. In such cases, there is rarely enough data to derive a time-dependent correction, so it is easier to model separation and position angle shifts as an extra error term. This method, i.e., modeling systematic errors

from the detector/optics/etc. as an additional error term using binary orbits, is the strategy we adopted here.

We first identified a set of binaries where the orbit can be fit (with <3% errors on the angular separation) without astrometry from the reference being tested. Literature sources using the same instrument and/or from the same paper series were merged for this comparison. We then fit the orbit of each binary following the method outlined in Section 5, using only the least-squares method for efficiency. We compared the expected position angle and separation (predicted from the binary orbit) to the measurements from the reference in question across all measurements and binaries included. For a given reference, we typically had tens or hundreds of orbit residual points, from which we computed a reduced χ^2 (χ^2_ν) for both the separation and position angle, accounting for errors in the orbital parameters. For references with $\chi^2_\nu > 1$, we derived the required missing error term, i.e., the additional error in separation or position angle uncertainty required to yield $\chi^2_\nu = 1$. We show an example of the procedure in Figure 2.

For references where no errors are provided, or for which there is a single uncertainty for all measurements, we adopted our derived uncertainty as the global error for all measurements. For references that report uncertainties for each measurement, we added our value in quadrature with the reported value. The added errors are summarized by reference group in Table 3, and all literature astrometry used in this paper is listed alongside our own measurements in Table 2.

Because the assumed uncertainties of each reference may impact the orbital fit (and hence the residuals of another reference), this process was done over all references twice, each time adjusting the uncertainties as appropriate. References where we could not test the reported errors (e.g., due to insufficient data) and those with extremely large added error terms (>100 mas) were not used. No reference yielded a negative term.

Some earlier studies modeled the extra uncertainty in separation as a fraction (e.g., Hartkopf et al. 2008, 2012; Horch et al. 2011). This is consistent with expectations for plate scale errors, which impact wider binaries more than tighter systems. We found a better fit to separation residuals using a single value than a fraction

Table 3
Literature Astrometry

Reference(s)	$\sigma_{\rm sep}$ (mas)	$\sigma_{\rm P.A.}$ (deg)	Median Sep[a] (mas)	Note
Global Error				
1	4.6	0.85	236	*HST* FGS
2–9	4.3	0.87	184	WIYN/DCT DSSI
10–18	6.4	1.7	161	ICCD Speckle
19–20	10	0.72	683	Palomar
21	45	1.4	390	
22	80	1.9	2080	
23–24	9.9	1.8	208	CTIO/KPNO USNO Speckle
25–32	42	1.1	1060	Speckle at USNO
Extra Term				
33–48	3.1	1.1	161	6 m Speckle
49–50	3.1	0.65	224	Astralux
51	4.9	0.65	168	
52–53	9.4	0.76	365	
54	14	1.6	334	
55	3.4	0.37	327	
56–62	3.8	0.95	179	SOAR Speckle
63	5.0	0.80	342	
64–67	5.9	1.6	123	Speckle interferometry of binaries

Note.
[a] The median separation for all measurements from a given reference used to estimate the uncertainty.

References. (1) Benedict et al. 2016; (2) Horch et al. 2002; (3) Horch et al. 2008; (4) Horch et al. 2010; (5) Horch et al. 2011; (6) Horch et al. 2012; (7) Horch et al. 2015a; (8) Horch et al. 2015b; (9) Horch et al. 2017; (10) Hartkopf et al. 1992; (11) Hartkopf et al. 1994; (12) Hartkopf et al. 1997; (13) Hartkopf et al. 2000; (14) McAlister et al. 1987; (15) McAlister et al. 1989; (16) McAlister et al. 1990; (17) Al-Shukri et al. 1996; (18) Fu et al. 1997; (19) Hełminiak et al. 2009; (20) Martinache et al. 2007; (21) Rodriguez et al. 2015; (22) Geyer et al. 1988; (23) Mason et al. 2018; (24) Mason et al. 2009; (25) Germain et al. 1999; (26) Douglass et al. 2000; (27) Mason et al. 2000; (28) Mason et al. 2002; (29) Mason et al. 2004a; (30) Mason et al. 2004b; (31) Mason et al. 2006; (32) Mason et al. 2011; (33) Balega et al. 1991; (34) Balega et al. 1994; (35) Balega et al. 1997; (36) Balega et al. 1999; (37) Balega et al. 2001; (38) Balega et al. 2002a; (39) Balega et al. 2002b; (40) Balega et al. 2004; (41) Balega et al. 2005; (42) Balega et al. 2006; (43) Balega et al. 2007b; (44) Balega et al. 2007a; (45) Balega et al. 2013; (46) Docobo et al. 2006; (47) Docobo et al. 2008; (48) Docobo et al. 2010; (49) Janson et al. 2012; (50) Janson et al. 2014; (51) Forveille et al. 1999; (52) Hartkopf et al. 2008; (53) Hartkopf & Mason 2009; (54) Jódar et al. 2013; (55) Köhler et al. 2012; (56) Tokovinin et al. 2010; (57) Hartkopf et al. 2012; (58) Tokovinin et al. 2014; (59) Tokovinin et al. 2015; (60) Tokovinin et al. 2016; (61) Tokovinin 2017; (62) Tokovinin et al. 2018; (63) Seifahrt et al. 2008; (64) Blazit et al. 1987; (65) Bonneau et al. 1986; (66) McAlister et al. 1983; (67) McAlister et al. 1984.

of the separation (the right panel of Figure 2 shows one example). This may be because other effects, such as DAR and field distortion, are as important as plate scale errors. In particular, fractional errors tend to underestimate the uncertainty for the smallest separations. However, because of the relatively narrow range of separations considered here, the two methods gave similar results, and our uncertainties were relatively consistent with these earlier studies. Mason et al. (2007), for example, compared the separation and position angle predictions from the
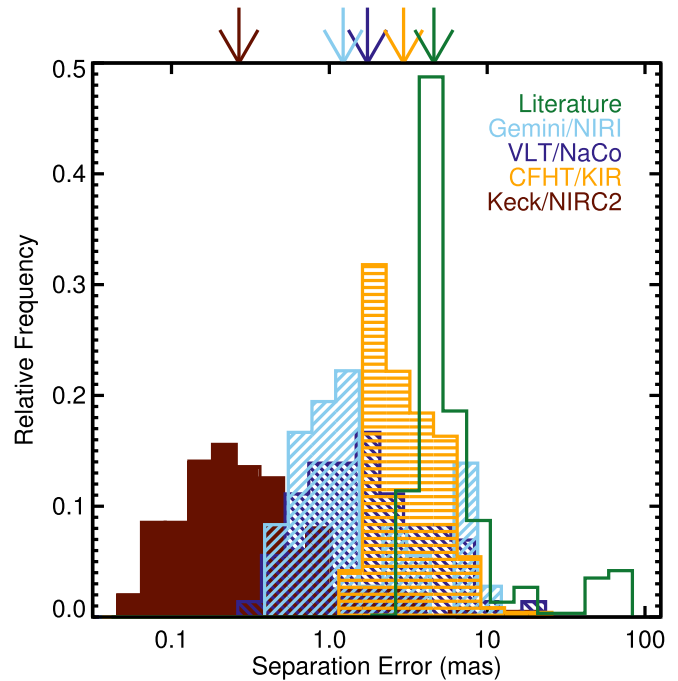
Figure 3. Comparison of input errors on separation for all astrometry used in our analysis by source (see Section 3). Arrows on the top *X*-axis denote the median for each source. Keck/NIRC2 astrometry significantly outperforms other sources and is the most critical for our analysis. Note that bins are spaced logarithmically to show the full range of separation uncertainties.

"Speckle Interferometry at USNO" paper series to a set of well-characterized orbits and found a scatter of 1°.1–1°.2 in position angle and 2.2%–5.6% in separation. For the typical separations we used in this series ($\simeq 1''$), this is consistent with our own determination of 1°.2 and 37 mas (Table 3). To aid with such comparisons, in Table 3 we included the typical separation from each reference used for our uncertainty estimates.

4.2. Summary of Input Astrometry

In total we measured or gathered 1142 unique data sets (unique filter/night/target combinations), approximately half of which we measured from AO images (541), whereas the other half were drawn from the literature (597). Most of the astrometry measurements derived from our analysis came from either Keck/NIRC2 (198) or CFHT/KIR (239), with a smaller contribution from VLT/NaCo (72) and Gemini/NIRI (36).

Although data from NIRC2 represent only $\lesssim 20\%$ of the total astrometric measurements, they are critical in constraining orbital parameters. NIRC2 astrometry was typically an order of magnitude more precise than those from the literature, and a factor of 3–8 more precise than those from KIR, NIRI, and NaCo (Figure 3). In addition to improved Strehl provided by a larger telescope, NIRC2 is rarely removed from the telescope and therefore has a stable and extremely well-characterized distortion solution and pixel scale. Terms we treat as uncertainties for much of the literature astrometry are modeled out for NIRC2 observations. Instruments like NaCo are also capable of achieving astrometry with similar levels of precision (e.g., Reggiani et al. 2016). However, this requires astrometric calibrators observed in the same run, which were not available for most data sets analyzed here.

We characterized the relative importance of each data source using the total number of unique separation measurements weighted by their uncertainties ($1/\sigma$). Under this metric, the NIRC2 points contributed significantly more orbital information than the literature data (77% of the total weight from NIRC2 vs. 9% from the literature). Measurements from KIR (7%) had a comparable total contribution to the literature data, each of which had $\simeq 2$–$3\times$ the weight of measurements from NaCo (4%) and NIRI (3%).

A comparison based on measurement errors alone significantly underestimates the importance of data sampling and orbital coverage. Literature and archive images tended to be concentrated on the best-characterized systems, while the NIRC2 observations were specifically coordinated to complete orbits and cover under- or unsampled regions of binary orbits. The literature data, however, provide the largest baseline. Over all observations used in our analysis, NIRI data spanned 6.5 yr, compared to 9.1 yr covered by KIR, 13.8 yr by NACO, 16.3 from NIRC2, and 68.9 yr from the literature. The NIRC2 data were also heavily concentrated in a single 3 yr window (2015–2018). While a significant fraction of the baseline in the literature astrometry came from a single target (Gl 65), literature data covered 37.2 yr even when this target is excluded. The long baseline provided by the literature astrometry was crucial for analyzing systems with multidecade orbital periods, which included the majority of binaries analyzed here.

5. Orbit Fitting

We fit the astrometry following a Bayesian methodology with Keplerian orbits. Our basic technique is outlined in Dupuy & Liu (2017 and references within), which we summarize here. We used the Markov chain Monte Carlo (MCMC) software `emcee` (Foreman-Mackey et al. 2013), a Python implementation of the affine-invariant ensemble sampler (Goodman & Weare 2010). For each system, we explored seven orbital elements: the orbital period (P), combined angular semimajor axis (α_{ang}), eccentricity (e), inclination (i), argument of periastron (ω), position angle of the line of nodes (Ω), and the position angle at 2010 January 1 00:00:00 UT (λ). The variable λ was fit instead of the usual epoch of periastron passage (T_0), because T_0 is undefined for circular orbits and multivalued to aliases of P, both of which cause problems for the MCMC exploration. We converted λ into T_0 after the MCMC chain is complete for reporting purposes.

We applied nonuniform priors of $1/P$, $1/\alpha_{ang}$, and $\sin(i)$ to P, α_{ang}, and i, respectively. All other parameters evolved under uniform priors. Parameters were limited by physical or definitional constraints, e.g., $P > 0$, $0 \leqslant e < 1$, and $0 \leqslant i \leqslant \pi$, but were given no additional boundaries. A summary of the fit parameters, priors, and limits is given in Table 4.

For each run, walkers were initialized with the best-fit orbit determined using `MPFIT` (Markwardt 2009) and a spread in starting values based on the `MPFIT` estimated errors. Each MCMC chain was initially run for 10^5 steps with 100 walkers. We considered a chain converged if the total length was at least 50 times as long as the autocorrelation time (Goodman & Weare 2010). Systems that did not converge were run for an additional 10^6 total steps, which was sufficient for convergence of all systems. We saved every 100 steps in the chain, and the first 10% of each chain was removed for burn-in. Longer

Table 4
Orbit Fit Parameters, Limits, and Priors

Parameter	Limits	Prior
P	$(0, \infty)$	$1/P$
α_{ang}	$(0, \infty)$	$1/\alpha_{ang}$
e	$(0, 1)$	uniform
i	$(0, \pi)$	$\sin(i)$
ω	$(0, 2\pi)$	uniform
Ω	$(0, 2\pi)$	uniform
λ	$(0, 2\pi)$	uniform

burn-in time did not change the final posterior in any significant way, in part because the initial (least-squares) guesses were always near the final answer from the MCMC.

Systems of near-equal mass may have the primary and companion confused, both in our own measurements and also in those taken from the literature. We identified such measurements by eye during the `MPFIT` stage and manually adjusted the position angles before starting the MCMC run. In total $\simeq 16$ measurements were corrected this way, almost all of which were for three systems with contrast ratios close to unity. A more robust solution to this problem would be to feed a double-peaked posterior at the reported value and $\pm 180°$ into the likelihood function. However, in all cases the problematic points were obvious by eye, they had reported Δm consistent with zero, and a simple $180°$ correction completely fixed the orbit.

Overall the quality of our fits was extremely good, with χ_ν^2 values ranging from 0.1 to 2 and a mean cumulative probability (the probability of getting the χ^2 or smaller given the degrees of freedom) of 63% across all targets. We show some example orbital fits in Figure 4 (with the full set in Appendix B) and provide the median orbital parameters in Table 5. Orbits span a wide range in period; the tightest binaries have $P < 1$ yr, while the widest systems have periods of >50 yr. The two systems with $P > 50$ yr (Gl 301 and Gl 277) were also some of the least well characterized. No systems show evidence of period doubling owing to limited sampling, an advantage of using data with a mix of tight ($\lesssim 1$ yr) and widely spaced (>5 yr) astrometry.

As a test of our sensitivity to the assumed priors, we reran the five systems with the fewest astrometry measurements (those most sensitive to prior assumptions) with uniform priors on all parameters. Otherwise, these fits were identical. The resulting orbital parameters agree with those from the fits including the prescribed priors to better than 1σ, suggesting insensitivity to our input priors.

Our orbital fits made heavy use of literature astrometry, many of which had no reported errors. Our method for assigning or correcting errors assumed that all measurements have a common missing error term per source (Section 4.1). It is more likely that errors depend on the separation and contrast ratio, as well as quantities that were not consistently reported, like weather, setup, and observational strategy. Further, this technique assumed an uncorrelated error term. In the case of an erroneous pixel scale or imperfectly aligned instrument, all measurements from a common instrument err in the same direction. In practice, it is difficult to correct for these effects without access to the actual images. The data suggest that this does not impact our results; the final χ_ν^2 values for the best-fit
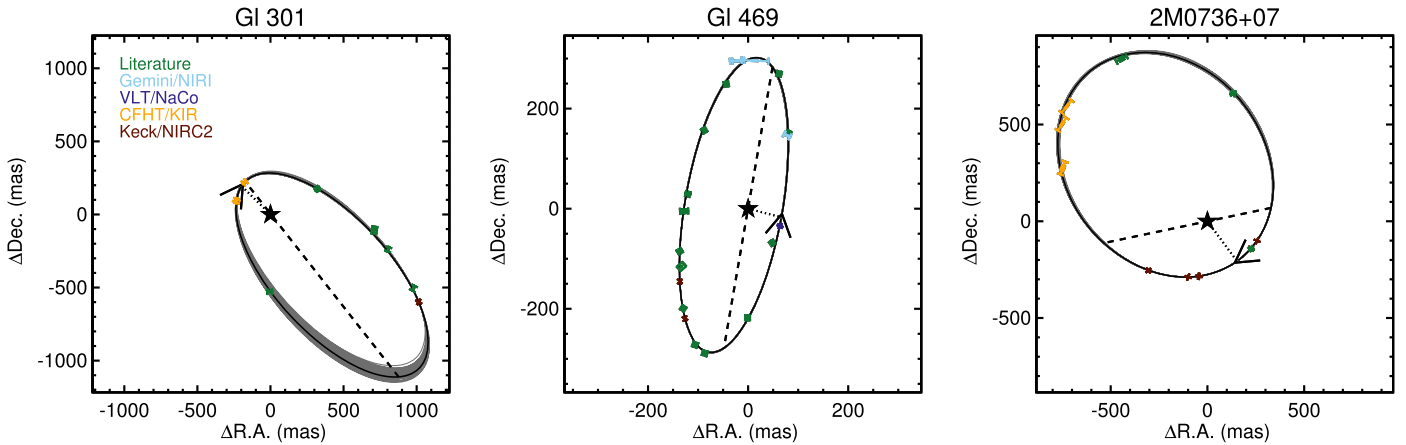
Figure 4. Example results of our orbit-fitting procedure for Gl 301AB (left), Gl 469AB (middle), and 2M0736+07AB (right). Points are individual measurements of the separation and position angle, color-coded by the astrometry source. The black solid line shows the best-fit (highest-likelihood) orbit. Dark-gray lines are drawn by randomly sampling 50 orbit fits from the MCMC chain to display an estimate of the errors. The dotted line connects periastron passage, with an arrow pointing in the orbital direction, and the dashed line indicates the line of nodes. For Gl 469AB, high-quality astrometry is available for the full orbit, and the resulting errors on orbital parameters are so small that the gray lines cannot be seen. All orbits are shown in Appendix A.

orbits show no correlation with the fraction of astrometry from the literature versus our own measurements, and astrometry from our own measurements agrees well with the literature data.

As an additional test, we tried refitting six binaries with the most literature data twice, first doubling the error term added to the literature points and then halving it. In all cases, overall parameters and errors did not change significantly (although the final χ^2_ν values changed). The main reason for this is that our measurements (particularly those from NIRC2) are far more precise and hence dictate the final solution, even in cases where most of the individual measurements are from the literature. In the case of halving errors, the MCMC landed on a similar solution, but with smaller parameter uncertainties and increased χ^2 values. We conclude that our treatment of literature errors does not significantly impact the final orbital fits and that our assigned errors are reasonable.

6. Stellar Parameters

6.1. Parallaxes

Parallaxes for 59 of the 62 systems were drawn from the literature, with the remaining three from MEarth astrometry (detailed below). To avoid complications from astrometric motion impacting the measured parallax, we used parallax determinations that accounted for centroid motion of the binary, or parallax measurements for a nearby associated companion or primary star where possible. Parallaxes from one of these two categories account for nearly half the sample (29 systems). For the other 30 systems with literature parallaxes, we adopted the most precise parallax available excluding values from *Gaia* DR2. While the most precise parallax is not necessarily the most accurate, the majority of systems had only one precise ($<5\%$) parallax in the literature.

Many studies used the weighted mean of all available parallaxes (e.g., Winters et al. 2015) to reduce overall uncertainties. However, excluding the 29 cases above, there are only a few systems where the weighted mean would significantly improve the parallax. Gl 125, as a typical example, has a parallax determination of 63.45 ± 1.94 mas from van Leeuwen (2007) and 77.2 ± 11.6 mas from van

Altena et al. (1995). The weighted mean of these two is 63.82 ± 1.91 mas, a negligible improvement from simply adopting the van Leeuwen (2007) value. More importantly, the weighted mean is only applicable if the parallax measurements are independent. For binaries, the parallax astrometry may be sampling the same systematics owing to centroid motion of the unresolved binary.

For 22 of the systems, we drew parallaxes from the new reduction of *Hipparcos* data (van Leeuwen 2007). We used parallaxes from Dupuy & Liu (2017) for the seven overlapping binaries and from Benedict et al. (2016) for 13. For four systems we pulled parallaxes from the general catalog of trigonometric parallaxes (van Altena et al. 1995), and three were taken from the Tycho-*Gaia* astrometric solution (TGAS or *Gaia* DR1; Gaia Collaboration et al. 2016).

About half (29) of our targets do not have entries in the second data release of *Gaia* (DR2; Lindegren et al. 2018; Gaia Collaboration et al. 2018b). They were likely excluded because centroid shifts from orbital motion prevented a five-parameter (single-star) solution (a requirement to be included in DR2). We also found significant differences between the *Gaia* DR2 values and earlier measurements (including from TGAS) even when measurements were available. Many wide triples or higher-order systems in *Gaia* DR2 (where the wider star is easily resolved) have significantly different parallaxes reported for each set of stars. For example, GJ 2069AC has a *Gaia* parallax of 60.237 ± 0.080 mas, while GJ 2069BD has a *Gaia* parallax of 62.02 ± 0.21 mas, a difference of 1.8 mas (7.9σ). While both AC and BD components are binaries, GJ 2069AC is an eclipsing binary, and it is too tight to have detectable astrometric motion. Orbital motion in GJ 2069BD is likely impacting the parallax measurement or uncertainties, an issue that should be resolved in future *Gaia* data releases that will include fits for orbital motion. We found no such issues with our other parallax sources.

We adopted *Gaia* DR2 parallaxes for five systems, GJ 1245AC, GJ 277AC, Gl 570BC, Gl 667AB, and HIP 111685AB. In each case we used the parallax of their wider common-proper-motion companion. The wider associated stars are not known to harbor another unresolved star, and hence they should not be impacted by the same binarity issue. Gl

Table 5
Orbital Parameters

Name	P (yr)	α_{ang} (mas)	e	i (deg)	ω (deg)	Ω (deg)	T_0 MJD	α_{ang}^3/P^2 (arcsec^3 yr^{-2})	χ^2/dof
GJ 1005	$4.55726^{+0.00075}_{-0.00074}$	$312.85^{+0.50}_{-0.50}$	$0.36136^{+0.00097}_{-0.00098}$	$143.93^{+0.62}_{-0.24}$	$345.26^{+0.62}_{-0.62}$	$61.23^{+0.41}_{-0.41}$	$58172.9^{+1.9}_{-1.9}$	$(1.4743 \pm 0.0072) \times 10^{-3}$	85.9/67
GJ 2005	$17.296^{+0.011}_{-0.011}$	$463.36^{+0.57}_{-0.56}$	$0.02900^{+0.00093}_{-0.00091}$	$62.816^{+0.050}_{-2.2}$	$143.3^{+2.4}_{-2.2}$	$11.798^{+0.084}_{-0.085}$	59158^{+42}_{-40}	$(3.326 \pm 0.015) \times 10^{-4}$	101.6/85
Gl 22	$15.4275^{+0.0054}_{-0.0054}$	$510.26^{+0.74}_{-0.74}$	$0.1576^{+0.0013}_{-0.0013}$	$44.29^{+0.15}_{-0.15}$	$104.90^{+0.53}_{-0.53}$	$176.75^{+0.21}_{-0.21}$	$57447.0^{+5.1}_{-5.2}$	$(5.582 \pm 0.026) \times 10^{-4}$	75.5/65
Gl 54	$1.14434^{+0.00022}_{-0.00022}$	$126.19^{+0.39}_{-0.39}$	$0.1718^{+0.0024}_{-0.0024}$	$125.32^{+0.35}_{-0.35}$	$47.33^{+0.92}_{-0.93}$	$92.04^{+0.40}_{-0.40}$	$58124.0^{+1.1}_{-1.1}$	$(1.534 \pm 0.014) \times 10^{-3}$	37.9/33
GJ 1038	$5.98^{+1.02}_{-0.77}$	$139.7^{+14.5}_{-9.7}$	$0.54^{+0.12}_{-0.11}$	$72.9^{+1.9}_{-2.5}$	174^{+13}_{-16}	$105.9^{+1.6}_{-2.7}$	58313^{+41}_{-1976}	$(7.67 \pm 0.52) \times 10^{-5}$	1.5/9
Gl 65	$26.359^{+0.025}_{-0.024}$	$2049.6^{+3.4}_{-3.4}$	$0.6222^{+0.0015}_{-0.0015}$	$128.09^{+0.15}_{-0.15}$	$283.340^{+0.085}_{-0.084}$	$146.29^{+0.14}_{-0.14}$	$60591.9^{+9.4}_{-9.4}$	$(1.2391 \pm 0.0058) \times 10^{-2}$	96.7/89
Gl 84	$13.328^{+0.037}_{-0.037}$	$495.5^{+1.2}_{-1.2}$	$0.3771^{+0.0082}_{-0.0081}$	$91.771^{+0.056}_{-0.057}$	$245.62^{+0.48}_{-0.48}$	$102.987^{+0.022}_{-0.022}$	61554^{+14}_{-14}	$(6.850 \pm 0.066) \times 10^{-4}$	21.4/17
2M0213+36	$6.419^{+0.067}_{-0.071}$	$161.5^{+1.3}_{-1.3}$	$0.4232^{+0.0039}_{-0.0038}$	$115.30^{+0.24}_{-0.24}$	$207.66^{+0.72}_{-0.73}$	$83.73^{+0.32}_{-0.32}$	$57604.5^{+2.8}_{-2.9}$	$(1.023 \pm 0.016) \times 10^{-4}$	28.8/11
Gl 98	$25.255^{+0.021}_{-0.021}$	$559.84^{+0.66}_{-0.65}$	$0.2354^{+0.0013}_{-0.0013}$	$73.389^{+0.048}_{-0.047}$	$231.49^{+0.21}_{-0.21}$	$109.116^{+0.022}_{-0.022}$	$56417.3^{+4.6}_{-4.7}$	$(2.7509 \pm 0.0098) \times 10^{-4}$	87.6/85
Gl 99	$24.015^{+0.086}_{-0.084}$	$360.53^{+0.72}_{-0.71}$	$0.2087^{+0.0028}_{-0.0025}$	$84.605^{+0.049}_{-0.049}$	$152.6^{+1.9}_{-1.9}$	$98.836^{+0.087}_{-0.090}$	56340^{+43}_{-43}	$(8.126 \pm 0.027) \times 10^{-5}$	23.8/25
Gl 125	$25.67^{+0.20}_{-0.19}$	$534.5^{+2.3}_{-2.3}$	$0.2271^{+0.0044}_{-0.0044}$	$97.186^{+0.026}_{-0.026}$	$181.38^{+0.35}_{-0.36}$	$13.732^{+0.082}_{-0.081}$	64226^{+74}_{-73}	$(2.3173 \pm 0.0098) \times 10^{-4}$	12.6/23
Gl 150.2	$13.604^{+0.045}_{-0.046}$	$254.9^{+1.3}_{-1.3}$	$0.268^{+0.011}_{-0.010}$	$101.79^{+0.38}_{-0.38}$	$250.5^{+1.3}_{-1.3}$	$100.68^{+0.46}_{-0.45}$	58570^{+23}_{-24}	$(8.95 \pm 0.16) \times 10^{-5}$	25.4/19
Gl 190	$0.96380^{+0.00024}_{-0.00024}$	$99.12^{+0.85}_{-0.85}$	$0.2441^{+0.0093}_{-0.0091}$	$92.96^{+0.26}_{-0.25}$	$186.4^{+5.7}_{-5.9}$	$40.42^{+0.17}_{-0.17}$	$58182.4^{+6.5}_{-6.7}$	$(1.048 \pm 0.027) \times 10^{-3}$	25.5/31
GJ 1081	$11.593^{+0.034}_{-0.033}$	$272.9^{+6.8}_{-6.1}$	$0.8612^{+0.0058}_{-0.0055}$	$97.23^{+0.35}_{-0.34}$	$230.5^{+1.5}_{-1.4}$	$51.11^{+0.14}_{-0.14}$	57220^{+18}_{-17}	$(1.51 \pm 0.10) \times 10^{-4}$	25.4/19
Gl 234	$16.5777^{+0.0027}_{-0.0027}$	$1086.04^{+0.27}_{-0.28}$	$0.38229^{+0.00013}_{-0.00013}$	$52.910^{+0.016}_{-0.016}$	$220.942^{+0.020}_{-0.020}$	$30.385^{+0.030}_{-0.030}$	$57342.99^{+0.23}_{-0.23}$	$(4.6612 \pm 0.0033) \times 10^{-3}$	123.2/105
LHS 221	$13.5943^{+0.0062}_{-0.0061}$	$440.9^{+1.6}_{-1.6}$	$0.4777^{+0.0022}_{-0.0022}$	$109.76^{+0.13}_{-0.13}$	$58.59^{+0.21}_{-0.21}$	$107.20^{+0.21}_{-0.21}$	$59671.2^{+2.5}_{-2.5}$	$(4.637 \pm 0.053) \times 10^{-4}$	30.5/49
LHS 224	$3.2860^{+0.0014}_{-0.0014}$	$156.38^{+0.29}_{-0.29}$	$0.2231^{+0.0045}_{-0.0044}$	$131.76^{+0.52}_{-0.53}$	$73.73^{+0.43}_{-0.43}$	$173.93^{+0.81}_{-0.84}$	$58535.0^{+4.9}_{-4.8}$	$(3.541 \pm 0.020) \times 10^{-4}$	19.2/27
Gl 263	$3.6205^{+0.0021}_{-0.0021}$	$143.8^{+2.1}_{-2.0}$	$0.7158^{+0.0065}_{-0.0064}$	$103.28^{+0.36}_{-0.36}$	$287.52^{+0.51}_{-0.51}$	$81.04^{+0.24}_{-0.24}$	$58416.0^{+3.6}_{-3.6}$	$(2.268 \pm 0.099) \times 10^{-4}$	21.9/17
Gl 277	$53.0^{+9.2}_{-7.2}$	1058^{+113}_{-84}	$0.48^{+0.14}_{-0.12}$	$93.53^{+0.48}_{-0.34}$	22^{+332}_{-17}	$10.22^{+0.26}_{-0.44}$	71033^{+12032}_{-3397}	$(4.22 \pm 0.16) \times 10^{-4}$	15.2/13
2M0736+07	$23.768^{+0.048}_{-0.048}$	$633.29^{+0.94}_{-0.93}$	$0.58621^{+0.00060}_{-0.00060}$	$12.3^{+1.0}_{-1.1}$	$66.7^{+5.6}_{-5.3}$	$77.3^{+4.9}_{-5.3}$	$57466.3^{+2.7}_{-2.7}$	$(4.495 \pm 0.019) \times 10^{-4}$	16.8/21
Gl 301	$62.2^{+1.8}_{-1.7}$	875^{+10}_{-10}	$0.6778^{+0.0049}_{-0.0048}$	$52.31^{+0.86}_{-0.87}$	$167.4^{+1.1}_{-1.1}$	$142.0^{+1.1}_{-1.1}$	51189^{+18}_{-18}	$(1.737 \pm 0.049) \times 10^{-4}$	20.1/13
Gl 310	$23.48^{+0.14}_{-0.14}$	$552.6^{+5.6}_{-5.4}$	$0.6976^{+0.0073}_{-0.0074}$	$122.06^{+0.57}_{-0.56}$	$246.72^{+0.36}_{-0.37}$	$49.62^{+0.39}_{-0.38}$	$58432.5^{+5.2}_{-5.1}$	$(3.06 \pm 0.12) \times 10^{-4}$	21.5/11
Gl 330	$32.69^{+0.42}_{-0.40}$	582^{+14}_{-12}	$0.8301^{+0.0071}_{-0.0070}$	$105.78^{+0.51}_{-0.49}$	$309.0^{+1.5}_{-1.5}$	$38.63^{+0.50}_{-0.51}$	64663^{+160}_{-157}	$(1.85 \pm 0.13) \times 10^{-4}$	20.2/17
LHS 6167	$5.0382^{+0.0036}_{-0.0036}$	$198.70^{+0.81}_{-0.81}$	$0.4807^{+0.0034}_{-0.0033}$	$115.78^{+0.19}_{-0.19}$	$92.67^{+0.25}_{-0.21}$	$112.86^{+0.31}_{-0.32}$	$58567.8^{+4.1}_{-4.1}$	$(3.091 \pm 0.034) \times 10^{-4}$	35.2/27
Gl 340	$34.106^{+0.053}_{-0.053}$	$675.7^{+1.4}_{-1.4}$	$0.3084^{+0.0034}_{-0.0033}$	$75.76^{+0.18}_{-0.18}$	$312.57^{+0.51}_{-0.51}$	$24.98^{+0.22}_{-0.22}$	57057^{+20}_{-20}	$(2.652 \pm 0.016) \times 10^{-4}$	43.9/57
Gl 352	$18.449^{+0.025}_{-0.024}$	$638.0^{+2.4}_{-2.4}$	$0.3270^{+0.0034}_{-0.0035}$	$141.78^{+0.60}_{-0.58}$	$287.75^{+0.75}_{-0.73}$	$52.27^{+0.50}_{-0.51}$	59074^{+13}_{-13}	$(7.63 \pm 0.10) \times 10^{-4}$	10.6/15
Gl 381	$7.5731^{+0.0054}_{-0.0055}$	$293.0^{+3.4}_{-3.1}$	$0.7503^{+0.0061}_{-0.0058}$	$93.026^{+0.071}_{-0.073}$	$273.99^{+0.10}_{-0.11}$	$68.523^{+0.047}_{-0.046}$	$57700.6^{+3.8}_{-3.9}$	$(4.39 \pm 0.15) \times 10^{-4}$	35.7/33
Gl 416	$7.2716^{+0.0077}_{-0.0078}$	$184.46^{+0.66}_{-0.59}$	$0.4571^{+0.0037}_{-0.0037}$	$87.25^{+0.24}_{-0.24}$	$154.3^{+1.1}_{-1.2}$	$89.08^{+0.11}_{-0.11}$	58731^{+11}_{-11}	$(1.187 \pm 0.013) \times 10^{-4}$	34.7/23
Gl 469	$11.5515^{+0.0055}_{-0.0055}$	$312.71^{+0.65}_{-0.65}$	$0.2995^{+0.0031}_{-0.0032}$	$108.194^{+0.065}_{-0.065}$	$268.58^{+0.13}_{-0.13}$	$9.81^{+0.13}_{-0.13}$	$58765.8^{+3.4}_{-3.4}$	$(2.292 \pm 0.014) \times 10^{-4}$	27.6/37
Gl 473	$15.826^{+0.017}_{-0.017}$	$919.7^{+1.3}_{-1.3}$	$0.2988^{+0.0012}_{-0.0012}$	$103.09^{+0.14}_{-0.14}$	$349.76^{+0.77}_{-0.77}$	$143.18^{+0.23}_{-0.23}$	60325^{+12}_{-11}	$(3.106 \pm 0.013) \times 10^{-3}$	54.1/51
Gl 494	$13.709^{+0.036}_{-0.037}$	$427.73^{+0.44}_{-0.44}$	$0.2436^{+0.0012}_{-0.0012}$	$130.79^{+0.20}_{-0.20}$	$158.81^{+0.62}_{-0.62}$	$56.13^{+0.17}_{-0.17}$	59365^{+18}_{-18}	$(4.164 \pm 0.029) \times 10^{-4}$	26.1/19
Gl 570	$0.84564^{+0.00021}_{-0.00021}$	$144.2^{+2.3}_{-2.1}$	$0.760^{+0.011}_{-0.011}$	$107.62^{+0.58}_{-0.57}$	$310.4^{+1.3}_{-1.3}$	$16.03^{+0.62}_{-0.64}$	$58305.1^{+1.0}_{-1.1}$	$(4.19 \pm 0.19) \times 10^{-3}$	45.4/49
Gl 600	$2.7808^{+0.0012}_{-0.0012}$	$100.91^{+0.58}_{-0.57}$	$0.3396^{+0.0040}_{-0.0039}$	$34.49^{+0.83}_{-0.85}$	$151.7^{+1.4}_{-1.4}$	$115.8^{+1.3}_{-1.2}$	$57927.9^{+2.8}_{-2.9}$	$(1.329 \pm 0.023) \times 10^{-4}$	31.6/27
Gl 623	$3.7390^{+0.0019}_{-0.0019}$	$238.13^{+0.46}_{-0.45}$	$0.6273^{+0.0019}_{-0.0019}$	$153.15^{+0.38}_{-0.38}$	$247.83^{+0.61}_{-0.62}$	$98.54^{+0.71}_{-0.71}$	$58141.3^{+2.1}_{-2.1}$	$(9.659 \pm 0.050) \times 10^{-4}$	34.7/43
GJ 1210	$14.298^{+0.015}_{-0.015}$	$307.75^{+0.24}_{-0.23}$	$0.48392^{+0.00032}_{-0.00032}$	$112.355^{+0.048}_{-0.048}$	$23.03^{+0.19}_{-0.19}$	$60.610^{+0.069}_{-0.069}$	$59161.4^{+5.7}_{-5.7}$	$(1.4259 \pm 0.0034) \times 10^{-4}$	8.9/17
Gl 660	$34.49^{+0.11}_{-0.10}$	$765.5^{+1.5}_{-1.5}$	$0.1999^{+0.0052}_{-0.0051}$	$19.25^{+0.74}_{-0.73}$	$218.9^{+4.2}_{-4.5}$	$143.5^{+5.3}_{-5.1}$	59799^{+47}_{-45}	$(3.771 \pm 0.029) \times 10^{-4}$	15.9/11
Gl 661	$12.9551^{+0.0043}_{-0.0042}$	$776.12^{+1.01}_{-1.00}$	$0.75167^{+0.00062}_{-0.00062}$	$146.96^{+0.26}_{-0.26}$	$98.31^{+0.57}_{-0.58}$	$159.18^{+0.67}_{-0.67}$	$57730.0^{+1.9}_{-1.9}$	$(2.785 \pm 0.011) \times 10^{-3}$	73.6/69
Gl 667	$42.089^{+0.062}_{-0.063}$	$1824.7^{+5.2}_{-5.1}$	$0.5730^{+0.0034}_{-0.0034}$	$127.57^{+0.22}_{-0.22}$	$68.09^{+0.18}_{-0.19}$	$133.22^{+0.50}_{-0.50}$	$58138.3^{+5.7}_{-5.8}$	$(3.430 \pm 0.031) \times 10^{-3}$	5.1/21
HIP 86707	$20.42^{+0.30}_{-0.27}$	$364.8^{+3.9}_{-3.7}$	$0.539^{+0.012}_{-0.012}$	$104.61^{+0.21}_{-0.21}$	$233.9^{+1.1}_{-1.1}$	$129.31^{+0.25}_{-0.25}$	61701^{+101}_{-90}	$(1.163 \pm 0.022) \times 10^{-4}$	4.4/11
Gl 695	$43.46^{+0.23}_{-0.23}$	$1402.0^{+6.0}_{-6.0}$	$0.1834^{+0.0031}_{-0.0031}$	$65.821^{+0.098}_{-0.098}$	$172.21^{+0.48}_{-0.46}$	$61.11^{+0.80}_{-0.79}$	54592^{+13}_{-13}	$(1.459 \pm 0.014) \times 10^{-3}$	20.7/23
Gl 747	$5.74693^{+0.00050}_{-0.00049}$	$292.78^{+0.33}_{-0.33}$	$0.25509^{+0.00033}_{-0.00033}$	$77.377^{+0.031}_{-0.031}$	$330.47^{+0.21}_{-0.21}$	$84.702^{+0.022}_{-0.022}$	$58827.9^{+1.3}_{-1.3}$	$(7.599 \pm 0.026) \times 10^{-4}$	78.5/65
Gl 748	$2.47609^{+0.00029}_{-0.00029}$	$146.38^{+0.45}_{-0.46}$	$0.4565^{+0.0018}_{-0.0018}$	$131.82^{+0.42}_{-0.40}$	$24.26^{+0.60}_{-0.60}$	$177.15^{+0.39}_{-0.39}$	$58171.0^{+1.0}_{-1.0}$	$(5.116 \pm 0.048) \times 10^{-4}$	69.2/69

Table 5
(Continued)

Name	P (yr)	α_{ang} (mas)	e	i (deg)	ω (deg)	Ω (deg)	T_0 MJD	$\alpha_{\mathrm{ang}}^3/P^2$ (arcsec^3 yr^{-2})	χ^2/dof
Gl 762.1	$1.35355^{+0.00019}_{-0.00020}$	$80.75^{+0.66}_{-0.63}$	$0.3903^{+0.0074}_{-0.0070}$	$147.7^{+2.3}_{-2.1}$	$1.4^{+3.6}_{-4.1}$	$67.1^{+3.0}_{-3.5}$	$58528.8^{+492.9}_{-2.5}$	$(2.874 \pm 0.070) \times 10^{-4}$	30.4/49
Gl 765.2	$11.924^{+0.022}_{-0.022}$	$194.0^{+1.1}_{-1.1}$	$0.2474^{+0.0078}_{-0.0078}$	$80.75^{+0.23}_{-0.23}$	$70.53^{+0.73}_{-0.76}$	$112.57^{+0.40}_{-0.39}$	57759^{+16}_{-16}	$(5.137 \pm 0.088) \times 10^{-5}$	30.3/35
GJ 1245	$16.8943^{+0.0090}_{-0.0090}$	$830.23^{+0.24}_{-0.24}$	$0.34114^{+0.00062}_{-0.00062}$	$135.47^{+0.12}_{-0.12}$	$216.71^{+0.22}_{-0.22}$	$80.37^{+0.15}_{-0.15}$	$57696.0^{+1.1}_{-1.1}$	$(2.0050 \pm 0.0031) \times 10^{-3}$	68.1/69
Gl 791.2	$1.47126^{+0.00035}_{-0.00037}$	$96.53^{+2.04}_{-0.88}$	$0.6350^{+0.0048}_{-0.0088}$	$166.9^{+6.3}_{-9.5}$	94^{+153}_{-60}	265^{+46}_{-163}	$58535.5^{+5.6}_{-531.3}$	$(4.16 \pm 0.22) \times 10^{-4}$	47.1/35
Gl 804	$14.731^{+0.017}_{-0.017}$	$282.0^{+1.3}_{-1.3}$	$0.5928^{+0.0036}_{-0.0037}$	$130.13^{+0.31}_{-0.31}$	$246.41^{+0.11}_{-0.11}$	$79.56^{+0.27}_{-0.26}$	$58543.5^{+1.9}_{-1.9}$	$(1.033 \pm 0.017) \times 10^{-4}$	38.9/33
Gl 831	$1.93198^{+0.00014}_{-0.00014}$	$145.44^{+0.17}_{-0.17}$	$0.38957^{+0.00093}_{-0.00092}$	$49.61^{+0.15}_{-0.15}$	$190.21^{+0.46}_{-0.46}$	$144.21^{+0.22}_{-0.23}$	$58217.57^{+0.69}_{-0.69}$	$(8.242 \pm 0.029) \times 10^{-4}$	84.2/77
Gl 844	$11.798^{+0.067}_{-0.065}$	$306.7^{+2.6}_{-2.5}$	$0.4838^{+0.0075}_{-0.0073}$	$38.21^{+0.86}_{-0.89}$	$267.2^{+1.0}_{-1.1}$	$151.8^{+1.1}_{-1.1}$	$57032.7^{+9.3}_{-9.4}$	$(2.073 \pm 0.050) \times 10^{-4}$	2.9/3
HD 239960	$45.13^{+0.44}_{-0.43}$	2447^{+16}_{-16}	$0.4131^{+0.0031}_{-0.0032}$	$165.41^{+0.72}_{-0.71}$	$208.2^{+2.8}_{-3.3}$	$152.6^{+3.3}_{-3.9}$	56944^{+12}_{-11}	$(7.204 \pm 0.034) \times 10^{-3}$	48.9/41
HIP 111685	$17.236^{+0.019}_{-0.019}$	$337.3^{+1.2}_{-1.2}$	$0.2404^{+0.0032}_{-0.0031}$	$55.57^{+0.27}_{-0.26}$	$116.28^{+0.54}_{-0.55}$	$69.57^{+0.11}_{-0.11}$	60996^{+15}_{-15}	$(1.291 \pm 0.014) \times 10^{-4}$	24.6/33
Gl 893.4	$19.173^{+0.016}_{-0.016}$	$220.44^{+0.41}_{-0.41}$	$0.4395^{+0.0024}_{-0.0024}$	$116.66^{+0.14}_{-0.14}$	$322.48^{+0.55}_{-0.55}$	$29.02^{+0.19}_{-0.19}$	$58454.0^{+7.3}_{-7.2}$	$(2.914 \pm 0.013) \times 10^{-5}$	17.9/25
Gl 900	$36.0^{+1.5}_{-1.4}$	444^{+12}_{-10}	$0.136^{+0.026}_{-0.025}$	$82.21^{+0.23}_{-0.23}$	$109.8^{+7.7}_{-8.5}$	$8.01^{+0.33}_{-0.33}$	54494^{+222}_{-237}	$(6.77 \pm 0.15) \times 10^{-5}$	16.5/15
LHS 4009	$24.7^{+1.9}_{-1.5}$	444^{+23}_{-18}	$0.386^{+0.052}_{-0.054}$	$98.37^{+0.45}_{-0.45}$	$12.0^{+8.1}_{-6.1}$	$10.69^{+0.28}_{-0.31}$	61617^{+656}_{-459}	$(1.445 \pm 0.016) \times 10^{-4}$	9.2/13
Gl 913	$2.3913^{+0.0016}_{-0.0017}$	$116.91^{+0.28}_{-0.27}$	$0.5142^{+0.0020}_{-0.0020}$	$114.20^{+0.19}_{-0.19}$	$306.66^{+0.24}_{-0.24}$	$112.30^{+0.23}_{-0.23}$	$58412.9^{+1.0}_{-1.0}$	$(2.795 \pm 0.019) \times 10^{-4}$	18.8/5

(This table is available in its entirety in machine-readable form.)

695BC, GJ 2005BC, Gl 22AC, and 2M1047+40 also have nearby associated stars. However, GJ 2005A has no entry in *Gaia* DR2, the *HST* parallax for Gl 695BC is more precise than the *Gaia* DR2 value for Gl 695A, GJ 22B does not pass the cuts on *Gaia* astrometry suggested in Lindegren et al. (2018) and Gaia Collaboration et al. (2018a), and the wide companion to 2M1047+40 is itself a tight binary (LP 213-67AB; Dupuy & Liu 2017) with a large reported excess astrometric noise in *Gaia* (a sign of binarity; Evans 2018).

For three systems we derived new parallaxes using MEarth astrometry (Nutzman & Charbonneau 2008). Updated parallaxes were measured following the procedure from Dittmann et al. (2014). The only difference was that we used ≃two additional years of data, which helps average out systematic errors arising from centroid motion due to the binary orbit and significantly reduces the overall uncertainties.

The remaining five systems had parallaxes from a range of other literature sources, each containing just one system in our sample. All adopted parallaxes and references are listed in Table 1.

6.2. Metallicity

We estimated [Fe/H] using our SpeX spectra and the empirical relations from Mann et al. (2013a) for K5–M6 dwarfs and from Mann et al. (2014) for M6–M9 dwarfs. These relations are based on the strength of atomic lines (primarily Na, Ca, and K features) in the optical or NIR (e.g., Rojas-Ayala et al. 2010; Terrien et al. 2012), empirically calibrated using wide binaries containing a solar-type primary and an M dwarf companion (e.g., Bonfils et al. 2005; Johnson & Apps 2009; Neves et al. 2012). The calibrations were based on the assumption that components of such binaries have similar or identical metallicities (e.g., Teske et al. 2015). Similar methods have been used extensively to assign metallicities across the M dwarf sequence (e.g., Muirhead et al. 2015; Terrien et al. 2015b; Dressing et al. 2017; Mace et al. 2018; Van Grootel et al. 2018). Final adopted [Fe/H] values are given in Table 1. Errors account for Poisson noise in the spectrum, but because of the relatively high S/N of the spectra, final errors on [Fe/H] are generally dominated by the uncertainties in the calibration itself, conservatively estimated to be 0.08 dex (Mann et al. 2013a, 2014). However, we estimated that we can measure relative [Fe/H] values (one M dwarf compared to another) to 0.04 dex.

For all but two systems (Gl 65 and HD 239960), our NIR spectra are for the combined flux of the binary components. Mann et al. (2014) explored the issue of measuring metallicities of binaries with unresolved data by combining spectra of single stars with equal metallicities and reapplying the same calibration. The bias introduced is negligible (≲0.02 dex) when compared to overall uncertainties. The additional scatter is smaller than the measurement uncertainties and can be explained entirely by Poisson noise introduced in the addition of component spectra. This may be more complicated for nearly or marginally resolved systems, where the narrow slit (0.″3) is preferentially including light from one star. However, repeating the tests of Mann et al. (2014) and adding a random flux weighting to the fainter star produced only a small increase in the uncertainties (0.01–0.03 dex).

Two systems (2M2140+16 and 2M2206−20) have SpeX spectra taken with a wider slit, yielding lower spectral resolution. The bands in Mann et al. (2014) are defined using

a homogeneous data set taken with the narrow (0.″3) slit, so this difference may impact the derived [Fe/H]. We tested this by convolving a set of single-star SpeX spectra taken with the 0.″3 slit with a Gaussian to put them at the appropriate lower resolution. The median of the derived [Fe/H] values changed by <0.01 dex, but the change varies between targets. Based on the resulting scatter, we estimate the errors on [Fe/H] from the lower-resolution spectra to be 0.12 dex on a solar scale and 0.08 dex on a relative scale. These systems are marked separately in Table 1.

Two of the systems in our sample are L dwarfs (2M0746+20 and 2M1017+13). These are most likely above the hydrogen-burning limit and hence were included in our analysis. However, the Mann et al. (2014) method contained no L dwarf calibrators. Our derived [Fe/H] were extrapolations of the Mann et al. (2014) calibration. The Mann et al. (2014) calibration has only a weak dependence on spectral type, but we still advise treating the assigned values with skepticism until an L dwarf calibration becomes available.

Three targets (Gl 792.1, Gl 765.2, and Gl 667) are too warm (earlier than K5) for the calibration of Mann et al. (2013a). For Gl 667, we adopted the [Fe/H] from Gaidos & Mann (2014) for the associated M dwarf companion Gl 667C. [Fe/H] measurements from Gaidos & Mann (2014) are determined in the same way as applied to other targets as explained above. For the other two, we took [Fe/H] values from Casagrande et al. (2011) and Torres et al. (2010), respectively. These [Fe/H] measurements are not necessarily on the same scale as those from Mann et al. (2013a), which are calibrated against abundances of Sun-like stars from Brewer et al. (2015, 2016). Given reported variations in [Fe/H] for these stars, as well as [Fe/H] determination differences (Hinkel et al. 2014, 2016), we adopted conservative 0.08 dex uncertainties on both systems. For the other target lacking a SpeX spectrum (Gl 54), we derived [Fe/H] using the optical calibration of Mann et al. (2013a) and a moderate-resolution optical spectrum taken from Gaidos et al. (2014).

6.3. K_S Magnitudes

To determine K_S magnitudes for each component, we required both unresolved (total) K_S for each system and the contrast (ΔK_S) for each component. We adopted unresolved K_S magnitudes from the Two Micron All Sky Survey (2MASS; Skrutskie et al. 2006). Some of the brightest stars in our sample are near or beyond saturation in 2MASS. For these targets we recalculated K_S magnitudes using available optical and NIR spectra, following the method of Mann & von Braun (2015) and Mann et al. (2015), using available optical spectra from Gaidos et al. (2014). Synthetic magnitudes were broadly consistent (mean difference of 0.003 ± 0.002 mag) with 2MASS K_S magnitudes (and at similar precision) for fainter targets ($K_S > 7$). We only updated K_S magnitudes for bright systems where our synthetic photometry differed from the 2MASS value by more than 2σ or the 2MASS photometry was saturated (five systems). We mark these systems in Table 1.

Reddening and extinction are expected to be ≃0 for all targets, as the most distant system is at 35 pc, while the Local Bubble (a region of near-zero extinction) extends to ≃70 pc (Aumer & Binney 2009). Hence, we did not apply any extinction correction to the adopted K_S values.

To compute ΔK_S, we used component contrast measurements from our AO data (Section 4). We utilize any contrast taken with a filter centered in the K band, which included K_s, K, and K' (K_p or
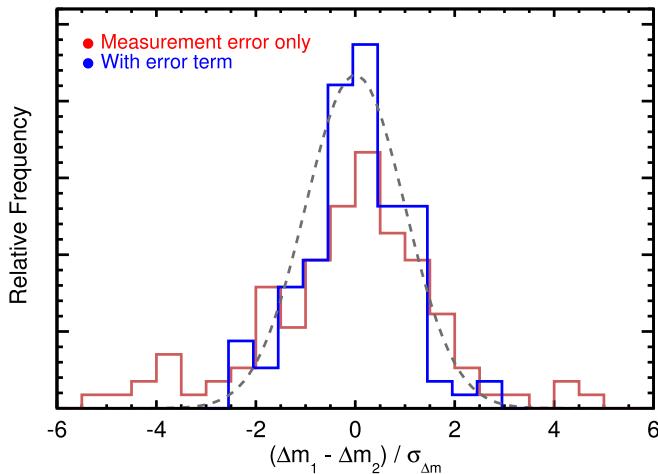
Figure 5. Distribution of contrast ratio differences (in units of standard deviations) for data taken on the same target, and with the same filter and instrument, but in different nights. The red line is before adding the missing error term, while the blue line shows the distribution after adding this. The gray dashed line shows the expected normal distribution. The histograms are offset slightly for clarity, although identical bins are used as input.

K-prime), as well as narrowband filters Brγ and K_c (K_{cont} or K-continuum). While all targets considered here had at least one measurement in one of these filters, none of the response functions used were a perfect match to 2MASS K_S. We transformed each K-band contrast into 2MASS contrasts (ΔK_S) using corrections derived from flux-calibrated spectra as detailed in Appendix A. These corrections were generally small ($\lesssim$0.1 mag).

After converting all contrast measurements to ΔK_S, we combed multiple measurements using the robust weighted mean. Errors on contrasts for each data set were taken to be the rms in flux measurements among consecutive images. These errors may be underestimated because of imperfect PSF modeling, flat-fielding, uncorrected nonlinearities in the detector, and intrinsic variability of the star. To test for this, we compared ΔK_X measurements of the same star using the same filter and instrument but on different nights (Figure 5). The comparison suggested a missing error term of 0.016 mag for NIRC2, 0.02 for KIR and NaCo, and 0.03 for NIRI. We did not split this into separate error terms per filter; many filters do not have enough multiepoch data on their own, and a single error term across all filters for a given instrument gave a reasonable fit. We included this term as an additional error term common to all measurements in our final computation of ΔK_S.

For GJ 2005BC and Gl 900BC, the 2MASS PSF included flux from the A component. In both cases, we used our AO data to measure ΔK_S between all three components. The total K_S magnitudes given in Table 1 already have the A components removed.

7. The Mass–Luminosity Relation

7.1. Methodology

For main-sequence stars, the mass–luminosity relation traditionally takes the form

$$\frac{L_*}{L_\odot} = C \left(\frac{M_*}{M_\odot} \right)^\alpha, \tag{1}$$

where α depends on the dominant energy transport mechanism (e.g., radiative versus convective) and internal structure of the star (Hansen et al. 2004).

We rewrite Equation (1) in terms of M_{K_S} instead of L_*. Absolute magnitudes are more easily measured than overall luminosity and avoid introducing errors from uncertain bolometric corrections or the need to take flux-calibrated spectra in order to measure the bolometric flux directly. Switching to M_{K_S} also mitigates effects of abundance differences. The K band is heavily dominated by metal-insensitive CO and H_2O molecular absorption bands. Optical bands are dominated by much stronger molecular bands (e.g., TiO, CO, CaH, MgH, and VO) that are sensitive to both [Fe/H] and [α/Fe] (Figure 6; see also Woolf & Wallerstein 2006; Lépine et al. 2007; Mann et al. 2013a).

Our sample encompassed almost an order of magnitude in mass and hence a range of underlying stellar physics. No single power law is expected to fit over the full sequence. Instead, we assumed that α depends on M_{K_S}, which we approximated as a polynomial. This yields an M_{K_S}–M_* relation of the form

$$\log_{10}\left(\frac{M_*}{M_\odot} \right) = \sum_{i=0}^{n} a_i (M_{K_S} - zp)^i, \tag{2}$$

where a_i are the fit coefficients. The order of the fit (n) was determined using the Bayesian Information Criterion (BIC). The constant zp is a zero-point (or anchor) magnitude, which is defined to be 7.5. This approximately corresponded to the logarithmic average mass of stars in our sample. The zero-point was effectively a coordinate shift, was not constrained by the fit, and did not impact the final result (a test fit with no zero-point gave consistent results). However, a value representative of the sample helped reduce the number of significant figures required for the a_i values and improved fit convergence time.

The true relation between between α and M_{K_S} is likely more complicated than Equation (2) and may depend on other astrophysical parameters (e.g., activity). We explore the impact of using this model in Section 7.4 and the role of [Fe/H] on the relation in Section 7.5. More complicated astrophysical effects are included as an additional error term (discussed below).

For the left-hand side of Equation (2), we computed the total dynamical mass ($M_{tot,dyn}$) for each binary. To this end, we combined the orbital period (P) and total angular semimajor axis (α_{ang}) from our fits to the orbital parameters (Section 5) with the parallax determinations (π, Section 6.1) following a rewritten form of Kepler's laws:

$$M_{tot,dyn} = M_1 + M_2 = \frac{(\alpha_{ang}/\pi)^3}{P^2}, \tag{3}$$

where P is in years, α_{ang} and π are in arcseconds, and M_{tot} is in solar masses.

Equation (3) provides only the total mass of a given binary system, as opposed to individual/component masses used in earlier work on the M_{K_S}–M_* relation. Thus, when fitting for the a_i coefficients, we performed the comparison between the predicted ($M_{tot,pre}$, from the M_{K_S}–M_* relation) and dynamical total mass (M_{tot}, from Equation (3)) for each system. For this, we rewrote Equation (2) to obtain an expression for the total mass predicted by the relation ($M_{tot,pre}$)

$$M_{tot,pre} = 10^{\sum_{i=0}^{n} a_i (M_{K_S,2} - zp)^i}$$
$$+ 10^{\sum_{i=0}^{n} a_i (M_{K_S,1} - zp)^i}, \tag{4}$$

where $M_{K_S,1}$ and $M_{K_S,2}$ are the primary and companion absolute K_S-band magnitudes derived from our measured ΔK_S and unresolved K_S magnitudes (Section 6.3). Note that while the
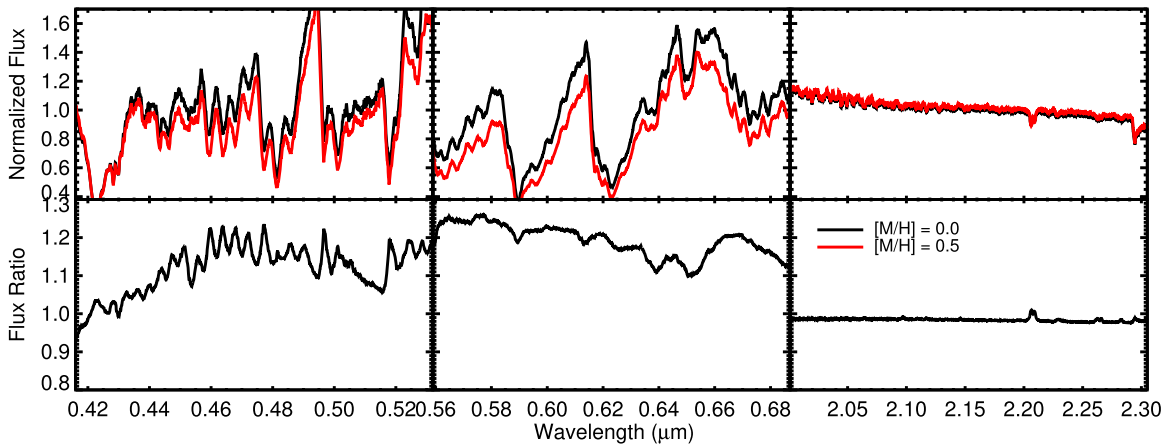
Figure 6. Effect of changes in [M/H] on a model spectrum at $T_{eff} = 3200$ K, $\log(g) = 5$ in g (left), r (middle), and K band (right). The top panel shows [M/H] $= 0$ (black) and [M/H] $= +0.5$ (red) spectra from the CFIST BT-SETTL models (Allard et al. 2012). The bottom panel shows the ratio of the two, highlighting how small an effect [M/H] has in the K band compared to optical regions. The one feature that stands out in the K band is the Na doublet, which is commonly used as a metallicity diagnostic for dwarfs (Rojas-Ayala et al. 2010; Terrien et al. 2012; Newton et al. 2014) and a gravity diagnostic for pre-main-sequence stars (e.g., Schlieder et al. 2012).

M_{K_S}–M_* relation is designed to make predictions for the masses of single stars from their M_{K_S} magnitudes, because we have resolved magnitudes we can combine predictions for the individual mass of each component into a prediction for $M_{tot,pre}$, which can be compared directly to $M_{tot,dyn}$. In this way we could solve for the a_i coefficients in the M_{K_S}–M_* relation without using individual masses or mass ratios. We also note that Equation (4) could be modified for arbitrarily higher-order star systems, providing individual M_{K_S} magnitudes, and the total mass of the system is known.

We fit for the a_i terms in Equation (4) using the MCMC code emcee, which accounts for the strong covariance between coefficients and provides a robust estimate of the uncertainties on the derived relation by exploring a wide range of allowed fits. Each coefficient was allowed to evolve under uniform priors without limits and was initialized with the best-fit value derived from MPFIT. We ran the MCMC chain with 500 walkers for 10^6 steps after a burn-in of 50,000 steps. We ran separate MCMC chains testing values of n (fit order) from 3 to 7. Initial a_i values were taken from a least-squared fit using MPFIT.

Errors on $M_{tot,dyn}$ and $M_{tot,pre}$ values are correlated to each other owing to a common parallax. $M_{tot,dyn}$ estimates scale with the cube of the parallax (Equation (3)). As a result, the parallax was a major source of uncertainty on $M_{tot,dyn}$ for many systems. Similarly, our component K_S magnitudes had relatively small errors (0.016–0.06 mag), so M_{K_S} errors tended to be dominated by the parallax. Because this correlation is usually along (parallel to) the direction of the M_{K_S}–M_* relation (a greater distance increases both $M_{tot,dyn}$ and $M_{tot,pre}$), it can tighten the fit if properly taken into account (when compared to assuming uncorrelated errors).

We wanted the MCMC to explore the full "ellipse" representing the correlation between M_{K_S} and M_* for each binary. To this end, we treated the distance of each system as a free parameter, letting each evolve under a prior from the observed parallaxes. The MCMC was fed a''^3/P^2 and K_S (with uncertainties) for each system, from which $M_{tot,dyn}$ and M_{K_S} were calculated using the common parallax. We converted M_{K_S} into $M_{tot,pre}$ for each binary, which we compared to the

corresponding $M_{tot,dyn}$ values within the likelihood function. Thus, the MCMC is forced to explore the range of possible parallaxes consistent with the input Gaussian uncertainties, while both $M_{tot,dyn}$ and $M_{tot,pre}$ shifted in a correlated way owing to changes in the (shared) parallax. Since the orbital information provides no direct constraint on the distances, this method effectively forced the MCMC to explore a distribution along the input prior.

For computational efficiency, we assumed Gaussian errors on α_{ang}^3/P^2. Although α_{ang} and P were often correlated and non-Gaussian, posteriors of α_{ang}^3/P^2 were all well described by a Gaussian (Figure 7).

For main-sequence dwarfs at fixed metallicity, more massive stars should always be brighter. Thus, we required that the resulting fit have a negative derivative (higher M_{K_S} always gives a smaller $M_{tot,pre}$) over the full range of input objects considered. We tested running without this constraint and found similar results over most of the parameter range considered. The major difference was near the edges of the input sample. Without the negative derivative constraint, the fit could become double valued where there were few points.

We specifically explore the role of [Fe/H] on the relation in Section 7.5, but other astrophysical effects, such as detailed abundances and activity/rotation/magnetic fields, are not explicitly modeled in our fit and hence may increase the overall scatter in the M_{K_S}–M_* relation. We modeled these effects as an additional dimensionless parameter, σ_e. In addition to missing astrophysical variance, additional variation modeled by σ_e could come from underestimated uncertainties in our input parallaxes (e.g., due to uncorrected orbital motion on the astrometry) or orbital parameters. In either case, it is critical to include σ_e as a free parameter to avoid underestimating the final uncertainties in the final relation. We implemented σ_e as a fractional uncertainty in the total mass, added to the measurement uncertainty (from the orbit and parallax errors) in quadrature. We also tested including σ_e as an additional uncertainty in the parallax (broadening the priors), or in the assigned K-band magnitudes. We discuss the differences between these implementations in Section 7.2.

To briefly summarize, each step of the MCMC chain included the following components:
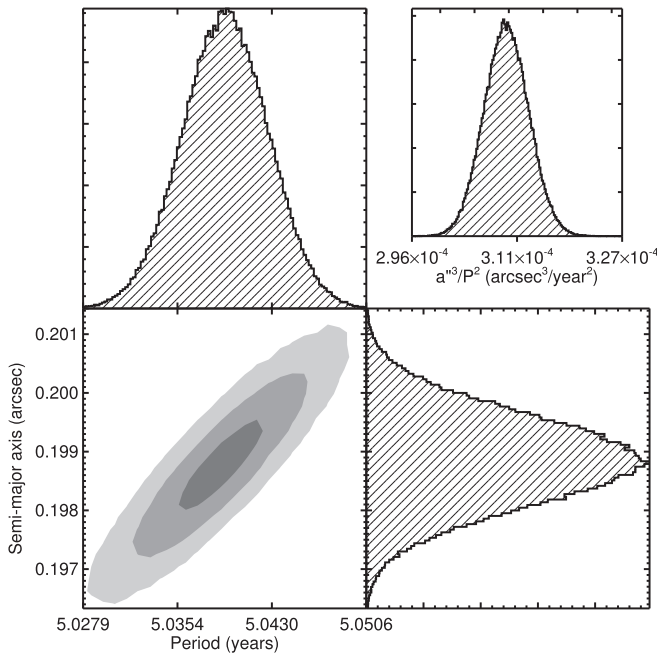
Figure 7. Example joint posterior on semimajor axis and orbital period (bottom left) for the system LHS 6167. Gray regions show 1σ, 2σ, and 3σ (from darkest to lightest) of the points. The histograms above and to the right show the 1D distributions of each parameter. The parameter fed into the M_{K_S}–M_* fit is $\alpha_{\mathrm{ang}}^3/P^2$ (in arcsec^3 per yr^2), which is shown in the top right inset.

1. We assumed an M_{K_S}–M_* relation following Equation (2). The first iteration used seed guesses for the a_i coefficients from a least-squared fit.
2. From the measured ΔK_S, unresolved K_S magnitudes, and input parallaxes, we computed M_{K_S} for each of the 124 stars, as well as uncertainties arising from errors in ΔK_S and K_S.
3. We applied the M_{K_S}–M_* relation from the first step to compute 124 individual mass estimates.
4. We summed the component masses in each binary, providing predictions for the total masses ($M_{\mathrm{tot,pre}}$) of each of the 62 systems and corresponding uncertainties.
5. To handle any missing uncertainties or intrinsic variation in the M_{K_S}–M_* relation, we inflated uncertainties on $M_{\mathrm{tot,pre}}$ by a fraction, σ_e. σ_e was treated as a free parameter and was initially set to $\simeq 0$.
6. Using the input orbital parameters ($\alpha_{\mathrm{ang}}^3/P^2$) for each system and the same parallaxes used for computing each M_{K_S}, we computed a total dynamical mass ($M_{\mathrm{tot,dyn}}$) for each binary system (see Equation (3)).
7. We calculated the likelihood, which is the χ^2 difference between all predicted total masses (from the relation) and total dynamical masses multiplied by uniform priors for a_i and σ_e and the Gaussian priors on each parallax.
8. Based on the log-likelihood, emcee adjusted the a_i coefficients, σ_e, and parallaxes for all systems and repeated the process.

We emphasize that the comparison was done completely in total mass; the fitting method included no assumptions about the mass ratio, nor were mass ratios needed to fit the a_i coefficients or σ_e. The fit was done using just π, $\alpha_{\mathrm{ang}}^3/P^2$, K_S, and Δ_{K_S} for each system. We address potential biases from

using total masses (instead of individual masses) in Sections 7.3 and 7.4.

7.2. Results and Uncertainties

We show the resulting posteriors for the polynomial coefficients (a_i) in Figure 8. The final fit was tightly constrained over the full sequence, which we show for individual masses in Figure 9 and for combined masses in Figure 10. For the former figure, we have assumed a mass ratio for each system from the M_{K_S}–M_* relation, i.e., the ratio of the two predicted masses given their individual M_{K_S} (see Sections 6.1 and 6.3 for more details). These ratios were not used in the fit and have strongly correlated uncertainties given a common parallax and total K_S. Thus, we only used these mass ratios for displaying the relation. The latter figure (Figure 10) is a more realistic representation of how the MCMC fit for M_{K_S}–M_* was done (i.e., comparing $M_{\mathrm{tot,dyn}}$ to $M_{\mathrm{tot,pre}}$).

Coefficients for powers of the same parity (even or odd) were strongly correlated to each other. This was expected, as a decrease in the slope (from linear) is best explained using an odd power, and an increase with an even power. Coefficients for powers with even parity (with the exception of the a_0 term) were generally centered around zero. This also was expected in the context of the shape of the relation seen in Figure 9 and our requirement that the mass always decrease with decreasing luminosity. A power with even parity will prefer to turn upward at low masses. We investigated this further by redoing the fit with no even powers (a_0 was retained), but exploring higher-order odd powers. The resulting fit was significantly worse, with a σ_e value twice as large as fits with the same number of free parameters including even powers. The resulting fits also showed significant systematic deviations from the empirical data for $0.3\,M_\odot < M_* < 0.5\,M_\odot$. We opted to include the even orders for all analyses despite their near-zero values.

We adopted $n = 5$ as the preferred solution based on both the BIC values and visual inspection of the residuals. Lower-order fits did a reasonable job fitting most of the sequence but poorly reproduced the masses of objects with $M_* < 0.085\,M_\odot$. In this regime, the relation becomes increasingly nonlinear. The result is that lower-order fits systematically underestimate masses of the coolest objects in our sample (Figure 11) and tend to overestimate σ_e to compensate. Higher-order ($n > 5$) fits explain the data well but were not justified statistically (e.g., marginal decrease in σ_e) and showed slope changes outside the calibration sample that are not expected by theoretical considerations.

The three different implementations of σ_e were broadly consistent with each other. For example, implementing σ_e as broadening on the parallax priors yielded an extra error $\gtrsim 1/3$ that of implementing it on the final mass. Since the parallax term is cubed in the total mass calculation (Equation (3)), these are functionally equivalent (although parameter correlation forces a slightly larger error in the parallax). However, we found that implementing σ_e as an error on the total mass best explained the data. Taking σ_e as an error on the K-band magnitude led to a χ_ν^2 value too low when just considering stars below $0.25\,M_\odot$ and too high for stars above $0.5\,M_\odot$, while applying χ_ν^2 as an error on the total mass yielded χ_ν^2 closer to 1 over the whole mass range. Taking σ_e as an error on M_* is also easily implemented when applying the relation.

We list the best-fit (highest-likelihood) coefficient values in Table 6, as well as the median value of σ_e and BIC values for
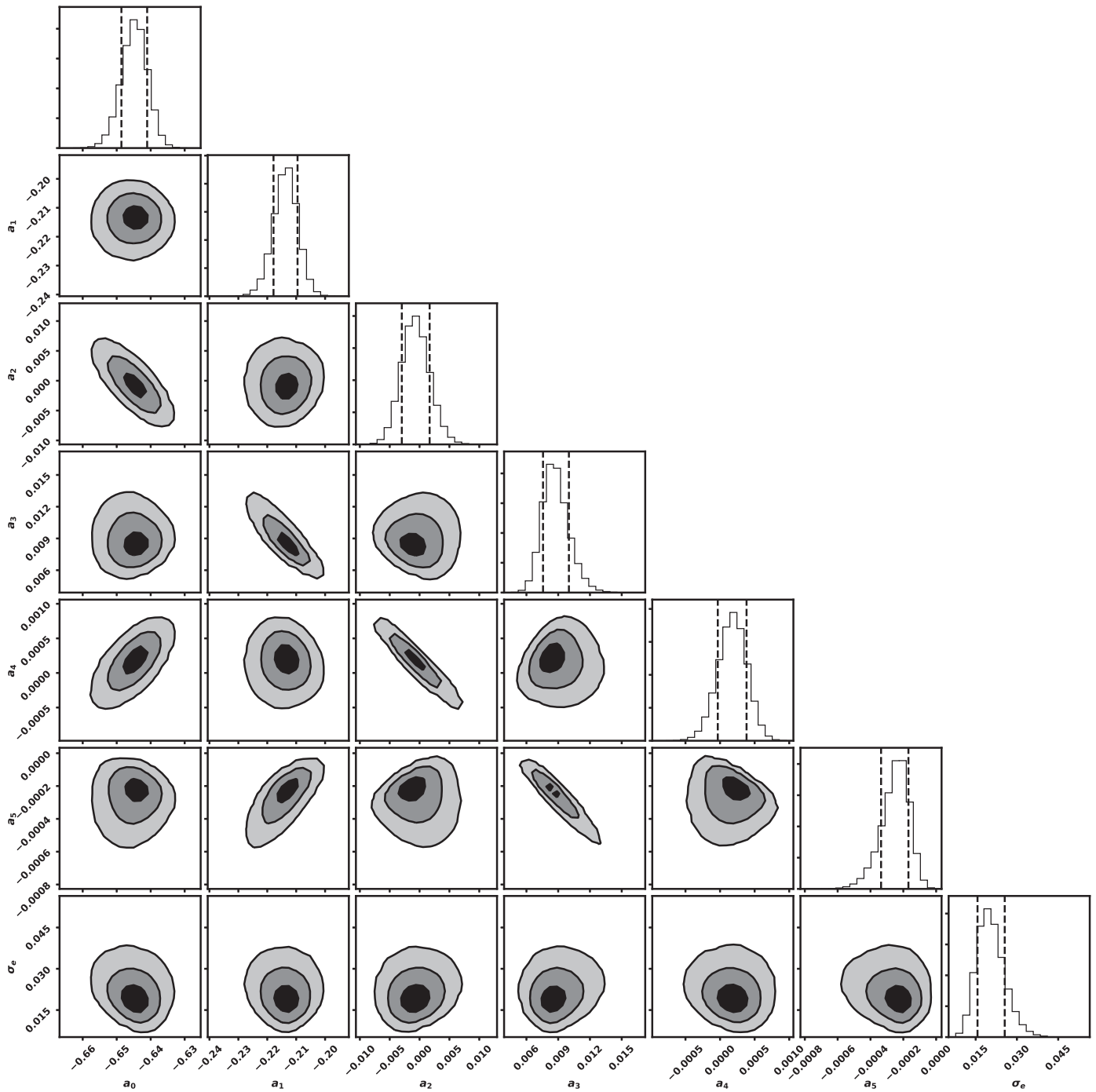
Figure 8. Posterior projections for the a_i values derived from our MCMC fit to Equation (4), as well as the additional error term σ_e. Contours denote the 1σ, 2σ, and 3σ confidence intervals, and the dashed lines in the histogram mark 1σ. The σ_e parameter represents the fractional error in the total mass, added to account for intrinsic variation in the relation or underestimated uncertainties in the input masses. The figure was generated using `corner.py` (Foreman-Mackey 2016).

each fit. We also provided trimmed posteriors for each coefficient and σ_e for our suggested relations.[22] Fits using $n = 4$ and $n = 6$ are included in Table 6 for reference, although we suggest only using the $n = 5$ relation.

To estimate the uncertainty in our M_{K_S}–M_* relation, we computed the standard deviation in the derived masses for a fixed M_{K_S} across all MCMC fits, adding errors from σ_e in quadrature. This accounts for (correlated) uncertainties in the a_i

coefficients in addition to intrinsic scatter in the M_{K_S}–M_* relation as characterized by σ_e. We list uncertainties as a function of M_{K_S} in Table 7. Including all sources of uncertainty, the relation is precise to $\simeq 2\%$ over most of the mass range, exceeding 3% near the edges where there are fewer binaries to constrain the fit.

Since σ_e (intrinsic scatter in the relation) represents the major source of uncertainty over most of the mass range, we also tried to estimate the intrinsic scatter using a more traditional χ^2 approach. For this test, we adopted the best-fit (highest-likelihood)

---

[22] https://github.com/awmann/M_-M_K-/tree/master/resources
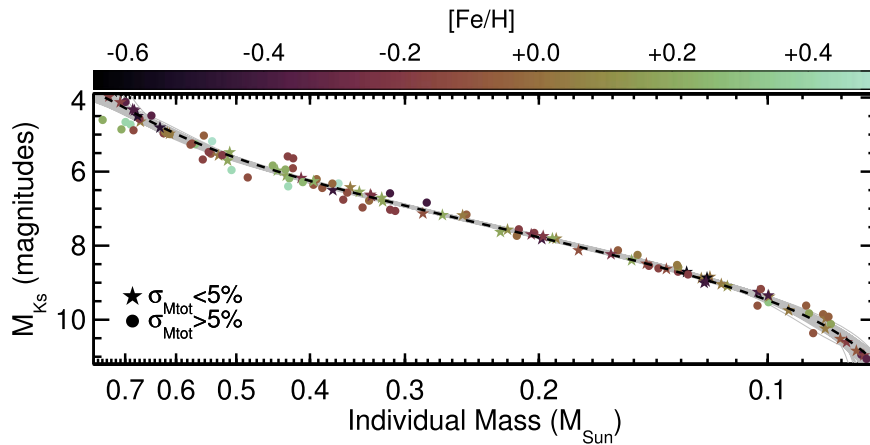
Figure 9. Absolute K_S-band magnitude as a function of mass for targets in our sample. Stars indicate systems with total dynamical mass uncertainty <5%, while those with larger uncertainties are shown as circles. All points are color-coded by their estimated metallicity. The black dashed line indicates the best fit (highest likelihood) from our MCMC analysis. To provide an estimate of the scatter in the relation as a function of mass, we show 100 randomly selected fits from the MCMC chain in gray. Note that our orbit fits only provide $M_{tot,dyn}$; we used the mass ratios derived from the best-fit $M_{K_S}-M_*$ relation here, and this figure should be considered for display purposes only. Figure 10 shows the comparison between $M_{tot,pre}$ (from our $M_{K_S}-M_*$ relation) and $M_{tot,dyn}$ (from Equation (3)), which is more reflective of how the MCMC fit is done.
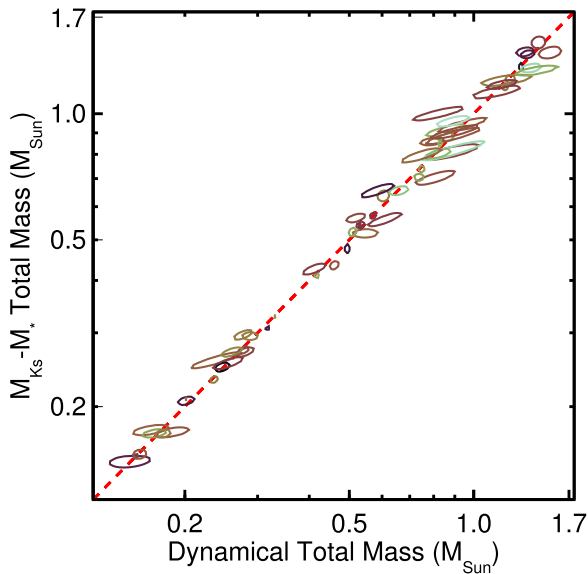
Figure 10. Predicted total (system) mass from the $M_{K_S}-M_*$ relation ($M_{tot,pre}$) as a function of the total dynamical mass determined from the orbital fits ($M_{tot,dyn}$). Ellipses represent $\simeq 1\sigma$ distribution of values for each point, accounting for parallax errors common to both the predicted and dynamical mass. Predicted masses (Y-axis) also account for errors arising from σ_e and correlated uncertainties in the a_i values. Color-coding by [Fe/H] matches that of Figure 9.

Figure 11. Median of the mass posteriors at each M_{K_S} using fits of varying order (n) to Equation (4) compared to the empirical values for the lowest-mass stars in our sample (black points). The inset shows objects with $M < 0.1\,M_\odot$, where the disagreement between different orders is largest. A high order ($n = 5$) is required to reproduce objects below $0.085\,M_\odot$ as the relation becomes increasingly nonlinear. The systematic offset seen between the low-mass sample and the best-fit relation can be seen in the coefficient posteriors and the best-fit relation (i.e., the distribution of fits is systematically high).

coefficient parameters given in Table 6 for $n = 5$. We applied the relation to each of the 124 component stars in our binary sample to compute their predicted individual masses and then summed the masses of each component in a system to obtain total masses ($M_{tot,pre}$) for each of the 62 binary systems. We compared these to the dynamical total masses ($M_{tot,dyn}$), computing a χ_ν^2 value over all 62 systems. Our χ_ν^2 computation accounted for errors in K_S magnitudes, parallaxes, and orbital parameters. The final χ_ν^2 from this comparison was 1.7. Adding a missing error term of 1.6% in the output M_* values from the relation yields $\chi_\nu^2 \simeq 1$, somewhat smaller than our σ_e estimates from the MCMC analysis. The difference arises because the χ^2 method fails to fully account for correlations between M_{K_S} and $M_{tot,dyn}$. Adopting a larger 5%

uncertainty yielded a $\chi_\nu^2 = 0.6$, which has a <0.2% chance of occurring given the number of degrees of freedom. This rules out a significantly larger intrinsic scatter in our fit and confirms that our 2%–3% uncertainties are consistent with the data.

Some systems land >10% outside the relation in Figures 9 and 10; however, all of these targets have similarly large (>10%) uncertainties in $M_{tot,dyn}$. If we restrict our sample to the 47 binaries with uncertainties on $M_{tot,dyn} < 10\%$, the rms for the fit residuals is only 4.3%. Similarly, the rms is 2.6% for the 28 binaries with <5% mass uncertainties and 2.0% for the 13 systems with <2% total mass uncertainties, confirming the 2%–3% precision for the derived $M_{K_S}-M_*$ relation.

While the values in Table 7 can be used to estimate mass uncertainties arising from using our given $M_{K_S}-M_*$ relation, a

Table 6
Best-fit Coefficients for Equations (4) and (5)

n	a_0	a_1	a_2	a_3	a_4	a_5	a_6	f	σ_e	BIC
4	−0.649	−0.202	5.16×10^{-3}	4.91×10^{-3}	-3.54×10^{-4}	⋯	⋯	⋯	0.025	90
5	−0.642	−0.208	-8.43×10^{-4}	7.87×10^{-3}	1.42×10^{-4}	-2.13×10^{-4}	⋯	⋯	0.020	86
6	−0.642	−0.209	-5.11×10^{-3}	7.25×10^{-3}	1.45×10^{-3}	-1.30×10^{-4}	-7.61×10^{-5}	⋯	0.020	89
4	−0.643	−0.199	7.36×10^{-4}	4.45×10^{-3}	-7.69×10^{-5}	⋯	⋯	0.0076	0.026	92
5	−0.647	−0.207	-6.53×10^{-4}	7.13×10^{-3}	1.84×10^{-4}	-1.60×10^{-4}	⋯	−0.0035	0.021	88
6	−0.644	−0.221	-5.51×10^{-3}	1.13×10^{-2}	1.18×10^{-3}	-4.25×10^{-4}	-4.71×10^{-5}	−0.0010	0.020	93

Note. Fits follow the form $\log_{10}\left(\frac{M_*}{M_\odot}\right) = \sum_{i=0}^{n} a_i (M_{K_S} - zp)^i$, where $zp \equiv 7.5$. The $n = 5$ fit is preferred, while the others are listed for reference.

Table 7
Error in M_{K_S}–M_* Relation

M_{K_S} (mag)	M_* $M_\odot$	SpT[a]	σ_{M_*}[b] $M_\odot$	σ_{M_*}[b] %
		No [Fe/H] Term ($f = 0$), Fifth Order		
4.0	0.754	K4.5	0.028	3.7
4.5	0.6739	K7.0	0.016	2.4
5.0	0.6020	M0.0	0.015	2.4
5.5	0.5255	M1.5	0.012	2.3
6.0	0.4440	M2.5	0.0099	2.2
6.5	0.3630	M3.0	0.0081	2.2
7.0	0.2890	M3.5	0.0064	2.2
8.0	0.1776	M4.5	0.0039	2.2
8.5	0.1411	M5.0	0.0032	2.2
9.0	0.1153	M6.0	0.0026	2.3
9.5	0.0977	M6.5	0.0023	2.4
10.0	0.0863	M7.5	0.0022	2.6
10.5	0.0791	M9.0	0.0021	2.6
11.0	0.0742	L1.0	0.0024	3.2
		[Fe/H] Term (f), Fifth Order		
4.0	0.753	K4.5	0.029	3.9
4.5	0.6734	K7.0	0.017	2.5
5.0	0.6017	M0.0	0.015	2.5
5.5	0.5255	M1.5	0.012	2.4
6.0	0.4441	M2.5	0.010	2.3
6.5	0.3630	M3.0	0.0082	2.3
7.0	0.2889	M3.5	0.0065	2.3
8.0	0.1775	M4.5	0.0040	2.3
8.5	0.1411	M5.0	0.0033	2.3
9.0	0.1152	M6.0	0.0027	2.4
9.5	0.0977	M6.5	0.0024	2.5
10.0	0.0863	M7.5	0.0023	2.6
10.5	0.0791	M9.0	0.0021	2.7
11.0	0.0742	L1.0	0.0025	3.3

Notes. This table assumes that M_{K_S} (and [Fe/H]) are known perfectly. Total errors on M_* should take into account errors in the measured parameters and the relation.
[a] Spectral types are given for reference but are extremely rough because of a significant dependence on metallicity and the spectral typing scale. It is not recommended to use this table as a means to compute M_{K_S} or M_* from a spectral type or vice versa.
[b] The uncertainty in the resulting M_* at a given M_{K_S} accounting for intrinsic scatter as characterized by σ_e.

more robust method would be to use the full fit posteriors. This can be important in regions of the fit where the posteriors are asymmetric around the best fit (e.g., between 0.2 and 0.3 $M_\odot$ the best fit sits below the median; see Figure 9). To aid with

using our relation and computing appropriate uncertainties, we included the fit posteriors and a simple code that provides output M_* posteriors given a K_S, distance, and associated uncertainties (see footnote 14). The program combines the scatter in the coefficients (accounting for correlations between a_i values) with the median value of σ_e to produce a realistic M_* posterior including any asymmetry. We note that while the relation is precise to 2%–3%, because of parallax and K_S magnitude uncertainties, the final uncertainties on M_* are usually 3%–4% for stars with *Gaia*-precision distances.

7.3. Testing for Biases in the M_{K_S}–M_* Relation

In Section 7.1 we outlined the methodology and mathematical framework for fitting the M_{K_S}–M_* relation using M_{tot} instead of individual masses. Because the relation is meant to be used on single stars, it is useful to explore what potential biases are introduced when using M_{tot} to fit the M_{K_S}–M_* relation, and especially how it might impact our overall uncertainties.

To this end, we generated a set of synthetic binaries with component (individual) masses assigned according to an input M_{K_S}–M_* relation and tested how well we can recover the assumed relation using only M_{tot} and our framework from Section 7.1. First, we generated a random set of 124 M_{K_S} values matching the overall distribution of our input sample, and then we assigned masses to each system assuming our best-fit M_{K_S}–M_* relation for $n = 5$. We converted this set of synthetic stars into synthetic binaries by splitting the sample and randomly matching a star from one half with one from the other half.

To assign M_{tot} for each system, we summed the assigned masses for each component. We then randomly assigned each system a parallax between 30 and 200 mas (matching our calibration sample), which enabled us to convert the assigned M_{K_S} values for each system to an unresolved K_S and ΔK_S and M_{tot} into α_{ang}^3/P^2 by inverting Equation (3). At this phase, each binary has the required set of information that went into our MCMC framework, specifically K_S, ΔK_S, α_{ang}^3/P^2, and π.

To keep our input errors consistent with our binary calibration sample, we drew uncertainties for each parameter (K_S, ΔK_S, α_{ang}^3/P^2, and π) and system by randomly sampling errors from our observed sample. Errors on α_{ang}^3/P^2 and π were treated as fractional Gaussian uncertainties, while errors on K_S and ΔK_S were taken as Gaussian errors in magnitudes. Synthetic binaries were sometimes assigned a large error in both α_{ang}^3/P^2 and π, yielding total mass uncertainties greater than 20%. Such systems would not have passed our selection criteria (Section 2); hence, in these cases we redrew uncertainties for the system.
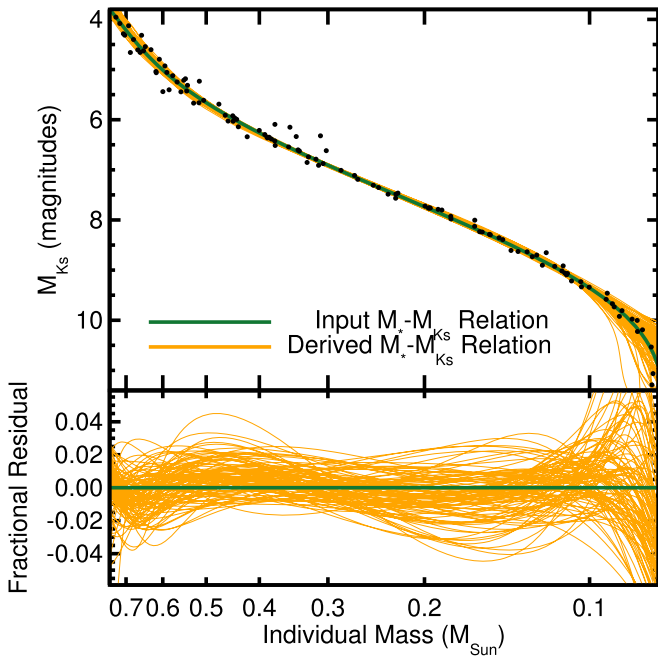
Figure 12. Input M_{K_S}–M_* relation (green) compared to the recovered relations (orange). The recovered M_{K_S}–M_* fits are the result of running our MCMC fit on a set of synthetic binaries using only their total masses, but their individual components follow the input M_{K_S}–M_* relation. The black points are one of the 100 randomly generated sets of synthetic binaries, which are shown for reference (each blue fit will use a different set of synthetic binaries).

All parameters were then randomly perturbed by their assigned uncertainties (assuming Gaussian errors). To replicate the effects of intrinsic scatter, we then perturbed the $\alpha_{\rm ang}^3/P^2$ by 2.0% (median value of σ_e). Note that these perturbations changed the assigned $M_{\rm tot}$ and M_{K_S}; for the purposes of this test we can consider the original values the true $M_{\rm tot}$ and M_{K_S} (they follow the input M_{K_S}–M_* perfectly), while the perturbed values are observed (imperfect measurements with realistic errors).

We ran the 62 synthetic binaries through our MCMC framework, exactly as we did with the real sample (Section 7.1). The only change was that we ran the MCMC chain for only 10,000 steps for computational efficiency. We repeated this process 100 times, each time generating a new binary sample and rerunning our MCMC analysis. After each run, we saved the best-fit a_i values and median σ_e. The shorter chain meant that not all fits passed our requirements for convergence, but we are mostly interested in the best-fit values and not a full exploration of the uncertainties that require a long chain.

We show the resulting distribution of M_{K_S}–M_* relations using our synthetic binary sample alongside the input (true) relation in Figure 12. The fits using the synthetic binaries followed input distribution closely in all cases. The range of solutions deviated from the input by $\simeq \sigma_e$, as expected, with the exception of $< 0.1\,M_\odot$, where there was a wider range of possible solutions. However, the larger scatter is reflected in our MCMC fit to the calibration binaries (Figure 9) and is well described by our adopted uncertainties ($\simeq 3\%$) in the very low mass regime. Since the fits using synthetic binaries used no information about the individual component masses, the consistency between the input and output M_{K_S}–M_* relation in this test confirms that our use of total masses does not significantly bias our result.
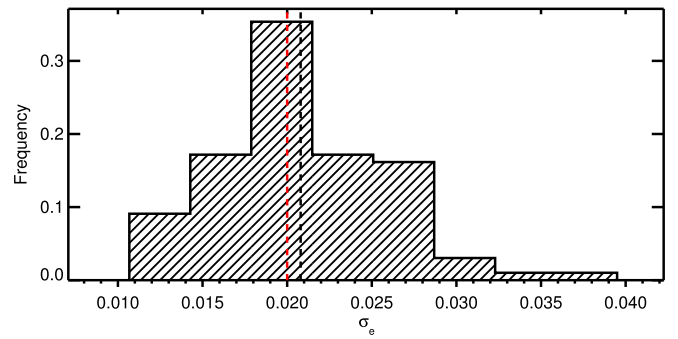
Figure 13. Input σ_e (red dashed line) compared to the distribution of values determined from 100 different sets of synthetic binaries (black histogram). The black dashed line indicates the median of the recovered σ_e values.

We show how well we recovered the input σ_e in Figure 13. The median of recovered σ_e values was slightly higher than our input value, although the two were consistent given the range of possible recovered values. Since σ_e was the dominant source of uncertainty over most of the relation, this confirms that our overall errors are reasonable despite our use of total masses.

The above test assumed that our functional form for the M_{K_S}–M_* (Equation (2)) is perfect. However, the real M_{K_S}–M_* relation is unknown; our assumption was that we could use an exponential to approximate this unknown relation with a smooth relation between α and M_{K_S}. To test the impact of these assumptions, we used the same method of generating synthetic binaries but instead assigned the true masses using a different formula. We then tested how well we could recover the assumed M_{K_S}–M_* using the functional form given in Equation (2).

For this test, we assumed that the M_{K_S}–M_* follows a piecewise function of the form

$$
M_* = \begin{cases} 10^{-0.136*M_{K_S}+0.36} & 3.5 < M_{K_S} \leqslant 5.0 \\ 10^{-0.16*M_{K_S}+0.48} & 5.0 < M_{K_S} \leqslant 8.0 \\ 10^{-0.11*M_{K_S}+0.08} & 8.0 < M_{K_S} \leqslant 11.5, \end{cases}
$$

where M_* is given in solar masses and M_{K_S} in magnitudes. Equation (13) was partially motivated by the form of Henry & McCarthy (1993), adjusted to meet the boundary conditions of our sample. However, we highlight that the goal is not to assign a formula that is accurate, but rather to assign one that is plausible but *different* from the exponential we assumed when fitting the relation. A piecewise equation is useful for this purpose because the breaks due to transitions at $M_{K_S} = 5$ and $M_{K_S} = 8$ might not be obvious when looking at the distribution of *total* masses and are harder to approximate with a polynomial or exponential. A piecewise function is also a useful test of potential astrophysical breaks in the true relation, such as the fully convective boundary. Thus, a piecewise function can be taken as a worst-case but still plausible scenario for the M_{K_S}–M_* relation, hence representing a strong test of our method.

In Figure 14 we show the result of repeating our synthetic binary test using an input M_{K_S}–M_* relation from Equation (13). The transitions between different sections of the piecewise equation are clear in the residuals, where the input and output relations show discontinuities and larger discrepancies. If there is a sharp astrophysical break (e.g., fully versus partially
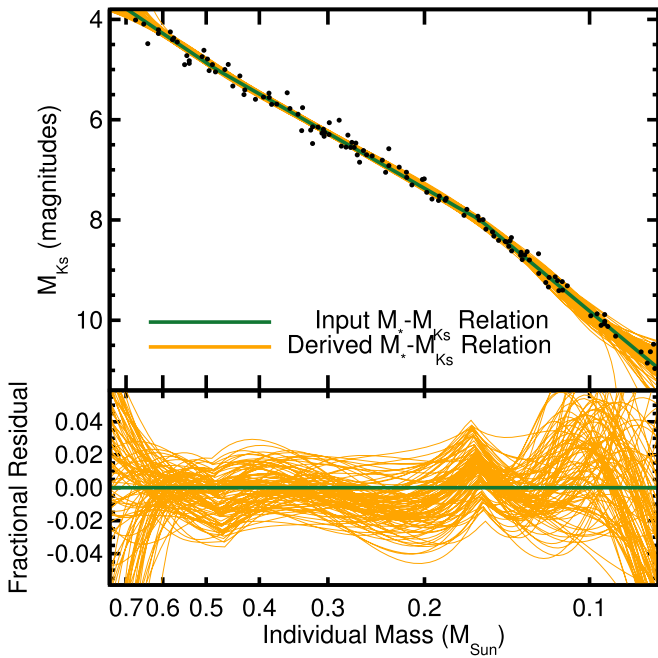
Figure 14. Same as Figure 12, but assuming a piecewise input $M_{K_S}–M_*$ relation (Equation (13)). The fit (orange lines) assumes that the $M_{K_S}–M_*$ follows Equation (2). Note that the black points are a randomly selected set of synthetic binaries and do not necessarily match any values from Figure 13 or the real binary calibration sample.

convective stars), the resulting relation would systematically miss masses right at the transition, but the relation would be unaffected just above or below the break. Further, the divergence is never significantly larger than our uncertainties.

We can adjust the coefficients in Equation (13) to make the breaks sharper. In these cases the deviations between our input and output increase at the breaks (although elsewhere the fit still follows the input relation). However, in these cases our derived value of σ_e increases proportionately. Even if we assume physically unrealistic breaks, our final uncertainties would still capture these deviations. Thus, all tests confirm that our output relation and assigned uncertainties are reasonable and the use of total, instead of individual, masses has no significant impact.

7.4. Testing the Relation on Individual Dynamical Masses

Our tests with synthetic binaries in Section 7.3 confirm that our use of total masses and our assumed function form for the $M_{K_S}–M_*$ relation have no significant impact on our relation. However, it is still useful to perform a completely independent test of our $M_{K_S}–M_*$ relation using dynamically measured individual masses. Further, a comparison between our relation and literature mass determinations would be useful to confirm or refute our assigned uncertainties and may reveal the origin of σ_e. To this end, we utilized two samples of binaries with precisely determined *individual* masses from the literature, each of which is completely independent of our calibration sample: (1) astrometric binaries or triples with radial velocities or absolute astrometry not included in our binary sample, and (2) M dwarf—M dwarf eclipsing binaries.

We drew sample 1 from Henry & McCarthy (1993), Delfosse et al. (2000), and Benedict et al. (2016), excluding those in our calibration sample (Section 2). We added one

target, GJ 2005A, for which the BC pair was analyzed in this paper, but Seifahrt et al. (2008) provide a mass determination for the A component. For sample 2, we drew eclipsing binaries from the compilations of Hartman et al. (2011) and Parsons et al. (2018), restricting the sample to double-lined eclipsing binaries, those with individual mass estimates better than 5%, and systems with a parallax from the second *Gaia* data release passing the *Gaia* quality cuts given in Appendix C of Lindegren et al. (2018). We removed 19e-3-08413AB because the distance is too large ($\gg$500 pc) to assume zero reddening and excluded systems from Kraus et al. (2011) because they have no reported flux or luminosity ratios, which are needed to estimate ΔK_S (detailed below). Lastly, we removed PTFEB132 +19AB (Kraus et al. 2017) because it is young ($\simeq$650 Myr). In total this gives us individual masses for 29 stars with which to test our $M_{K_S}–M_*$ relation.

A significant advantage of eclipsing binaries is that we could adopt the much more precise parallaxes from *Gaia*, as they all have orbits that are too tight to show detectable centroid motion. For the astrometric binaries/triples, we drew parallaxes either from *Gaia* DR2 parallaxes of nearby companions (e.g., for Gl 644ABC we used the *Gaia* parallax from the wider companion Gl 643) or from sources that accounted for the high-order nature of the system.

As with binaries analyzed in this paper, unresolved K_S values were taken from 2MASS. We used AO data from VLT/NaCo to derive ΔK for Gl 866AC-B and our own Keck/NIRC2 measurements for Gl 644A-BC and GJ 2005A-B-C (all three are resolved), just as was done for binaries analyzed in this paper. For other systems, including unresolved components of the triples (Gl 866A-C and Gl 644B-C), the literature only provided contrast ratios in optical bands. We converted these to ΔK_S using the synthetic and observed magnitudes given in Mann et al. (2015), following a procedure analogous to that outlined in Kraus et al. (2017). To briefly summarize, we found the combination of two single-star spectral templates that reproduced both the unresolved spectral energy distribution (*Gaia* and 2MASS photometry) and the measured contrast(s) from the literature reference (usually V, R, or *Kepler*) and then computed a ΔK_S value for the best-fit template combination. This is similar to our conversion of ΔK_X to ΔK_S detailed in Appendix A.

Correction from optical to NIR contrasts depends on metallicity (e.g., Schlaufman & Laughlin 2010), and precise metallicities of these systems were not known. Instead, we assumed that all systems were $-0.6 < [Fe/H] < +0.4$, and we adopted uncertainties that encompass the range of values due to unknown metallicity. Errors introduced from these contrast conversions were extremely small for nearly equal mass systems (because $\Delta K_S \simeq 0$) but became large (>0.1 mag) for systems with mass ratios $\lesssim 0.6$.

Table 8 lists all systems with their adopted parallaxes, M_* estimates, corresponding references, and our derived K_S magnitudes.

We show the M_{K_S} values versus literature dynamical masses for these systems in Figure 15 compared to the prediction from our $M_{K_S}–M_*$ relation. Our result follows the literature individual masses extremely well. To quantify this and test our previously estimated precision on the $M_{K_S}–M_*$, we calculated a predicted mass for each star using the $n = 5$ relation as given in Section 7.2 and the M_{K_S} value from our adopted K_S magnitudes and parallaxes. This is exactly as the

Table 8
Targets with Individual Masses

Name	M_* ($M_\odot$)	K_S (mag)	π (mas)	Type[a]	M_* Ref	π Ref
HAT-TR-318-007A	0.448 ± 0.011	11.509 ± 0.041	8.345 ± 0.076	EB	1	2
HAT-TR-318-007B	0.2721 ± 0.0042	12.459 ± 0.062	8.345 ± 0.076	EB	1	2
NGTS J0522-2507A	0.1739 ± 0.0015	11.798 ± 0.055	18.378 ± 0.072	EB	3	2
NGTS J0522-2507B	0.1742 ± 0.0019	11.798 ± 0.056	18.378 ± 0.072	EB	3	2
HATS 551-027A	0.2440 ± 0.0030	10.401 ± 0.071	25.484 ± 0.061	EB	4	2
HATS 551-027B	0.1790 ± 0.0015	10.852 ± 0.080	25.484 ± 0.061	EB	4	2
1RXSJ1547+4508A	0.2576 ± 0.0085	8.967 ± 0.023	45.120 ± 0.035	EB	5	2
1RXSJ1547+4508B	0.2585 ± 0.0080	8.967 ± 0.026	45.120 ± 0.035	EB	5	2
Kepler-16A	0.6897 ± 0.0035	9.060 ± 0.042	13.289 ± 0.027	EB	6	2
Kepler-16B	0.20255 ± 0.00066	12.11 ± 0.23	13.289 ± 0.027	EB	6	2
LSPM J1112+7626A	0.3946 ± 0.0023	10.180 ± 0.060	17.616 ± 0.051	EB	7	2
LSPM J1112+7626B	0.2745 ± 0.0012	10.910 ± 0.090	17.616 ± 0.051	EB	7	2
NSVS 01031772A	0.5428 ± 0.0027	9.420 ± 0.050	16.480 ± 0.030	EB	8	2
NSVS 01031772B	0.4982 ± 0.0025	9.650 ± 0.060	16.480 ± 0.030	EB	8	2
YY GemA	0.5992 ± 0.0047	5.960 ± 0.045	66.232 ± 0.051	EB	9	2
YY GemB	0.5992 ± 0.0047	6.010 ± 0.051	66.232 ± 0.051	EB	9	2
LSPM J0337 + 6910A	0.375 ± 0.016	9.470 ± 0.071	26.907 ± 0.041	EB	10	2
LSPM J0337 + 6910B	0.280 ± 0.015	10.048 ± 0.093	26.907 ± 0.041	EB	10	2
GU BooA	0.6160 ± 0.0070	10.911 ± 0.046	6.147 ± 0.016	EB	11	2
GU BooB	0.6000 ± 0.0060	11.041 ± 0.061	6.147 ± 0.016	EB	11	2
GJ 2069A	0.42940 ± 0.00100	7.230 ± 0.041	60.138 ± 0.092	EB	12	2
GJ 2069C	0.3950 ± 0.0018	7.490 ± 0.054	60.138 ± 0.092	EB	12	2
GJ 2005A	0.115 ± 0.010	8.714 ± 0.060	128.5 ± 1.5	Astr	13	14
Gl 866B	0.1145 ± 0.0012	6.593 ± 0.041	293.60 ± 0.90	Astr	15	15
Gl 866A	0.1187 ± 0.0011	6.557 ± 0.072	293.60 ± 0.90	Astr	15	15
Gl 866C	0.09300 ± 0.00080	7.127 ± 0.080	293.60 ± 0.90	Astr	15	15
Gl 644A	0.4155 ± 0.0057	5.350 ± 0.041	153.92 ± 0.13	Astr	15	2[b]
Gl 644B	0.3466 ± 0.0047	5.610 ± 0.071	153.92 ± 0.13	Astr	15	2[b]
Gl 644C	0.3143 ± 0.0040	5.890 ± 0.092	153.92 ± 0.13	Astr	15	2[b]

Notes.
[a] Eclipsing (EB) or astrometric (Astr) binary/triple.
[b] Parallax from companion star Gl 643.

References. (1) Hartman et al. 2018; (2) Lindegren et al. 2018; (3) Casewell et al. 2018; (4) Zhou et al. 2015; (5) Hartman et al. 2011; (6) Doyle et al. 2011; (7) Irwin et al. 2011; (8) Lopez-Morales et al. 2006; (9) Torres & Ribas 2002; (10) Irwin et al. 2009; (11) López-Morales & Ribas 2005; (12) Wilson et al. 2017; (13) Seifahrt et al. 2008; (14) Benedict et al. 2016; (15) Ségransan et al. 2000.

procedure would be applied to single stars in the field. The output masses account for uncertainty in the relation (including intrinsic scatter characterized by σ_e) and uncertainties in K_S magnitudes and measured parallaxes.

Of the 29 stars, only one had a literature mass $>2\sigma$ off from the M_{K_S}–M_* predicted value (Kepler-16A), and the χ_ν^2 of predicted and dynamical masses was 1.02 ($\chi^2 = 29.6$). The rms of the residuals was 3.6%, although this is driven primarily by the points with the largest errors in M_* or K_S. If we restrict the sample to targets with 3% uncertainties in M_*, the rms is only 2.8%, in agreement with our estimated uncertainties in the M_{K_S}–M_* relation.

Figure 15 also suggests a small ($\simeq 2\%$) systematic offset, such that literature dynamical masses for eclipsing binaries are preferentially higher than those predicted from the M_{K_S}–M_* relation. This difference is comparable in size to σ_e and our overall precision and hence is within systematic uncertainties (further verified by a χ_ν^2 near unity). Assuming that the offset is astrophysical, it is consistent with a scenario where low-mass eclipsing binaries are inflated compared to single stars owing to increased activity (e.g., MacDonald & Mullan 2012; Feiden & Chaboyer 2013, 2014a; Somers & Stassun 2017). Higher activity levels may inhibit convection, increasing the radius and
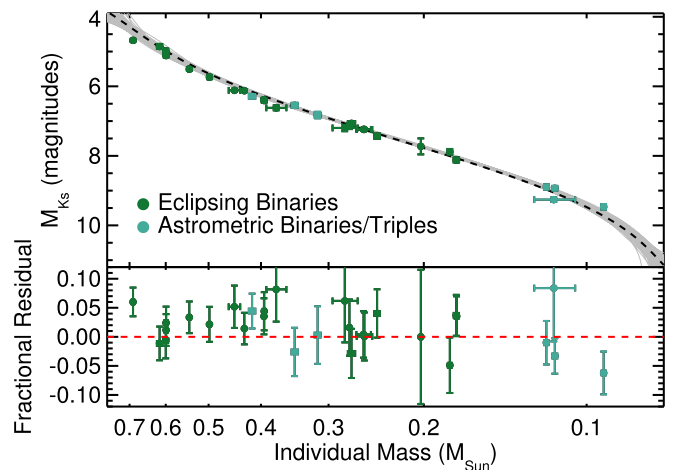
Figure 15. Top: M_* and M_{K_S} for M dwarfs with individual dynamical masses from the literature (points) compared to our derived M_{K_S}–M_* relation (dashed line). The gray region shows 100 randomly selected fits from the MCMC. Bottom: fractional difference between the empirical mass and the mass predicted by our M_{K_S}–M_* relation. Points are color-coded by type (eclipsing or astrometric binaries). Errors in the bottom panel account for uncertainty in the M_{K_S}–M_* relation and measurement uncertainties in K_S magnitudes, parallaxes, and the literature dynamical masses.
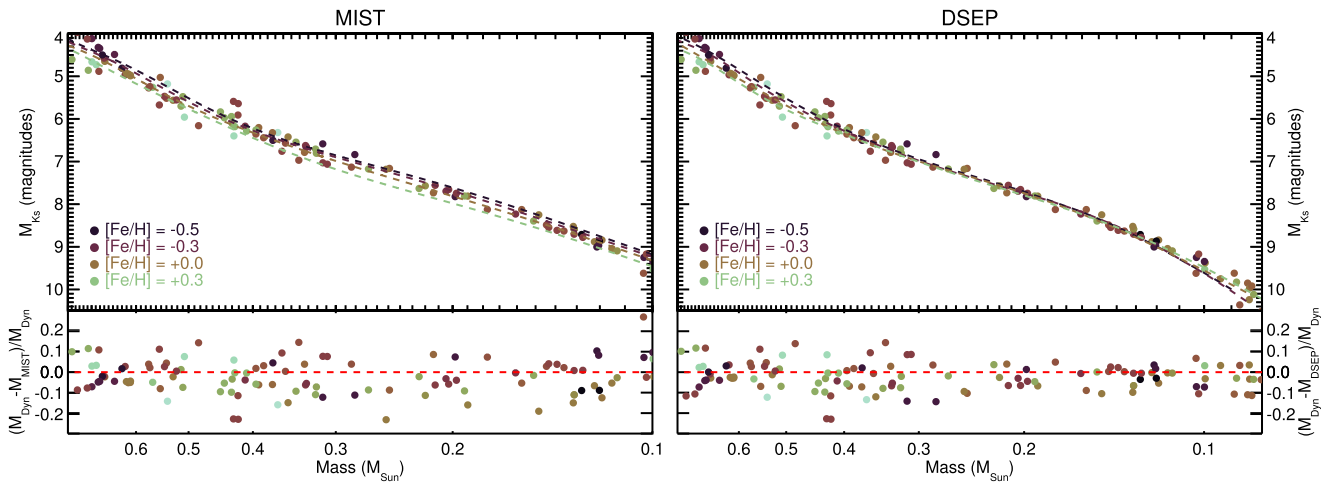
Figure 16. M_{K_S} as a function of M_* using MIST (left) and DSEP (right) tracks of different metallicities (dashed lines) compared to empirical mass determinations (points). Color-coding by metallicity is the same for the points and lines and matches the color scale of Figure 9. Due to the limits of the model grids, the plots cut at 0.1 and 0.085 $M_{\odot}$ for MIST and DSEP, respectively. The bottom panel shows the fractional residual between the model and empirical determinations. The model masses for the residuals were estimated by interpolating over the model grid using the [Fe/H] and M_{K_S} for a given target. As with Figure 9, we have converted our dynamical total masses to individual masses using the predicted mass ratios from the $M_{K_S}-M_*$ for display purposes.

decreasing the fusion rate and hence overall luminosity at fixed mass. For activity levels expected in most low-mass EBs, Feiden (2016) models suggest a difference of 1%–3% in M_* for a fixed M_{K_S} over $0.1\,M_{\odot} < M_* < 0.6\,M_{\odot}$, consistent with the offset seen here.

7.5. The Role of Metallicity

We explored the effects of [Fe/H] on the $M_{K_S}-M_*$ relation using the Mesa Isochrones and Stellar Tracks (MIST; Choi et al. 2016; Dotter 2016) and an updated version of the Dartmouth Stellar Evolution Database (DSEP; Dotter et al. 2008). The updates to DSEP have been previously detailed in Feiden & Chaboyer (2013, 2014a) and Muirhead et al. (2014), with additional information on the updates for low-mass stars in Mann et al. (2015). MIST models use ATLAS/SYNTHE model atmospheres (Castelli & Kurucz 2004) with updated TiO opacities for late-type stars that should improve performance. DSEP uses PHOENIX (Hauschildt et al. 1999a, 1999b) models, which have been used widely for studies of late-type dwarfs (e.g., Boyajian et al. 2012; Bell et al. 2015; Kesseli et al. 2018b). While other model grids (e.g., YaPSI, PARSEC, Lyon; Spada et al. 2013; Chen et al. 2014; Baraffe et al. 2015) show similar agreement with empirical studies of low-mass stars, we leave a more detailed comparison between the full range of model grids and our empirical masses for future analysis, and we restrict our model comparison here to just effects from metallicity.

We show the expected M_{K_S} tracks from MIST and DSEP for $-0.5 < [Fe/H] < +0.3$ in Figure 16 alongside our empirical determinations. MIST models do not extend below $0.1\,M_{\odot}$, while DSEP goes down to $0.085\,M_{\odot}$. For this comparison we assumed a fixed age of 5 Gyr, although the choice of age from 1 to 10 Gyr makes a negligible difference for the mass range shown (Figure 1).

Metal-rich stars are expected to be less luminous for a fixed M_*, whereas the opposite trend is seen for a fixed $T_{\rm eff}$ and most color selections. Higher metal abundance increases the opacity, causing the stellar radius to increase at a fixed M_* and surface temperature to decrease. Decreasing surface temperature also

decreases the core temperature because it shifts the star to a different adiabat, which reduces nuclear reaction rates and overall luminosity. The trend is weaker (or even reversed) in the K band, because although the overall luminosity is lower at higher [Fe/H], most of the increases in opacity are in the optical, causing a larger fraction of the total luminosity to escape at NIR wavelengths. This difference as a function of wavelength can be seen in Figure 6, where the metal-rich spectrum sits below the solar-metallicity one at optical wavelengths but above it in the NIR. The MIST and DSEP models likely have some difference in their treatment of one or both of these competing effects, as the DSEP models show a reduced impact of [Fe/H] on the $M_{K_S}-M_*$ relation as with decreasing stellar mass (likely because of increasing opacity in the optical with decreasing surface temperature), while MIST models show a similarly large impact over the full mass range considered here.

Based on our dynamical masses, there is a slight trend for metal-rich stars above $0.4\,M_{\odot}$ to land below the median sequence, as expected from both model grids. However, many metal-poor stars also land below the sequence, and there is no obvious trend below $0.4\,M_{\odot}$. Further, the largest metal-rich outlier in the high-mass region (Gl 99) had a relatively poor mass determination (12%) and is consistent with the solar-metallicity sequence.

The residuals from our best fit indicate a weak (or no) effect on the derived M_* due to changes in [Fe/H], as we show in Figure 17. A Spearman's rank test yielded no significant correlation between the residuals and [Fe/H]. We tried resampling the measurements using their uncertainties, and <1% of samples showed a significant correlation. We also repeated this test, but restricted to just the best-characterized systems (<5% precision on mass), and still found no significant trend with [Fe/H].

Our sample is limited in its [Fe/H] range; 67% of the targets are $-0.2 < [Fe/H] < +0.2$, and only one target has $[Fe/H] < -0.5$. It is possible that our best-fit relation masked any [Fe/H] term by shifting the fit to match the typical metallicity of stars at a given M_{K_S}. We explored [Fe/H] effects in a more
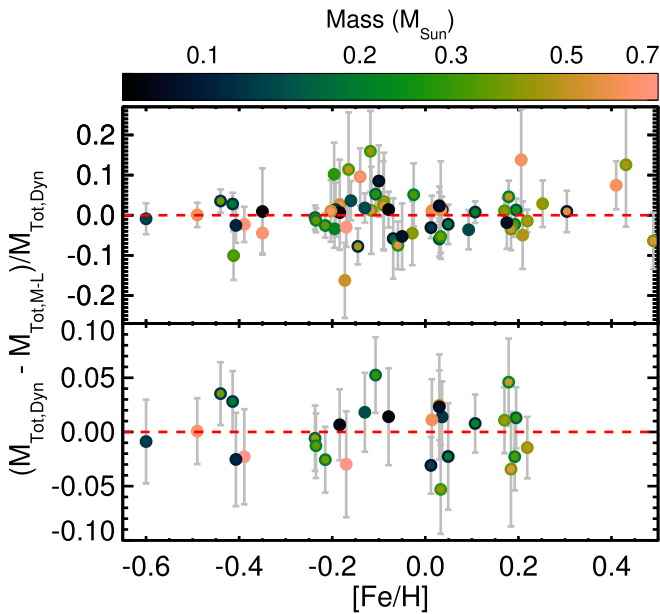
Figure 17. Fractional difference between the orbital and predicted total mass as a function of the system metallicity. The top panel contains all systems, while the bottom panel shows just those with $<5\%$ uncertainties on $M_{\rm tot,dyn}$. Note that the top and bottom panels have different Y-axis ranges. Points are color-coded by the masses of components, with the inner dot corresponding to the primary star's estimated mass and the outer circle to the companion's estimated mass. Error bars include errors on $M_{\rm tot,dyn}$ and $M_{\rm tot,pre}$ (including σ_e).

robust way by fitting for a term of the form

$$M_{\rm tot,pre} = (1 + f\,[{\rm Fe/H}])$$
$$\times \left(10^{\sum_{i=0}^{n} a_i (M_{K_S,2} - zp)^i} + 10^{\sum_{i=0}^{n} a_i (M_{K_S,1} - zp)^i} \right). \quad (5)$$

This is identical to Equation (4) multiplied by $(1 + f{\rm Fe/H}])$. This assumes that a linear change in [Fe/H] corresponds to a fractional change in M_* (e.g., $f = 0.1$ would correspond to a 10% change in derived M_* per dex change in [Fe/H] at a fixed M_{K_S}). This is generally consistent with the models over the metallicity range considered here (although it is predicted to become increasingly nonlinear for [FeH] < -0.5). Equation (5) also assumes a single f over the whole mass range considered. While this is consistent with the predictions of MIST models, DSEP models show a tightening with decreasing mass (increasing M_{K_S}). However, our sample is too small and errors on [Fe/H] are too large to justify adding a term that depends on both [Fe/H] and M_{K_S}. We leave higher-order tests for a future investigation with a broader range of metallicities.

For the metallicity analysis, we excluded the two L dwarfs from the sample because their metallicities are less reliable (extrapolated from an M dwarf calibration). As with our fit to Equation (4), we tested a range of values for n (number of a_i coefficients). Both targets also have masses below the limits of the model grids. Our MCMC fitting method was otherwise identical to that outlined in Section 7.

We show the output coefficient posteriors including f in Figure 18. We list the corresponding best-fit coefficients in Table 6 along with the median values of σ_e and f. As with our fits neglecting any [Fe/H] terms, we found significantly better agreement with the lowest-mass objects in the sample using

$n = 5$, although $n = 4$ and $n = 6$ are listed in Table 6 for reference.

In agreement with our previous analyses, our derived f value is consistent with zero (a $0.0\% \pm 2.2\%$ change in mass per dex change in [Fe/H]). This suggests that our relation will work reasonably well even on more extreme metallicity samples. However, it is also possible that [Fe/H] is less important than abundances of elements that specifically impact the strength of molecular features in M dwarf spectra. Higher C/O, for example, suppresses available oxygen for TiO formation, weakening a major source of opacity in the optical (e.g., C, O, Ti, Fortney 2012; Gaidos 2015; Veyette et al. 2016). This also might explain some of the extra scatter in the relation (σ_e) if there is sufficient variance of these abundances in the given sample. Testing this will require a means to determine more detailed abundances of M dwarfs (e.g., Veyette et al. 2017) and/or to add in subdwarf binaries or other systems with more extreme abundances to provide increased leverage on any metallicity effects.

To compare to the models, we fit the MIST and DSEP grid points in the same manner as the empirical data set following Equation (5). Our binary sample is not uniformly spaced in [Fe/H] and M_{K_S}, so to ensure a fair comparison, we resample the model grid to match the binary sample. For every target, we generated a model-predicted mass at fixed age (5 Gyr) and alpha abundance (solar) by linearly interpolating over M_{K_S} and [Fe/H] (using the assigned values for that target). We used the resulting (model-based) masses with the input M_{K_S} and [Fe/H] values to fit for a model f value that can be compared to our empirical determination.

In Figure 19, we show the posterior on f from the model grids compared to that from the dynamical masses. MIST models predict a larger [Fe/H] effect than suggested by our binary sample, while DSEP predictions are quite consistent with our own. The difference between the two posteriors ($f_{\rm model} - f_{\rm dynamical}$) is inconsistent with zero at 5.1σ for MIST, while for DSEP the difference is 2σ.

The discrepancy between MIST model masses and dynamical masses cannot be explained by σ_e. Scatter from σ_e only amounts to a $\simeq 2\%$ variation in M_* for a given M_{K_S}. The MIST models predict a metallicity effect of $\simeq 17\%$ per dex; since our sample covers about 1 dex in [Fe/H], this translates to an expected $\simeq 17\%$ variation in mass over the full sample, or 8% if we just consider the majority of the targets. It is possible that σ_e is being driven in part by erroneous assigned [Fe/H] (or underestimated errors on [Fe/H]), which would systematically decrease our derived f value, but the effect is too small to reconcile with the MIST models.

The discrepancy between MIST and empirical estimates of the impact of [Fe/H] could be due to missing opacity/ molecular lines in the atmospheric models. Recent comparison suggests that atmospheric models reproduce optical and NIR spectra of M dwarfs to $\simeq 5\%$ (e.g., Lépine et al. 2013; Mann et al. 2013b), with the exception of a few molecular features like CaOH, AlH, and NaH (Rajpurohit et al. 2013). However, these tests have not been performed on the atmospheric models used for MIST isochrones. Missing opacity at optical wavelengths would strengthen the effect of [Fe/H] by underestimating the number of saturated features; if a line is saturated, adding [Fe/H] cannot make it stronger, which serves to reduce the impact of [Fe/H]. The effect at NIR wavelengths would be weaker, since there are fewer molecular bands, but underestimated opacity in the optical shifts continuum levels in the NIR (and how those levels change with [Fe/H]). A problem
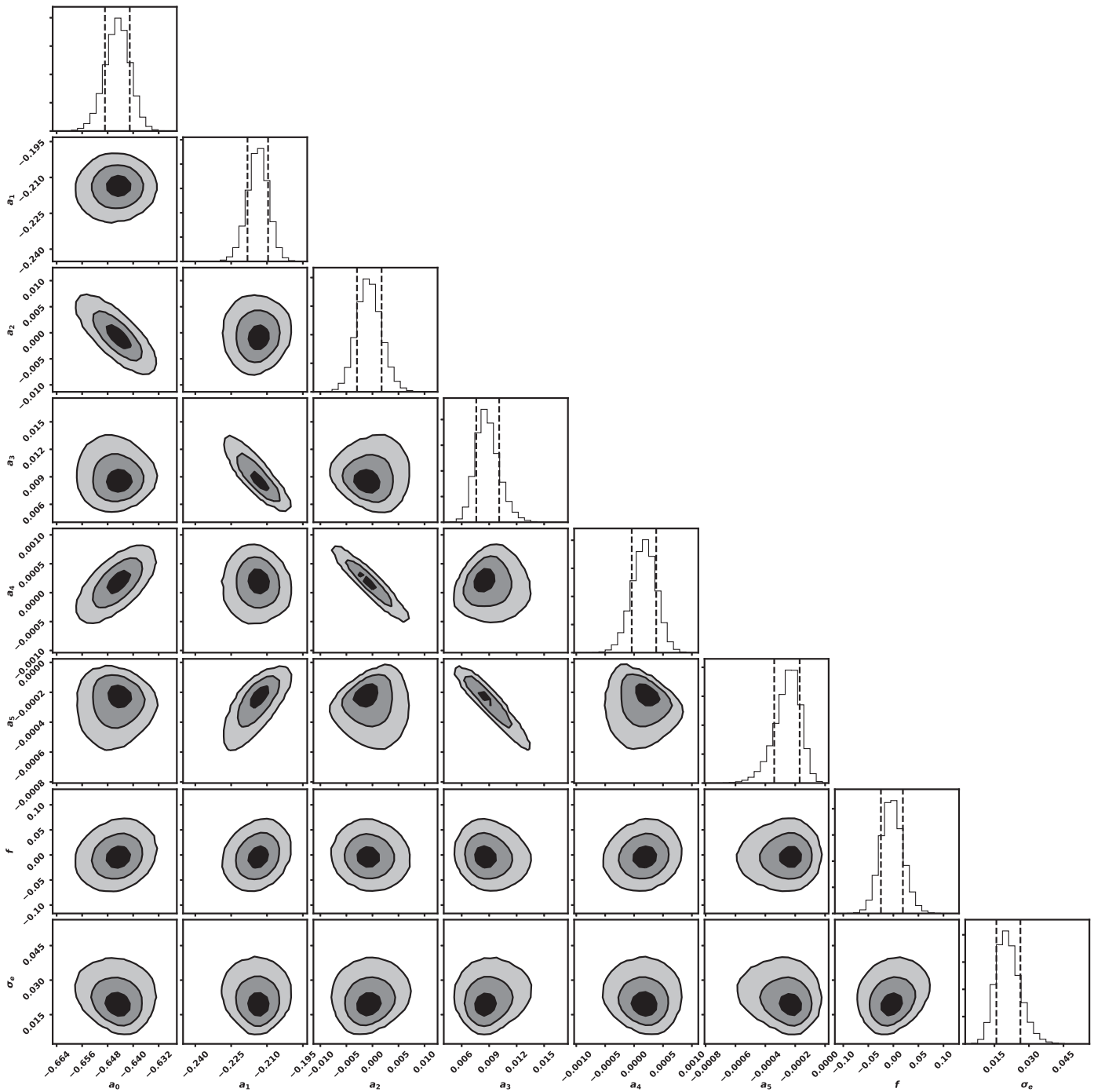
Figure 18. Same as Figure 8, but for the fit following Equation (5), i.e., including the [Fe/H] term, f.

with the input opacities is also consistent with the trend of growing discrepancy at the lowest masses, where molecular bands become increasingly important, and might explain the difference between MIST and DSEP model predictions.

7.6. Comparison to Previous Relations

7.6.1. Henry & McCarthy (1993)

Henry & McCarthy (1993) provided one of the first M_K–M_* relations, providing the basis for updates from Delfosse et al. (2000) and Benedict et al. (2016). Although the least precise

(scatter of 15%–20% in mass), it covers a large range in mass ($0.08\,M_\odot \lesssim M_* \lesssim 1\,M_\odot$). Most of the dynamical mass measurements used for the Henry & McCarthy (1993) relation have since been significantly improved, including many of the astrometric binaries in our sample, but a comparison could reveal any potential changes in results that relied on Henry & McCarthy (1993) with our more precise relation.

We show the comparison in Figure 20. The Henry & McCarthy (1993) relation is split into three sections by mass, as can be seen in the sharp change at $\simeq 0.2$ and $0.5\,M_\odot$. The scatter in masses from Henry & McCarthy (1993) is large; however,
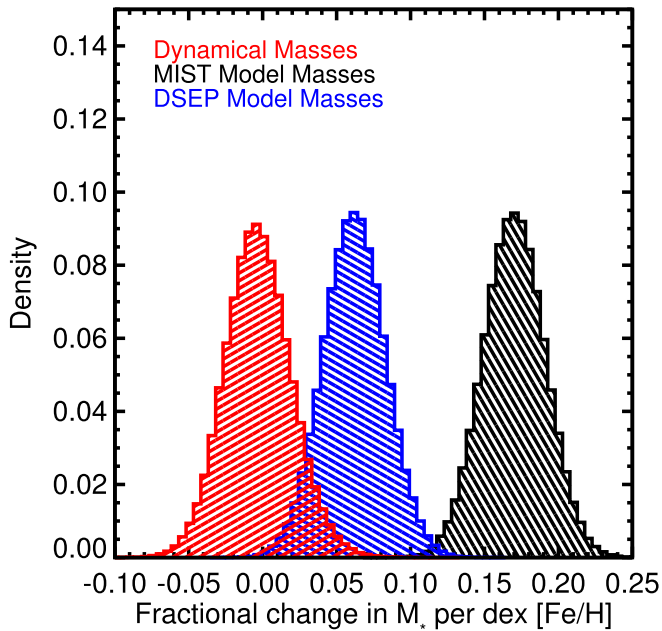
Figure 19. Comparison of the posterior on *f* (fractional change in M_* per dex in metallicity for a fixed M_{K_S}; Equation (5)) predicted by the MIST models (black) and DSEP (blue) with that using our dynamical masses (red). The MIST models significantly overpredict the role of [Fe/H] on the relation, although our results are consistent with predictions from DSEP (at 2σ). There are an identical number of points in each posterior, and the bin sizes are the same.

the two relations track each other to within 10%–20% over the entire overlapping mass range, consistent with the 15%–20% uncertainties given by Henry & McCarthy (1993).

7.6.2. Delfosse et al. (2000)

Delfosse et al. (2000) provided one of the most commonly used M_K–M_* relations, covering $0.1\,M_\odot < M_* < 0.6\,M_\odot$. Like our work, the calibration was built primarily on astrometric binaries. Delfosse et al. (2000) used a mix of individual (targets with radial velocities and/or absolute astrometry) and total masses, with the latter case converted to individual masses using models available at the time. Nearly all the targets in Delfosse et al. (2000) were included in our sample, with the exception of triple stars and eclipsing binaries, both of which were not included in our calibration sample (but were used for tests in Section 7.4). Because of the sample overlap, consistency is expected. However, as with our comparison to Henry & McCarthy (1993), a comparison can be useful to see how past use of Delfosse et al. (2000) may change with our more precise results.

We show the comparison in Figure 21, including the points used in the Delfosse et al. (2000) calibration, as well as the two fit lines. Given errors often quoted for the Delfosse et al. (2000) relation (5%–10%), the two fits are in remarkable (<5%) agreement over most of the mass range ($0.15\,M_\odot \lesssim M_* \lesssim 0.5\,M_\odot$). Only at the high-mass end do the two relations diverge by as much as 10%, but Delfosse et al. (2000) had few calibrators in this regime. While the two relations are in excellent agreement, the relation presented here is a factor of 3–5 more precise over the whole mass regime.

7.6.3. Mann et al. (2015)

Mann et al. (2015) built a catalog of 183 M dwarfs with precise $T_{\rm eff}$ and R_*, calibrated against radius measurements
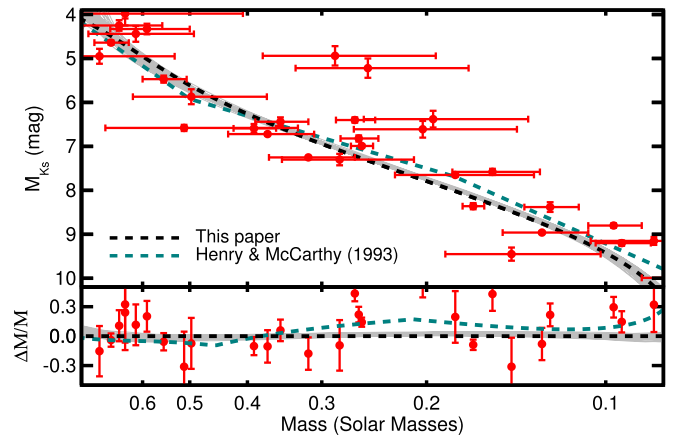
Figure 20. Absolute K_S-band magnitude as a function of mass for astrometric binaries analyzed by Henry & McCarthy (1993; red circles). The relation from Henry & McCarthy (1993) is shown as a teal dashed line (converted from M_K to M_{K_S}), while the best-fit relation from this paper is shown as a blacked dashed line (with error in gray as in Figure 9). The bottom panel shows the residual of the Henry & McCarthy (1993) points compared to our relation. Note that some extreme outlier masses are not shown in the residual plot.
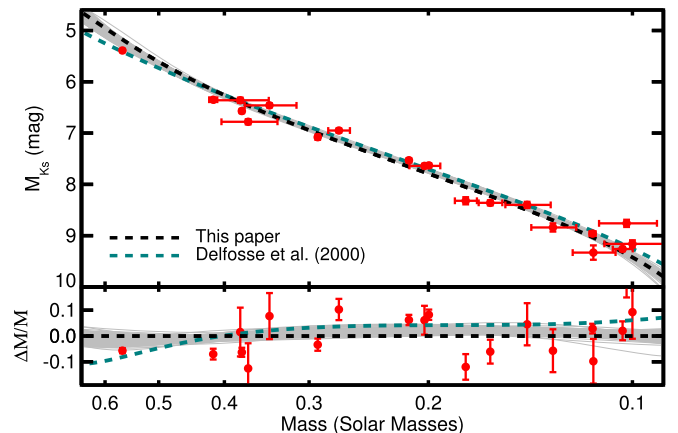
Figure 21. Absolute K_S-band magnitude as a function of mass for astrometric binaries analyzed by Delfosse et al. (2000; red circles). The resulting M_*–M_{K_S} relation from Delfosse et al. (2000) is shown as a teal dashed line, while the best-fit relation from this paper is shown as a blacked dashed line (with error in gray as in Figure 9). The bottom panel shows the residual of the Delfosse et al. (2000) points compared to our relation.

from long-baseline optical interferometry (Boyajian et al. 2012) and precision bolometric fluxes (e.g., Boyajian et al. 2015; Mann & von Braun 2015). Masses were computed for these stars by interpolating the parameters onto an updated version of the DSEP models as described in Feiden & Chaboyer (2013, 2014b) and Muirhead et al. (2014). Although these masses were model dependent, they accurately reproduced the mass–radius relation from low-mass eclipsing binaries. This suggested that the model-based masses were accurate to $\simeq$3% or better and motivated the development of an M_{K_S}–M_* relation from the Mann et al. (2015) sample. A comparison to our relation can be seen in part as a test on the updated DSEP models, in addition to the results given in Mann et al. (2015).

We show our fit with uncertainties alongside that of Mann et al. (2015) in Figure 22. The two fits track each other extremely well, with a maximum divergence of $\simeq$5%. Given the quoted 2%–3% uncertainties from Mann et al. (2015) and similar errors in our relation, this difference is not significant.
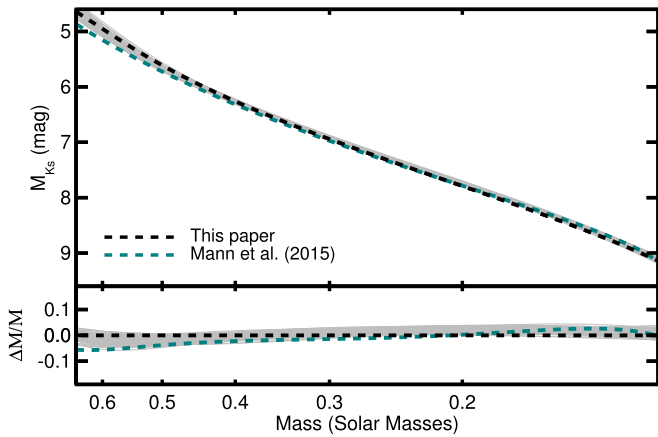
Figure 22. Comparison of $M_* - M_{K_S}$ from Mann et al. (2015), shown as a teal dashed line, to that from this paper, which is shown in black, with 100 randomly selected realizations of the MCMC (as with Figures 9 and 21). Residual is shown in the bottom panel. Individual points from Mann et al. (2015) on which the calibration is based are not shown (for clarity), but they follow a tight sequence around the teal line. Only the range of masses covered by Mann et al. (2015) is shown.

There is a hint of tension above $0.6\,M_\odot$ and around 0.2–$0.3\,M_\odot$, where the difference is the largest, but the offset never exceeds the quoted uncertainties of the two relations.

7.6.4. Benedict et al. (2016)

Like our work, the Benedict et al. (2016) relation was also based primarily on masses derived from M dwarf astrometric binaries. The Benedict et al. (2016) sample uses absolute astrometry from *HST* fine guidance sensors and radial velocities for a subset of systems. In addition to the precision provided by *HST*, this combination yields individual (component) masses and, in many cases, independent constraints on parallaxes. Hence, although our sample is larger and contains most of the targets in Benedict et al. (2016), their analysis has the advantage of using individual, instead of total, masses.

We compare our $M_{K_S} - M_*$ relation with that of Benedict et al. (2016) in Figure 23. The two relations are in excellent agreement for $0.09\,M_\odot \lesssim M_* \lesssim 0.25\,M_\odot$. Below this regime, the Benedict et al. (2016) fit is effectively anchored by one star, GJ 1245C, because the two other stars in this low-mass regime (GJ 2005B and C) have relatively large errors. GJ 1245AC is in our sample, but we used a parallax from Lindegren et al. (2018) on GJ 1245B for this system, which places it 10σ (2.5%) more distant than the parallax adopted by Benedict et al. (2016). Our orbital parameters for this system are in excellent agreement with Benedict et al. (2016) if we adopt their distance, but the Lindegren et al. (2018) parallax makes the final parameters more consistent with our $M_{K_S} - M_*$ relation (although still 2σ discrepant). If the Benedict et al. (2016) parallax is correct, this reduces the total mass to $0.189 \pm 0.001\,M_\odot$, while the predicted mass is $0.207\,M_\odot$ for the adjusted M_K values (8.90 and 10.02 for the primary and companion, respectively). To reconcile the dynamical and predicted mass using the Benedict et al. (2016) parallax, we would need to explain why GJ 1245AC is $\simeq 0.3$ mag more luminous than predicted by other similar-mass objects. Some of the complications for GJ 1245 could be due to youth and/or activity, since the system is known to have a high flare rate (Lurie et al. 2015).
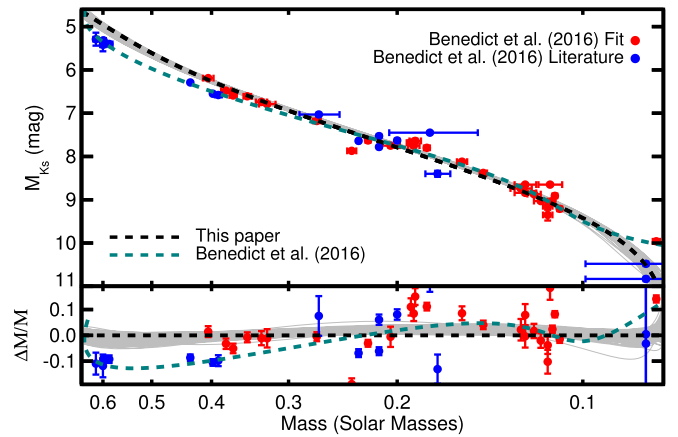
Figure 23. Absolute K_S-band magnitude as a function of M_* for astrometric binaries analyzed by Benedict et al. (2016; red circles) and those used in the Benedict et al. (2016) relation but pulled from the literature (blue circles). The resulting $M_* - M_{K_S}$ relation from Benedict et al. (2016) is shown as a teal dashed line, while the best-fit relation from this paper is shown as a black dashed line (with random samplings in gray as in earlier figures). The bottom panel shows the residual of the Benedict et al. (2016) points compared to our relation, with the Benedict et al. (2016) relation in teal for reference. Errors in the residuals only reflect errors in M_* and M_{K_S} and do not account for errors in our $M_* - M_{K_S}$ relation.

Above $0.3\,M_\odot$, Benedict et al. (2016) predict masses as much as 10% higher than our own for a fixed M_{K_S}. Our fit agrees reasonably well with the astrometric binaries analyzed by Benedict et al. (2016) in this mass regime. The divergence is driven instead by literature mass determinations that Benedict et al. (2016) included in their $M_{K_S} - M_*$ fit. Inspection of these literature points makes the origin of the discrepancy more clear: many are eclipsing binaries and have ΔK-band magnitudes of mixed quality and/or lack parallaxes needed for a precise M_{K_S}. GU Boo, for example, has absolute magnitudes estimated from an optical eclipse depth combined with bolometric corrections (López-Morales & Ribas 2005), which are drawn from models that perform poorly on M dwarfs (Lejeune et al. 1998; Hauschildt et al. 1999a). Similarly, for GJ 2069AC (CU Cnc) Benedict et al. (2016) adopted M_{K_S} from Ribas (2003) that disagrees with the 2MASS K_S and *Gaia* DR2 parallax (for either AC or B) using any ΔK_S.

In addition to GJ 1245AC, there are two targets in the Benedict et al. (2016) astrometric sample that are significantly discrepant from our own relation. These are GJ 1005AB and Gl 791.2AB, both of which have masses discrepant from predictions of the Benedict et al. (2016) relation. Our assigned total masses for both systems were much more consistent with both our $M_{K_S} - M_*$ relation and relation from Benedict et al. (2016). A comparison of our orbital fits with those of Benedict et al. (2016) revealed the source of the discrepancy; as we show in Figure 24 for GJ 1005AB, while the Benedict et al. (2016) orbit reproduces the astrometry from *HST*, it is highly discrepant from more recent astrometry (which was not included in the Benedict et al. 2016 fits). Comparing the Benedict et al. (2016) orbit to all astrometry used in our analysis yielded a χ^2 of 1978 (69 degrees of freedom). Our fit showed more tension with the *HST* astrometry but accurately reproduced all measurements within uncertainties, yielding a final χ^2 of 87 ($\chi^2_\nu = 1.3$). A similar effect can be seen in Gl 791.2AB. Because the discrepancy between our orbits and those in Benedict et al. (2016) for these two systems can be
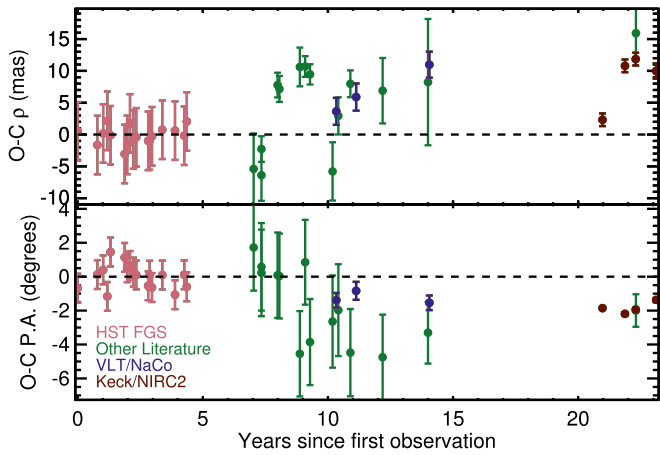
Figure 24. Difference between astrometry used in our fit and the orbital parameters from Benedict et al. (2016). The top panel shows the residuals in separation, while the bottom panel shows the residuals in position angle. Points are color-coded according to their source, including *HST* FGS data used in the Benedict et al. (2016) analysis.

seen in multiple sources of astrometry (including literature measurements), we consider our orbits and masses to be more accurate.

8. Conclusions and Discussion

8.1. Summary

The mass–luminosity relation has proven to be a critical tool for estimating masses of cool stars for decades and has broad applications ranging from characterizing extrasolar planets to measuring the initial mass function in massive galaxies. We endeavored to improve on existing M_{K_S}–M_* relations and evaluate the role of [Fe/H] on the relation by expanding the sample of calibrators, using new techniques to measure the metallicity of binary M dwarfs, and exploring the role of astrophysical scatter on the final precision.

As part of this effort, we combined AO data from Keck, CFHT, Gemini, and VLT with astrometric measurements from the literature to map the orbits of 55 binaries, which we join with seven systems with orbits from Dupuy & Liu (2017). While the more recent astrometry from Keck/NIRC2 was the most precise, the literature data provided >30 yr of data, which was essential to fit systems with >10 yr orbital periods. We include all our astrometry, as well as those from the literature, here, so that future work in this area can continue to grow this baseline and further improve the orbits of these systems.

Using parallaxes from the literature or derived from MEarth astrometry, we converted the orbital information into dynamical mass ($M_{tot,dyn}$) measurements for each binary. Six binaries in our final sample of 62 systems had total mass determinations better than 1%, 13 to better than 2%, and 28 to better than 5%.

We used our dynamical masses and resolved M_{K_S} magnitudes to fit for an empirical relation between M_* and M_{K_S}. Our methodology uses the observed quantity, which is the *total* mass of a given binary. This was done by making individual mass predictions from our resolved M_{K_S} estimates and the M_{K_S}–M_* relation and summing component masses to turn them into predictions for the total mass ($M_{tot,pre}$) of each binary. The $M_{tot,pre}$ values could then be compared directly to $M_{tot,dyn}$ estimates within the likelihood function. While this halves the

number of points constraining the fit compared to using individual masses, using M_{tot} is far more robust than using model-based mass ratios, reduces the need for observationally expensive radial velocity and/or absolute astrometry (difficult without *HST* for many systems), and helps increase the range of binaries amenable to characterization (e.g., wider systems with small radial velocity amplitudes).

The resulting M_{K_S}–M_* relation covers almost an order of magnitude in M_*, from $\simeq 0.70\,M_\odot$ down to the hydrogen-burning limit ($\simeq 0.075\,M_\odot$), and includes stars spanning the range of [Fe/H] expected for the solar neighborhood ($-0.6 <$ [Fe/H] $< +0.4$). Accounting for both intrinsic scatter and errors in the fit coefficients, masses from our M_{K_S}–M_* relation are precise to $\simeq 2\%$ over most of the M dwarf sequence, rising to $\simeq 3\%$ near the edges.

The primary limit to our precision is scatter in $M_{tot,dyn}$–$M_{tot,pre}$ above what is expected given measurement uncertainties alone. We characterized this missing error with a free parameter (σ_e), which we found to be $\simeq 2\%$ for all fits. It is likely that σ_e arose from intrinsic variation in the M_{K_S}–M_* relation due to a missing astrophysical parameter, such as age/activity/rotation (e.g., Kraus et al. 2011; Feiden 2016; Somers & Stassun 2017) or detailed abundances (e.g., Lindgren & Heiter 2017; Veyette et al. 2017), although we cannot rule out underestimated errors in the input orbital parameters, parallaxes, or K_S magnitudes.

We ran a series of tests to confirm that our use of M_{tot} and our assumed functional form did not bias our results or estimated uncertainties. To this end, we generated a set of synthetic binaries with component masses assigned using an assumed M_{K_S}–M_* relation. We ran our MCMC framework on these synthetic binaries, providing no information about the individual masses (only M_{tot}). The resulting fits matched the input M_{K_S}–M_* relation to within uncertainties. Our recovery of the input M_{K_S}–M_* relation worked even when we assumed a functional form different from our input relation (i.e., a piecewise function with sharp breaks).

As an additional test of our M_{K_S}–M_* relation, we compared predicted masses from the M_{K_S}–M_* relation to stars with *individual* dynamical masses from the literature. Our M_{K_S}–M_* provides individual mass estimates in excellent agreement with those from the literature, with a χ_ν^2 of 1.06 and an rms consistent with measurement uncertainties. There is a small ($\lesssim 2\%$) systematic offset between the literature eclipsing binaries and predictions from our own relation. With the exception of very young stars, tight eclipsing binaries will generally be more magnetically active and have faster rotation periods than their single-star counterparts. The fact that our M_{K_S}–M_* relation encompasses these stars within our quoted uncertainties suggests that the relation is effective for the majority of stars, which will have much lower activity levels.

Using empirically calibrated spectroscopic abundances, we explored the role of [Fe/H] on the M_{K_S}–M_* relation. Our results indicate that the effect of metallicity on the M_{K_S}–M_* relation is consistent with zero. MIST models significantly overestimate the importance of [Fe/H] in the M_{K_S}–M_* relation (at 5σ); however, predictions from updated DSEP models are consistent with our own.

We compared our relation to recent similar relations in the literature. Given quoted uncertainties, the Henry & McCarthy (1993), Delfosse et al. (2000), and Mann et al. (2015) relations

agreed with our own over the full sequence. Our results were consistent with the sample of astrometric binaries analyzed in Benedict et al. (2016), but our relation diverges from Benedict et al. (2016) above $\simeq 0.35\,M_\odot$. We attribute this difference to literature points included in the Benedict et al. (2016) fit from earlier analyses with uncertain distances and ΔK_S magnitudes. Our M_{K_S}–M_* relation represents a significant improvement in precision over all these earlier determinations.

8.2. Suggestions When Using Our M_{K_S}–M_* Relation

To help users interested in using M_{K_S} to compute realistic M_* and σ_{M_*} of single stars with parallaxes and K_S magnitudes, we provide a simple code (see footnote 14) to sample the fit posterior. Before using that code or the provided MCMC posteriors, take note of the following suggestions:

1. Our estimate of σ_e is only valid for stars comparable to the calibration sample. Targets that are unusual (in terms of activity, metallicity, etc.) compared to those in the solar neighborhood may have their mass uncertainties underestimated.

2. The fit behaves more poorly near the edges of the calibration sample. The scatter in the MCMC posterior accounts for this but restricts use to $4.0 < M_{K_S} < 11.0$ ($0.075\,M_\odot < M_* < 0.75\,M_\odot$), and a safer range would be $4.5 < M_{K_S} < 10.5$ ($0.08\,M_\odot < M_* < 0.70\,M_\odot$).

3. Our relation is only valid for main-sequence stars, and the roles of youth and activity were not accounted for in our analysis. Based on the Lyon models (Baraffe et al. 2015), we advise restricting use to >100 Myr above $0.4\,M_\odot$, >300 Myr to $0.2\,M_\odot$, >500 Myr to $0.1\,M_\odot$, and >1 Gyr below $0.1\,M_\odot$. A safer cut would be to only use this on stars >1 Gyr, similar to the calibration sample. The comparison to masses from eclipsing binaries suggests possible issues for highly active stars at the $\simeq 2\%$ level. While these are within our uncertainties, we suggest avoiding highly active stars until this can be directly tested with a more active sample of binaries.

4. The sample metallicity spans $-0.60 < $ [Fe/H] $< +0.45$, but 84% of the binaries have $-0.40 < $ [Fe/H] $< +0.30$. We provide a fit that attempts to take into account changes due to [Fe/H], and the weak impact suggests that the [Fe/H]-free relation is safe to use for most stars in the solar neighborhood. However, given the paucity of extreme metallicity systems in our calibration sample, we advise caution when targeting more metal-poor populations ([Fe/H] $\ll -0.6$).

5. The relation is only tested above the hydrogen-burning limit. Since the boundary likely depends on metallicity (Burrows et al. 2001), it is also not possible to use a simple M_{K_S} cut. Objects just below the hydrogen-burning limit age slowly (Baraffe et al. 2015), so the relation given here may give reasonable results, but we urge caution when interpreting resulting M_* values for $M_{K_S} > 10.5$.

6. Since σ_e is likely due to astrophysical variation in the relation, we suggest always including this as an irreducible and potentially systematic source of error.

8.3. Future Directions

We intentionally selected targets that had ΔK measurements, as M_{K_S} was known to give the tightest relation with M_* for M dwarfs. Unfortunately, only about one-third of the sample has measurements in an optical band. This limits the utility of the sample, as *Gaia G*, *BP*, and *RP* are now widely available for early and mid-M dwarfs and are generally measured with better precision than 2MASS K_S. The growing capabilities of speckle cameras (e.g., Horch et al. 2009) offer the opportunity to add optical contrasts. These can be converted to *Gaia* bandpasses, given reasonable assumptions about the component spectra, and used to derive an M_G–M_* (or M_G–M_*–[Fe/H]) relation that can be applied to millions of K and M dwarfs. Complementary optical data also provide colors for individual components, from which we can measure component $T_{\rm eff}$ and luminosity (e.g., Kraus et al. 2017).

We would like to explore changes in the impact of [Fe/H] as a function of M_{K_S} or M_*, especially given predictions from the DSEP models (Figure 16(b)). Metallicity effects may also become important only at extremely low metallicities, as was seen for the M_{K_S}–R_* relation (Kesseli et al. 2018a). Our sample was heavily biased toward the narrow [Fe/H] distribution of nearby stars. This limited our ability to both explore more complex impacts of [Fe/H] and tighten constraints on f. We identified four additional [Fe/H] < -0.5 binaries not included in our analysis, including two subdwarf systems. However, these systems have short baselines of astrometry in the literature when compared to their expected orbital periods, and complete orbits will take several more years. The availability of *Gaia* parallaxes will also help improve the precision of the known metal-poor systems and aid in the identification of new ones. Lastly, as new methods arrive to measure detailed abundances of M dwarfs (Veyette et al. 2016, 2017), we can explore effects beyond just [Fe/H].

Mass ratios were available for some systems (e.g., Söderhjelm 1999; Malogolovets et al. 2007; Dupuy & Liu 2017). However, these determinations were heterogeneous (e.g., some use models, some radial velocities, and some absolute astrometry), and some mass ratios reported in the literature are derived from orbits that disagree with our own determinations (e.g., Köhler et al. 2012). A more robust method would be to include radial velocity or absolute astrometry as part of our analysis. Fortunately, later *Gaia* data releases will include full absolute astrometry. When combined with a measure of the flux ratio in the *Gaia G* bandpass and our existing astrometry, we will be able to fit for both individual masses and parallaxes simultaneously. The resulting data set will effectively double our sample size and may help reveal the origin of σ_e.

The ages of our binary sample are not known, preventing any study of the effects of age on the M_{K_S}–M_* relation. However, our larger sample of binaries with orbit measurements still in progress contains known members of binaries in nearby young moving groups, known pre-main-sequence stars, and members of the Hyades. These systems span ages from 10 to 650 Myr, offering the chance to both test pre-main-sequence models of M dwarfs (Montet et al. 2015; Czekala et al. 2016; Nielsen et al. 2016; Rizzuto et al. 2016) and explore the role of activity on M dwarf parameters (e.g., Spada et al. 2013; Kesseli et al. 2018b). The current sample can be included in such work when combined with age indicators like kinematics (Wojno et al. 2018), ultraviolet flux

Appendix A
Converting Observed ΔK_X to 2MASS ΔK_S for M Dwarfs

To place all K-band magnitudes on the 2MASS system, we derived a relation between ΔK_X and ΔK_S as a function of ΔK_X, where X denotes the particular filter (K_s, K, K', Brγ, and $K_{\rm cont}$) used for the AO observations. For photometry, we only used observations taken with a filter somewhere in the K band (all wavelengths are used for astrometry).

To derive a conversion between contrasts, we used the 183 absolutely flux-calibrated spectra of nearby single stars from Mann et al. (2015), which cover a similar range of $T_{\rm eff}$ and M_* to the sample considered here. These spectra are mostly empirical; models are only used to fill in gaps in the spectrum or regions of high telluric contamination, none of which land in the regions covered by the filters considered here.

First, we randomly sampled two stars from the sample and scaled the absolute level of each spectrum by the star's distance. We convolved each of the two stars with the relevant filter profiles for NIRC2,[23] KIR,[24] NIRI,[25] or NaCo[26] and integrate over all wavelengths to compute the total flux in a given band. The ΔK_X value for the given pair was then computed as $2.5 \log_{10}(F_1/F_2)$. We computed the equivalent ΔK_S for each pair of stars using the 2MASS filter profile from Cohen et al. (2003).

We repeated this process with 5000 unique combinations of the 183 stars for 12 different filter/instrument combinations. For each filter and instrument combination we computed a best-fit line to $\Delta K_S - \Delta K_X$ as a function of ΔK_X. We show four examples in Figure 25. For the majority of the filters considered, the trend is insignificant compared to errors in the underlying spectra and absolute calibration (1%–2%). We did not apply a correction in these cases.

Most of the scatter seen in Figure 25 is due to random errors in the distance of the template star or Poisson noise in the spectra. $K_{\rm cont}$, for example, shows a larger apparent scatter in Figure 25, primarily because the narrow band is more sensitive to random Poisson errors in the calibrated spectra, but the final calibration is relatively precise. The uncertainties on applied

---

[23] https://www2.keck.hawaii.edu/inst/nirc2/filters.html
[24] http://www.cfht.hawaii.edu/Instruments/Filters/kir.html
[25] http://www.gemini.edu/sciops/instruments/niri/imaging/filters
[26] http://www.eso.org/sci/facilities/paranal/instruments/naco/inst/filters.html
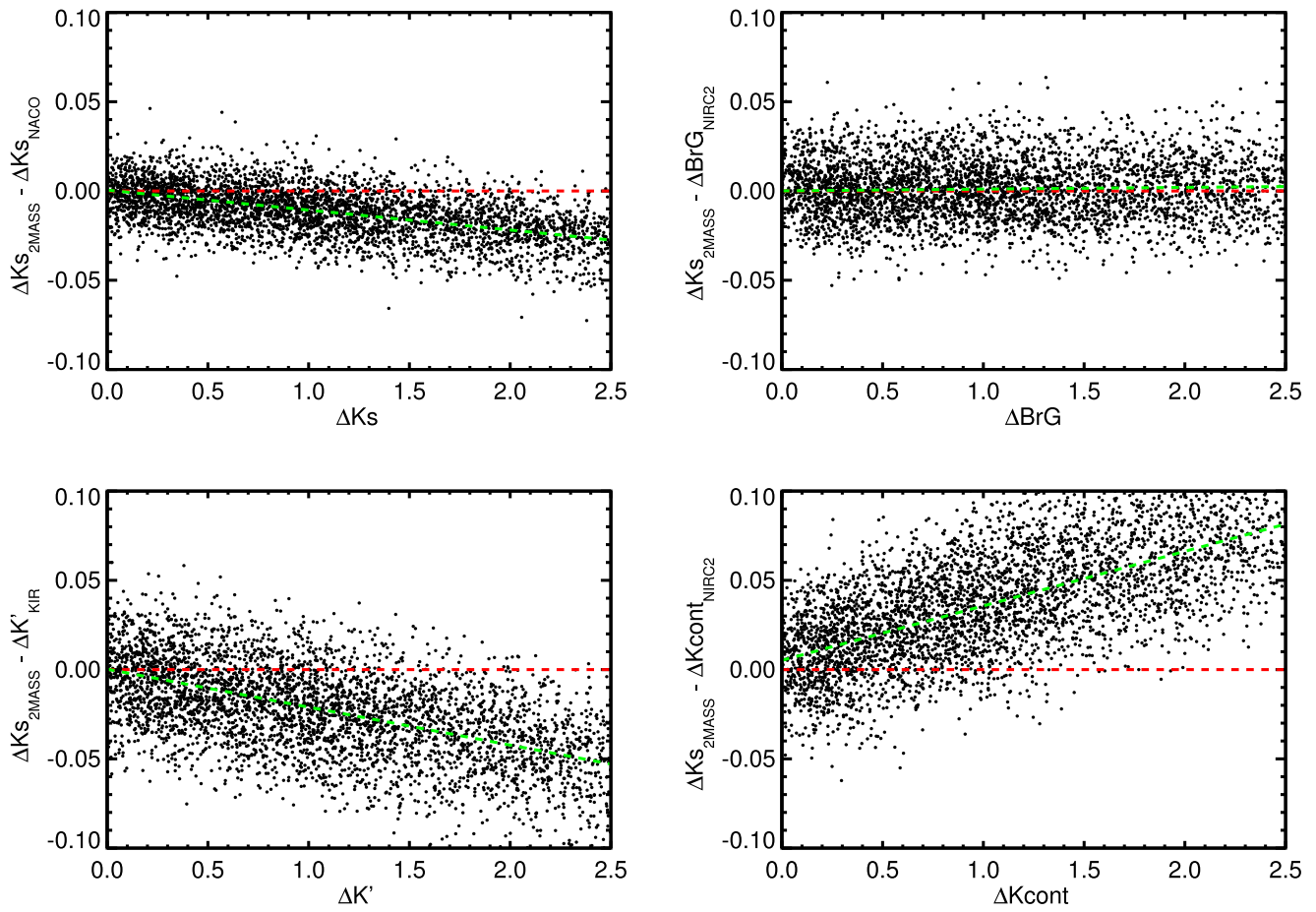
Figure 25. Difference between 2MASS ΔK_S and four example Δm values measured from our AO imaging, built from a grid of absolutely calibrated spectra and the relevant filter profile. No corrections are applied for the NIRC2 Brγ and K_S (K-short) filter, as the trend is not significant compared to the calibration precision of the underlying spectra.

corrections were 0.01–0.02 mag for all filters, which was driven primarily by potential systematic errors in the underlying spectra.

We did not see a significant difference in any derived correction based on the metallicity of the component stars. This was expected given how [Fe/H] changes K-band flux levels (Figure 6). We also found no significant effect as a function of the mass of the primary.

Appendix B
Orbits of Binaries

In Figure 26 we show diagnostic plots of each of the binaries in our sample. Here we show diagnostic plots of each of the binaries in our sample. Details of the input data can be found in Section 3.2 for data analyzed in this paper and in Section 4.1 for astrometry from the literature. The method by which we fit the orbits is described in Section 5.
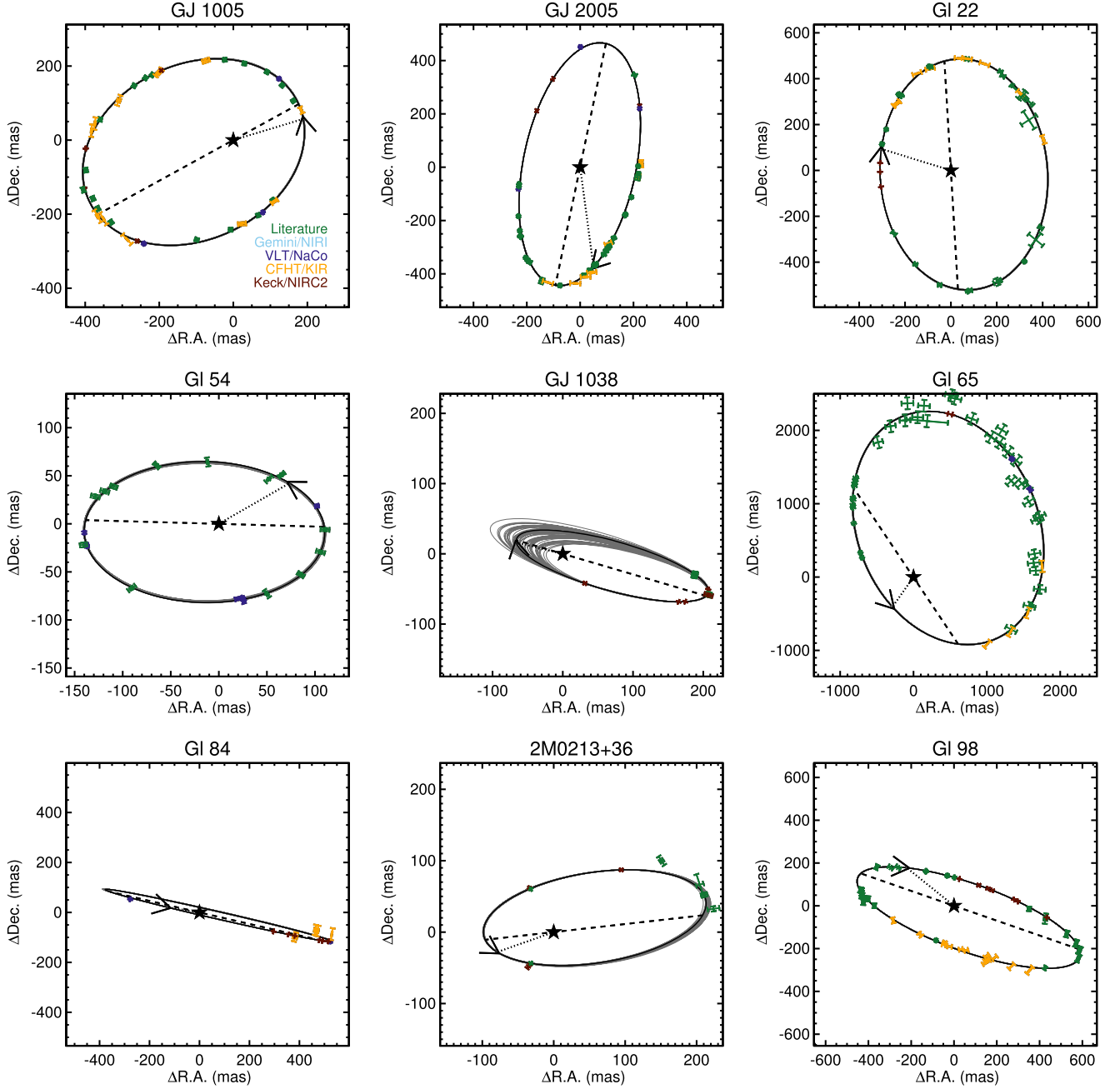
Figure 26. Orbital fit for each binary fit in this paper. The black star marks the primary (always at 0, 0). The best fit (highest likelihood) is shown as a black line, with 50 randomly selected orbit fits from the MCMC shown in gray to provide an estimate of the uncertainties. In some fits, the range of orbital solutions is so small that the gray lines are not visible underneath the best-fit black line. Points are individual separation and position angle measurements with adopted uncertainties, color-coded by the data source (Gemini/NIRI in light blue, VLT/NaCo in blue, CFHT/KIR in yellow, Keck/NIRC2 in dark red, and literature data in green). The dashed line is the line of nodes, the dotted line indicates periastron passage, and the arrow marks the direction of motion.
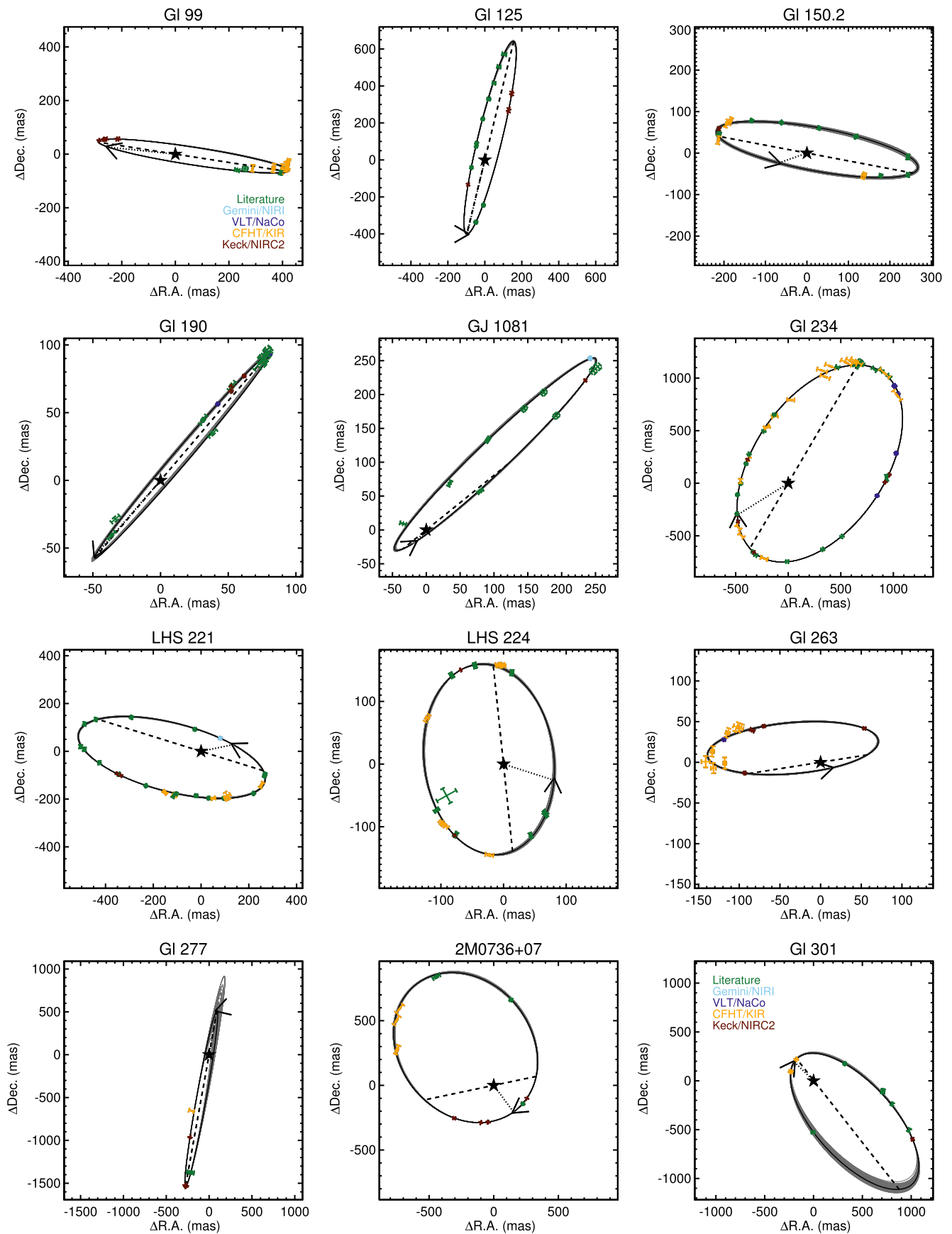
Figure 26. (Continued.)
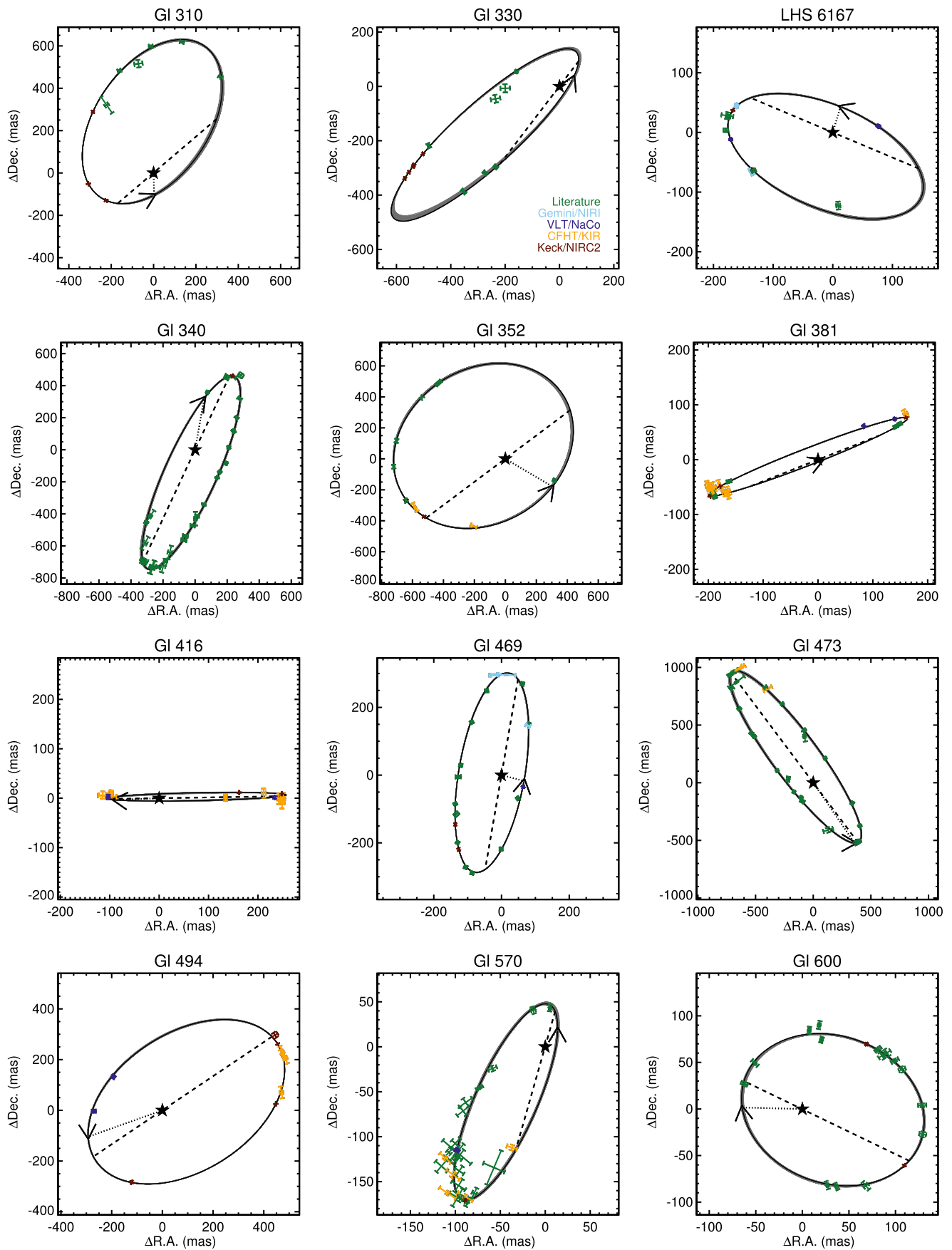
Figure 26. (Continued.)
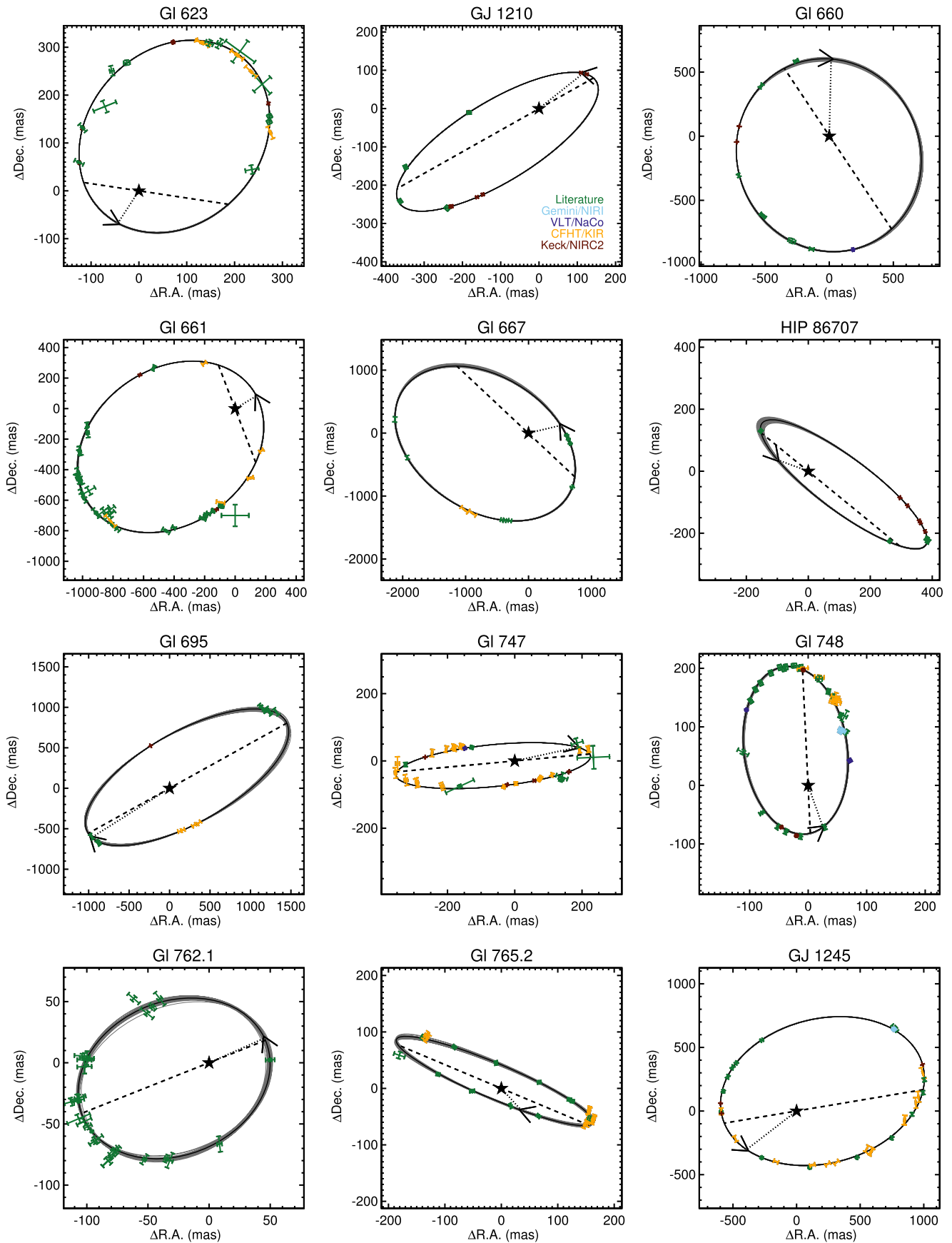
Figure 26. (Continued.)
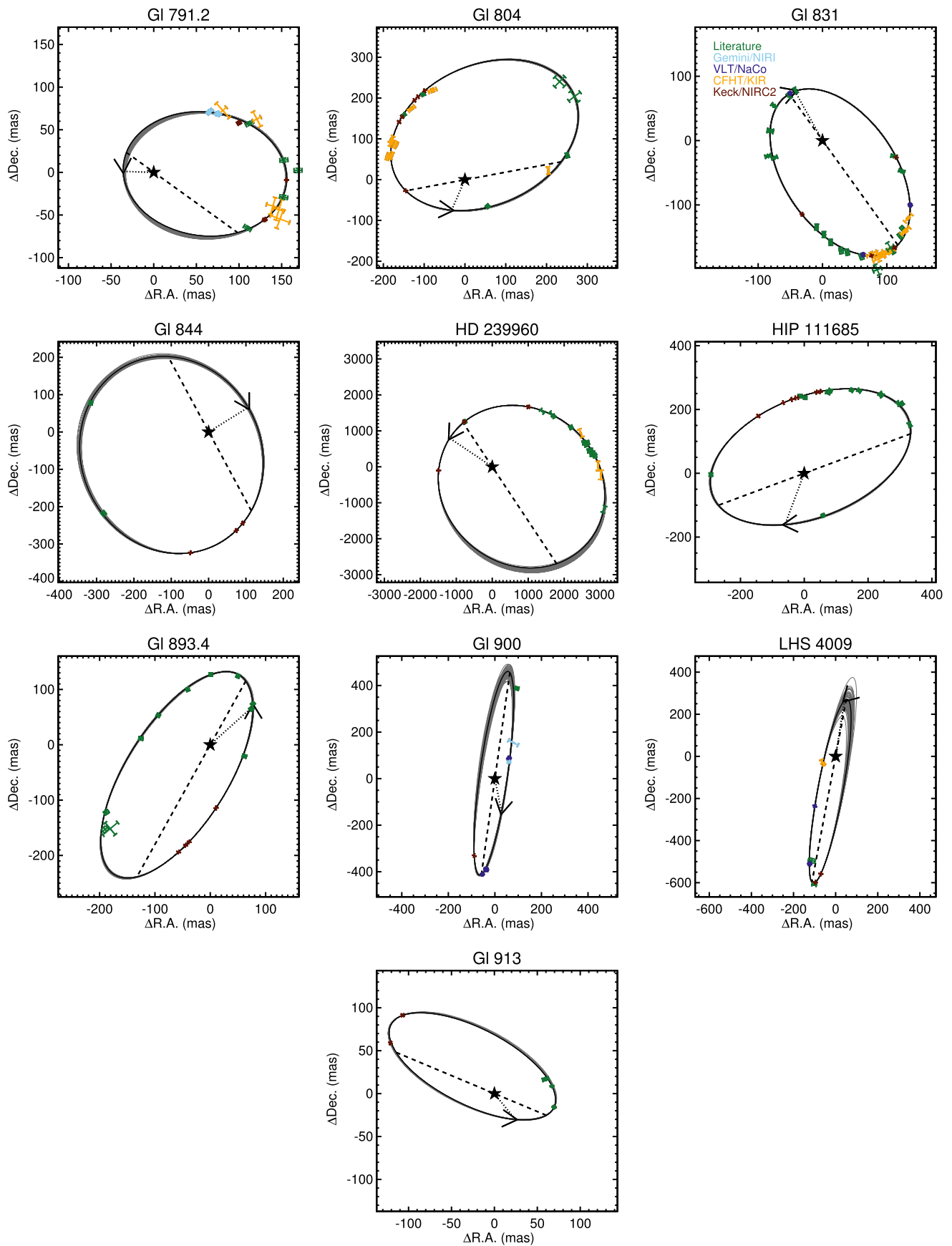
Figure 26. (Continued.)

ORCID iDs

Andrew W. Mann ⓘ https://orcid.org/0000-0003-3654-1602
Trent Dupuy ⓘ https://orcid.org/0000-0001-9823-1445
Adam L. Kraus ⓘ https://orcid.org/0000-0001-9811-568X
Eric Gaidos ⓘ https://orcid.org/0000-0002-5258-6846
Megan Ansdell ⓘ https://orcid.org/0000-0003-4142-9842
Michael Ireland ⓘ https://orcid.org/0000-0002-6194-043X
Aaron C. Rizzuto ⓘ https://orcid.org/0000-0001-9982-1332
Chao-Ling Hung ⓘ https://orcid.org/0000-0001-8025-8850
Jason Dittmann ⓘ https://orcid.org/0000-0001-7730-2240
Samuel Factor ⓘ https://orcid.org/0000-0002-8332-8516
Gregory Feiden ⓘ https://orcid.org/0000-0002-2012-7215
Raquel A. Martinez ⓘ https://orcid.org/0000-0001-6301-896X
Dary Ruíz-Rodríguez ⓘ https://orcid.org/0000-0003-3573-8163
Pa Chia Thao ⓘ https://orcid.org/0000-0001-5729-6576

References

Allard, F., Homeier, D., & Freytag, B. 2012, RSPTA, 370, 2765
Al-Shukri, A. M., McAlister, H. A., Hartkopf, W. I., Hutter, D. J., & Franz, O. G. 1996, AJ, 111, 393
Andersen, J. 1991, A&ARv, 3, 91
Ansdell, M., Gaidos, E., Mann, A. W., et al. 2015, ApJ, 798, 41
Arsenault, R., Salmon, D. A., Kerr, J. M., et al. 1994, Proc. SPIE, 2201, 833
Astropy Collaboration, Robitaille, T. P., Tollerud, E. J., et al. 2013, A&A, 558, A33
Aumer, M., & Binney, J. J. 2009, MNRAS, 397, 1286
Balega, I., Balega, Y. Y., Maksimov, A. F., et al. 2004, A&A, 422, 627
Balega, I. I., Balega, A. F., Maksimov, E. V., et al. 2006, BSAO, 59, 20
Balega, I. I., Balega, Y. Y., Belkin, I. N., et al. 1994, A&AS, 105, 503
Balega, I. I., Balega, Y. Y., Falcke, H., et al. 1997, AstL, 23, 172
Balega, I. I., Balega, Y. Y., Gasanova, L. T., et al. 2013, AstBu, 68, 53
Balega, I. I., Balega, Y. Y., Hofmann, K. H., et al. 2002a, A&A, 385, 87
Balega, I. I., Balega, Y. Y., Hofmann, K. H., et al. 2005, A&A, 433, 591
Balega, I. I., Balega, Y. Y., Hofmann, K. H., & Weigelt, G. 2001, AstL, 27, 95
Balega, I. I., Balega, Y. Y., Maksimov, A. F., et al. 1999, A&AS, 140, 287
Balega, I. I., Balega, Y. Y., Maksimov, A. F., et al. 2007a, AstBu, 62, 339
Balega, I. I., Balega, Y. Y., Vasyuk, V. V., & Tokovinin, A. A. 1991, PAZh, 17, 530
Balega, Y. Y., Beuzit, J. L., Delfosse, X., et al. 2007b, A&A, 464, 635
Balega, Y. Y., Tokovinin, A. A., Pluzhnik, E. A., & Weigelt, G. 2002b, AstL, 28, 773
Baraffe, I., Homeier, D., Allard, F., & Chabrier, G. 2015, A&A, 577, A42
Bartlett, J. L., Lurie, J. C., Riedel, A., et al. 2017, AJ, 154, 151
Bayless, A. J., & Orosz, J. A. 2006, ApJ, 651, 1155
Beck, T. L., Schaefer, G. H., Simon, M., et al. 2004, ApJ, 614, 235
Bell, C. P. M., Mamajek, E. E., & Naylor, T. 2015, MNRAS, 454, 593
Benedict, G. F., Henry, T. J., Franz, O. G., et al. 2016, AJ, 152, 141
Blazit, A., Bonneau, D., & Foy, R. 1987, A&AS, 71, 57
Bochanski, J. J., Munn, J. A., Hawley, S. L., et al. 2007, AJ, 134, 2418
Bonfils, X., Delfosse, X., Udry, S., et al. 2005, A&A, 442, 635
Bonneau, D., Balega, Y., Blazit, A., et al. 1986, A&AS, 65, 27
Boyajian, T., von Braun, K., Feiden, G. A., et al. 2015, MNRAS, 447, 846
Boyajian, T. S., von Braun, K., van Belle, G., et al. 2012, ApJ, 757, 112
Brewer, J. M., Fischer, D. A., Basu, S., Valenti, J. A., & Piskunov, N. 2015, ApJ, 805, 126
Brewer, J. M., Fischer, D. A., Valenti, J. A., & Piskunov, N. 2016, ApJS, 225, 32
Burrows, A., Hubbard, W. B., Lunine, J. I., & Liebert, J. 2001, RvMP, 73, 719
Casagrande, L., Schönrich, R., Asplund, M., et al. 2011, A&A, 530, A138
Casewell, S. L., Raynard, L., Watson, C. A., et al. 2018, arXiv:1808.02761
Castelli, F., & Kurucz, R. L. 2004, arXiv:astro-ph/0405087
Chen, Y., Girardi, L., Bressan, A., et al. 2014, MNRAS, 444, 2525
Choi, J., Dotter, A., Conroy, C., et al. 2016, ApJ, 823, 102
Chung, S., Zhu, W., Udalski, A., et al. 2017, ApJ, 838, 154
Cohen, M., Wheaton, W. A., & Megeath, S. T. 2003, AJ, 126, 1090
Conroy, C., & van Dokkum, P. 2012, ApJ, 747, 69
Covey, K. R., Hawley, S. L., Bochanski, J. J., et al. 2008, AJ, 136, 1778
Cushing, M. C., Vacca, W. D., & Rayner, J. T. 2004, PASP, 116, 362

Czekala, I., Andrews, S. M., Torres, G., et al. 2016, ApJ, 818, 156
Delfosse, X., Forveille, T., Ségransan, D., et al. 2000, A&A, 364, 217
Dieterich, S. B., Henry, T. J., Jao, W.-C., et al. 2014, AJ, 147, 94
Diolaiti, E., Bendinelli, O., Bonaccini, D., et al. 2000, A&AS, 147, 335
Dittmann, J. A., Irwin, J. M., Charbonneau, D., et al. 2017, Natur, 544, 333
Dittmann, J. A., Irwin, J. M., Charbonneau, D., & Berta-Thompson, Z. K. 2014, ApJ, 784, 156
Docobo, J. A., Tamazian, V. S., Balega, Y. Y., et al. 2008, A&A, 478, 187
Docobo, J. A., Tamazian, V. S., Balega, Y. Y., & Melikian, N. D. 2006, AJ, 132, 994
Docobo, J. A., Tamazian, V. S., Balega, Y. Y., & Melikian, N. D. 2010, AJ, 140, 1078
Dotter, A. 2016, ApJS, 222, 8
Dotter, A., Chaboyer, B., Jevremović, D., et al. 2008, ApJS, 178, 89
Douglass, G. G., Mason, B. D., Rafferty, T. J., Holdenried, E. R., & Germain, M. E. 2000, AJ, 119, 3071
Doyle, L. R., Carter, J. A., Fabrycky, D. C., et al. 2011, Sci, 333, 1602
Doyon, R., Nadeau, D., Vallee, P., et al. 1998, Proc. SPIE, 3354, 760
Dressing, C. D., & Charbonneau, D. 2013, ApJ, 767, 95
Dressing, C. D., Newton, E. R., Schlieder, J. E., et al. 2017, ApJ, 836, 167
Dupuy, T. J., Kratter, K. M., Kraus, A. L., et al. 2016, ApJ, 817, 80
Dupuy, T. J., & Liu, M. C. 2012, ApJS, 201, 19
Dupuy, T. J., & Liu, M. C. 2017, ApJS, 231, 15
Dupuy, T. J., Liu, M. C., & Bowler, B. P. 2009a, ApJ, 706, 328
Dupuy, T. J., Liu, M. C., Bowler, B. P., et al. 2010, ApJ, 721, 1725
Dupuy, T. J., Liu, M. C., & Ireland, M. J. 2009b, ApJ, 699, 168
Evans, D. F. 2018, RNAAS, 2, 20
Evans, T. M., Ireland, M. J., Kraus, A. L., et al. 2012, ApJ, 744, 120
Fabricius, C., & Makarov, V. V. 2000, A&AS, 144, 45
Feiden, G. A. 2016, A&A, 593, A99
Feiden, G. A., & Chaboyer, B. 2012, ApJ, 757, 42
Feiden, G. A., & Chaboyer, B. 2013, ApJ, 779, 183
Feiden, G. A., & Chaboyer, B. 2014a, ApJ, 789, 53
Feiden, G. A., & Chaboyer, B. 2014b, A&A, 571, A70
Ferguson, D., Gardner, S., & Yanny, B. 2017, ApJ, 843, 141
Finch, C. T., & Zacharias, N. 2016, AJ, 151, 160
Foreman-Mackey, D. 2016, JOSS, 24
Foreman-Mackey, D., Hogg, D. W., Lang, D., & Goodman, J. 2013, PASP, 125, 306
Fortney, J. J. 2012, ApJL, 747, L27
Forveille, T., Beuzit, J.-L., Delfosse, X., et al. 1999, A&A, 351, 619
Fu, H.-H., Hartkopf, W. I., Mason, B. D., et al. 1997, AJ, 114, 1623
Gagné, J., Lafrenière, D., Doyon, R., Malo, L., & Artigau, É 2014, ApJ, 783, 121
Gagné, J., Lafrenière, D., Doyon, R., Malo, L., & Artigau, É 2015, ApJ, 798, 73
Gaia Collaboration, Babusiaux, C., van Leeuwen, F., et al. 2018a, A&A, 616, A10
Gaia Collaboration, Brown, A. G. A., Vallenari, A., et al. 2016, A&A, 595, A2
Gaia Collaboration, Brown, A. G. A., Vallenari, A., et al. 2018b, A&A, 616, A1
Gaidos, E. 2013, ApJ, 770, 90
Gaidos, E. 2015, ApJ, 804, 40
Gaidos, E., & Mann, A. W. 2013, ApJ, 762, 41
Gaidos, E., & Mann, A. W. 2014, ApJ, 791, 54
Gaidos, E., Mann, A. W., Kraus, A. L., & Ireland, M. 2016, MNRAS, 457, 2877
Gaidos, E., Mann, A. W., Lépine, S., et al. 2014, MNRAS, 443, 2561
Germain, M. E., Douglass, G. G., & Worley, C. E. 1999, AJ, 117, 1905
Geyer, D. W., Harrington, R. S., & Worley, C. E. 1988, AJ, 95, 1841
Gillon, M., Triaud, A. H. M. J., Demory, B.-O., et al. 2017, Natur, 542, 456
Goldin, A., & Makarov, V. V. 2006, ApJS, 166, 341
Goodman, J., & Weare, J. 2010, Communications in Applied Mathematics and Computational Science, 5, 65
Han, E., Muirhead, P. S., Swift, J. J., et al. 2017, AJ, 154, 100
Hansen, C. J., Kawaler, S. D., & Trimble, V. 2004, Stellar Interiors: Physical Principles, Structure, and Evolution (Berlin: Springer)
Hartkopf, W. I., & Mason, B. D. 2009, AJ, 138, 813
Hartkopf, W. I., Mason, B. D., McAlister, H. A., et al. 2000, AJ, 119, 3084
Hartkopf, W. I., Mason, B. D., & Rafferty, T. J. 2008, AJ, 135, 1334
Hartkopf, W. I., McAlister, H. A., & Franz, O. G. 1992, AJ, 104, 810
Hartkopf, W. I., McAlister, H. A., Mason, B. D., et al. 1994, AJ, 108, 2299
Hartkopf, W. I., McAlister, H. A., Mason, B. D., et al. 1997, AJ, 114, 1639
Hartkopf, W. I., McAlister, H. A., & Mason, B. D. 2001, AJ, 122, 3480
Hartkopf, W. I., Tokovinin, A., & Mason, B. D. 2012, AJ, 143, 42
Hartman, J. D., Bakos, G. Á, Noyes, R. W., et al. 2011, AJ, 141, 166

Hartman, J. D., Quinn, S. N., Bakos, G. Á., et al. 2018, AJ, 155, 114
Hauschildt, P. H., Allard, F., & Baron, E. 1999a, ApJ, 512, 377
Hauschildt, P. H., Allard, F., Ferguson, J., Baron, E., & Alexander, D. R. 1999b, ApJ, 525, 871
Hejazi, N., De Robertis, M. M., & Dawson, P. C. 2015, AJ, 149, 140
Hełminiak, K. G., Konacki, M., Kulkarni, S. R., & Eisner, J. 2009, MNRAS, 400, 406
Henry, T. J., Kirkpatrick, J. D., & Simons, D. A. 1994, AJ, 108, 1437
Henry, T. J., & McCarthy, D. W., Jr. 1993, AJ, 106, 773
Hershey, J. L., & Taff, L. G. 1998, AJ, 116, 1440
Hinkel, N. R., Timmes, F. X., Young, P. A., Pagano, M. D., & Turnbull, M. C. 2014, AJ, 148, 54
Hinkel, N. R., Young, P. A., Pagano, M. D., et al. 2016, ApJS, 226, 4
Hodapp, K. W., Jensen, J. B., Irwin, E. M., et al. 2003, PASP, 115, 1388
Horch, E. P., Bahi, L. A. P., Gaulin, J. R., et al. 2012, AJ, 143, 10
Horch, E. P., Casetti-Dinescu, D. I., Camarata, M. A., et al. 2017, AJ, 153, 212
Horch, E. P., Davidson, J. W., Jr., van Altena, W. F., et al. 2006, AJ, 131, 1000
Horch, E. P., Falta, D., Anderson, L. M., et al. 2010, AJ, 139, 205
Horch, E. P., Gomez, S. C., Sherry, W. H., et al. 2011, AJ, 141, 45
Horch, E. P., Robinson, S. E., Meyer, R. D., et al. 2002, AJ, 123, 3442
Horch, E. P., van Altena, W. F., Demarque, P., et al. 2015a, AJ, 149, 151
Horch, E. P., van Altena, W. F., William, M. C., Jr., et al. 2008, AJ, 136, 312
Horch, E. P., van Belle, G. T., Davidson, J. W., Jr., et al. 2015b, AJ, 150, 151
Horch, E. P., Veillette, D. R., Baena Gallé, R., et al. 2009, AJ, 137, 5057
Irwin, J., Charbonneau, D., Berta, Z. K., et al. 2009, ApJ, 701, 1436
Irwin, J. M., Quinn, S. N., Berta, Z. K., et al. 2011, ApJ, 742, 123
Janson, M., Bergfors, C., Brandner, W., et al. 2014, ApJ, 789, 102
Janson, M., Hormuth, F., Bergfors, C., et al. 2012, ApJ, 754, 44
Jódar, E., Pérez-Garrido, A., Díaz-Sánchez, A., et al. 2013, MNRAS, 429, 859
Johnson, J. A., & Apps, K. 2009, ApJ, 699, 933
Jones, E., Oliphant, T., Peterson, P., et al. 2001, SciPy: Open Source Scientific Tools for Python, http://www.scipy.org/
Jurić, M., Ivezić, Ž, Brooks, A., et al. 2008, ApJ, 673, 864
Kane, S. R., von Braun, K., Henry, G. W., et al. 2017, ApJ, 835, 200
Kesseli, A. Y., Kirkpatrick, J. D., Fajardo-Acosta, S. B., et al. 2018a, arXiv:1810.07702
Kesseli, A. Y., Muirhead, P. S., Mann, A. W., & Mace, G. 2018b, AJ, 155, 225
Köhler, R., Ratzka, T., & Leinert, C. 2012, A&A, 541, 29
Kraus, A. L., Douglas, S. T., Mann, A. W., et al. 2017, ApJ, 845, 72
Kraus, A. L., Ireland, M. J., Huber, D., Mann, A. W., & Dupuy, T. J. 2016, AJ, 152, 8
Kraus, A. L., Ireland, M. J., Martinache, F., & Lloyd, J. P. 2008, ApJ, 679, 762
Kraus, A. L., Shkolnik, E. L., Allers, K. N., & Liu, M. C. 2014, AJ, 147, 146
Kraus, A. L., Tucker, R. A., Thompson, M. I., Craine, E. R., & Hillenbrand, L. A. 2011, ApJ, 728, 48
Law, N. M., Dhital, S., Kraus, A., Stassun, K. G., & West, A. A. 2010, ApJ, 720, 1727
Law, N. M., Hodgkin, S. T., & Mackay, C. D. 2008, MNRAS, 384, 150
Lee, J., & Song, I. 2018, MNRAS, 475, 2955
Lejeune, T., Cuisinier, F., & Buser, R. 1998, A&AS, 130, 65
Lépine, S., Hilton, E. J., Mann, A. W., et al. 2013, AJ, 145, 102
Lépine, S., Rich, R. M., & Shara, M. M. 2007, ApJ, 669, 1235
Lindegren, L., Hernández, J., Bombrun, A., et al. 2018, A&A, 616, A2
Lindgren, S., & Heiter, U. 2017, A&A, 604, A97
Liu, M. C., Dupuy, T. J., & Ireland, M. J. 2008, ApJ, 689, 436
Lloyd, J. P., Martinache, F., Ireland, M. J., et al. 2006, ApJL, 650, L131
Lopez-Morales, M., Orosz, J. A., Shaw, J. S., et al. 2006, arXiv:astro-ph/0610225
López-Morales, M., & Ribas, I. 2005, ApJ, 631, 1120
Lu, J. R., Ghez, A. M., Hornstein, S. D., et al. 2009, ApJ, 690, 1463
Lu, J. R., Ghez, A. M., Yelda, S., et al. 2010, Proc. SPIE, 7736, 77361I
Lurie, J. C., Davenport, J. R. A., Hawley, S. L., et al. 2015, ApJ, 800, 95
MacDonald, J., & Mullan, D. J. 2012, MNRAS, 421, 3084
Mace, G. N., Mann, A. W., Skiff, B. A., et al. 2018, ApJ, 854, 145
Malo, L., Artigau, É., Doyon, R., et al. 2014, ApJ, 788, 81
Malogolovets, E. V., Balega, Y. Y., Rastegaev, D. A., Hofmann, K. H., & Weigelt, G. 2007, AstBu, 62, 117
Mann, A. W., Brewer, J. M., Gaidos, E., Lépine, S., & Hilton, E. J. 2013a, AJ, 145, 52
Mann, A. W., Deacon, N. R., Gaidos, E., et al. 2014, AJ, 147, 160
Mann, A. W., Feiden, G. A., Gaidos, E., Boyajian, T., & von Braun, K. 2015, ApJ, 804, 64
Mann, A. W., Gaidos, E., & Ansdell, M. 2013b, ApJ, 779, 188
Mann, A. W., Gaidos, E., Lépine, S., & Hilton, E. J. 2012, ApJ, 753, 90
Mann, A. W., Vanderburg, A., Rizzuto, A. C., et al. 2018, AJ, 155, 4
Mann, A. W., & von Braun, K. 2015, PASP, 127, 102

Markwardt, C. B. 2009, in ASP Conf. Ser. 411, Astronomical Data Analysis Software and Systems XVIII, ed. D. A. Bohlender, D. Durand, & P. Dowler (San Francisco, CA: ASP), 251
Martinache, F., Lloyd, J. P., Ireland, M. J., Yamada, R. S., & Tuthill, P. G. 2007, ApJ, 661, 496
Martinez, A. O., Crossfield, I. J. M., Schlieder, J. E., et al. 2017, ApJ, 837, 72
Masciadri, E., Brandner, W., Bouy, H., et al. 2003, A&A, 411, 157
Mason, B. D., Hartkopf, W. I., Gies, D. R., Henry, T. J., & Helsel, J. W. 2009, AJ, 137, 3358
Mason, B. D., Hartkopf, W. I., Holdenried, E. R., et al. 2000, AJ, 120, 1120
Mason, B. D., Hartkopf, W. I., Miles, K. N., et al. 2018, AJ, 155, 215
Mason, B. D., Hartkopf, W. I., Urban, S. E., et al. 2002, AJ, 124, 2254
Mason, B. D., Hartkopf, W. I., Wycoff, G. L., et al. 2004a, AJ, 127, 539
Mason, B. D., Hartkopf, W. I., Wycoff, G. L., et al. 2004b, AJ, 128, 3012
Mason, B. D., Hartkopf, W. I., & Wycoff, G. L. 2011, AJ, 141, 157
Mason, B. D., Hartkopf, W. I., Wycoff, G. L., & Holdenried, E. R. 2006, AJ, 132, 2219
Mason, B. D., Hartkopf, W. I., Wycoff, G. L., & Wieder, G. 2007, AJ, 134, 1671
McAlister, H. A., Hartkopf, W. I., & Franz, O. G. 1990, AJ, 99, 965
McAlister, H. A., Hartkopf, W. I., Gaston, B. J., Hendry, E. M., & Fekel, F. C. 1984, ApJS, 54, 251
McAlister, H. A., Hartkopf, W. I., Hutter, D. J., & Franz, O. G. 1987, AJ, 93, 688
McAlister, H. A., Hartkopf, W. I., Sowell, J. R., Dombrowski, E. G., & Franz, O. G. 1989, AJ, 97, 510
McAlister, H. A., Hendry, E. M., Hartkopf, W. I., Campbell, B. G., & Fekel, F. C. 1983, ApJS, 51, 309
McConnell, N. J., Lu, J. R., & Mann, A. W. 2016, ApJ, 821, 39
Montet, B. T., Bowler, B. P., Shkolnik, E. L., et al. 2015, ApJL, 813, L11
Muirhead, P. S., Becker, C., Feiden, G. A., et al. 2014, ApJS, 213, 5
Muirhead, P. S., Hamren, K., Schlawin, E., et al. 2012a, ApJL, 750, L37
Muirhead, P. S., Johnson, J. A., Apps, K., et al. 2012b, ApJ, 747, 144
Muirhead, P. S., Mann, A. W., Vanderburg, A., et al. 2015, ApJ, 801, 18
Mulders, G. D., Pascucci, I., & Apai, D. 2015, ApJ, 798, 112
Neuhäuser, R., Guenther, E. W., Wuchterl, G., et al. 2005, A&A, 435, L13
Neves, V., Bonfils, X., Santos, N. C., et al. 2012, A&A, 538, A25
Neves, V., Bonfils, X., Santos, N. C., et al. 2014, A&A, 568, A121
Newton, E. R., Charbonneau, D., Irwin, J., et al. 2014, AJ, 147, 20
Newton, E. R., Charbonneau, D., Irwin, J., & Mann, A. W. 2015, ApJ, 800, 85
Nielsen, E. L., De Rosa, R. J., Wang, J., et al. 2016, AJ, 152, 175
Nutzman, P., & Charbonneau, D. 2008, PASP, 120, 317
Park, C., Jaffe, D. T., Yuk, I.-S., et al. 2014, Proc. SPIE, 9147, 91471E
Parsons, S. G., Gänsicke, B. T., Marsh, T. R., et al. 2018, MNRAS, 481, 1083
Petigura, E. A., Howard, A. W., & Marcy, G. W. 2013, PNAS, 110, 19273
Plewa, P. M., Gillessen, S., Eisenhauer, F., et al. 2015, MNRAS, 453, 3234
Rajpurohit, A. S., Reylé, C., Allard, F., et al. 2013, A&A, 556, A15
Rayner, J., Bond, T., Bonnet, M., et al. 2012, Proc. SPIE, 8446, 84462C
Rayner, J. T., Toomey, D. W., Onaka, P. M., et al. 2003, PASP, 115, 362
Reggiani, M., Meyer, M. R., Chauvin, G., et al. 2016, A&A, 586, A147
Reid, I. N., Cruz, K. L., Allen, P., et al. 2004, AJ, 128, 463
Reid, I. N., Gizis, J. E., & Hawley, S. L. 2002, AJ, 124, 2721
Reiners, A., & Basri, G. 2009, ApJ, 705, 1416
Ribas, I. 2003, A&A, 398, 239
Ricker, G. R., Winn, J. N., Vanderspek, R., et al. 2014, Proc. SPIE, 9143, 20
Riedel, A. R., Blunt, S. C., Lambrides, E. L., et al. 2017, AJ, 153, 95
Riedel, A. R., Subasavage, J. P., Finch, C. T., et al. 2010, AJ, 140, 897
Rizzuto, A. C., Ireland, M. J., Dupuy, T. J., & Kraus, A. L. 2016, ApJ, 817, 164
Rizzuto, A. C., Mann, A. W., Vanderburg, A., Kraus, A. L., & Covey, K. R. 2017, AJ, 154, 224
Rodriguez, D. R., Duchêne, G., Tom, H., et al. 2015, MNRAS, 449, 3160
Rogers, L. A., Bodenheimer, P., Lissauer, J. J., & Seager, S. 2011, ApJ, 738, 59
Rojas-Ayala, B., Covey, K. R., Muirhead, P. S., & Lloyd, J. P. 2010, ApJL, 720, L113
Rojas-Ayala, B., Covey, K. R., Muirhead, P. S., & Lloyd, J. P. 2012, ApJ, 748, 93
Schlaufman, K. C., & Laughlin, G. 2010, A&A, 519, A105
Schlieder, J. E., Lépine, S., Rice, E., et al. 2012, AJ, 143, 114
Schroeder, D. J., Golimowski, D. A., Brukardt, R. A., et al. 2000, AJ, 119, 906
Ségransan, D., Delfosse, X., Forveille, T., et al. 2000, A&A, 364, 665
Seifahrt, A., Röll, T., Neuhäuser, R., et al. 2008, A&A, 484, 429
Service, M., Lu, J. R., Campbell, R., et al. 2016, PASP, 128, 095004
Shields, A. L., Ballard, S., & Johnson, J. A. 2016, PhR, 663, 1
Shin, I. G., Udalski, A., Yee, J. C., et al. 2017, AJ, 154, 176

Shkolnik, E. L., Allers, K. N., Kraus, A. L., Liu, M. C., & Flagg, L. 2017, AJ, 154, 69
Shkolnik, E. L., Anglada-Escudé, G., Liu, M. C., et al. 2012, ApJ, 758, 56
Skrutskie, M. F., Cutri, R. M., Stiening, R., et al. 2006, AJ, 131, 1163
Söderhjelm, S. 1999, A&A, 341, 121
Somers, G., & Stassun, K. G. 2017, AJ, 153, 101
Spada, F., Demarque, P., Kim, Y.-C., & Sills, A. 2013, ApJ, 776, 87
Spiniello, C., Barnabè, M., Koopmans, L. V. E., & Trager, S. C. 2015, MNRAS, 452, L21
Stapelfeldt, K. R., Ménard, F., Watson, A. M., et al. 2003, ApJ, 589, 410
Stevens, D. J., Gaudi, B. S., & Stassun, K. G. 2018, ApJ, 862, 53
Tarter, J. C., Backus, P. R., Mancinelli, R. L., et al. 2007, AsBio, 7, 30
Terrien, R. C., Mahadevan, S., Bender, C. F., et al. 2012, ApJL, 747, L38
Terrien, R. C., Mahadevan, S., Bender, C. F., Deshpande, R., & Robertson, P. 2015a, ApJL, 802, L10
Terrien, R. C., Mahadevan, S., Deshpande, R., & Bender, C. F. 2015b, ApJS, 220, 16
Teske, J. K., Ghezzi, L., Cunha, K., et al. 2015, ApJL, 801, L10
Tokovinin, A. 2017, AJ, 154, 110
Tokovinin, A. 2018, ApJS, 235, 6
Tokovinin, A., Mason, B. D., & Hartkopf, W. I. 2010, AJ, 139, 743
Tokovinin, A., Mason, B. D., & Hartkopf, W. I. 2014, AJ, 147, 123
Tokovinin, A., Mason, B. D., Hartkopf, W. I., Mendez, R. A., & Horch, E. P. 2015, AJ, 150, 50
Tokovinin, A., Mason, B. D., Hartkopf, W. I., Mendez, R. A., & Horch, E. P. 2016, AJ, 151, 153
Tokovinin, A., Mason, B. D., Hartkopf, W. I., Mendez, R. A., & Horch, E. P. 2018, AJ, 155, 235
Tokovinin, A. A., & Smekhov, M. G. 2002, A&A, 382, 118
Torres, G., Andersen, J., & Giménez, A. 2010, A&ARv, 18, 67
Torres, G., & Ribas, I. 2002, ApJ, 567, 1140
Vacca, W. D., Cushing, M. C., & Rayner, J. T. 2003, PASP, 115, 389
van Altena, W. F., Lee, J. T., & Hoffleit, E. D. 1995, The General Catalogue of Trigonometric [stellar] Parallaxes (New Haven, CT: Yale Univ. Observatory)
van Dam, M. A., Le Mignant, D., & Macintosh, B. A. 2004, ApOpt, 43, 5458
van Dokkum, P. G. 2001, PASP, 113, 1420
Van Grootel, V., Fernandes, C. S., Gillon, M., et al. 2018, ApJ, 853, 30
van Leeuwen, F. 2007, A&A, 474, 653
Veyette, M. J., Muirhead, P. S., Mann, A. W., et al. 2017, ApJ, 851, 26
Veyette, M. J., Muirhead, P. S., Mann, A. W., & Allard, F. 2016, ApJ, 828, 95
Ward-Duong, K., Patience, J., De Rosa, R. J., et al. 2015, MNRAS, 449, 2618
Wheeler, J. C. 2012, ApJ, 758, 123
Wilson, R. E., Pilachowski, C. A., & Terrell, D. 2017, ApJ, 835, 251
Winn, J. N. 2010, in Exoplanet Transits and Occultations, Space Science Series, ed. S. Seager (Tucson, AZ: Univ. Arizona Press), 55
Winters, J. G., Hambly, N. C., Jao, W.-C., et al. 2015, AJ, 149, 5
Wizinowich, P., Acton, D. S., Shelton, C., et al. 2000, PASP, 112, 315
Woitas, J., Tamazian, V. S., Docobo, J. A., & Leinert, C. 2003, A&A, 406, 293
Wojno, J., Kordopatis, G., Steinmetz, M., et al. 2018, MNRAS, 477, 5612
Woolf, V. M., & Wallerstein, G. 2006, PASP, 118, 218
Woolf, V. M., & West, A. A. 2012, MNRAS, 422, 1489
Yelda, S., Lu, J. R., Ghez, A. M., et al. 2010, ApJ, 725, 331
Yi, Z.-P., Luo, A.-L., Zhao, J.-K., et al. 2015, RAA, 15, 860
Yuk, I.-S., Jaffe, D. T., Barnes, S., et al. 2010, Proc. SPIE, 7735, 77351M
Zhou, G., Bayliss, D., Hartman, J. D., et al. 2015, MNRAS, 451, 2263
Zhu, W., Calchi Novati, S., Gould, A., et al. 2016, ApJ, 825, 60